Nano Today 11 (2016) 483–520

Contents lists available at ScienceDirect

Nano Today

journal homepage: www.elsevier.com/locate/nanotoday

Review

2D nanosheets-based novel architectures: Synthesis, assembly and applications

Jianhua Shen, Yihua Zhu*, Hao Jiang, Chunzhong Li*

Key Laboratory for Ultrafine Materials of Ministry of Education, School of Materials Science and Engineering, East China University of Science and Technology, 130 Meilong Road, Shanghai 200237, China

ARTICLE INFO

Article history:
Received 13 April 2016
Received in revised form 27 June 2016
Accepted 9 July 2016
Available online 5 August 2016

Keywords:
2D nanosheets
3D architectures
Energy storage
Electrocatalysis
Sensing

ABSTRACT

The discovery of graphene attracted great interest because of the potential prospects of which in both basic and applied research. And other kinds of 2D graphene analogues, including hexagonal BN, carbon nitride, transition metal dichalcogenides, etc. derived from their layered bulk crystals, have also been extensively investigated because of their promising characters and potential applications. It is expected that these 2D nanosheets, in bulk or in composite materials, could maintain their extraordinary properties. However, the irreversible aggregation or accumulating of 2D nanosheets due to the strong van der Waals interactions, extremely decrease their accessible surface area. More recently, with the recognization of the tremendous interest of these 2D structures, scientists noticed that the performance of certain devices could be significantly improved by utilizing 3D architectures and/or aerogels due to the increase of unit activity of the materials. This review summarizes different synthetic process (such as assembly, chemical vapor deposition direct synthesis, *in-situ* confinement growth and so on) used for preparation of 2D graphene analogues based 3D architectures and/or aerogels containing either any or their composites. And the different fields of application for energy storage (including both supercapacitor and lithium ion battery applications), electrocatalysis, sensing and others are provided a significant enhancement in the efficacy as compared to their 2D analogues or even opened the path to novel application. In addition, some perspectives on the challenges and opportunities in this promising research area are also discussed.

Contents

* Corresponding authors.
E-mail addresses: yhzhu@ecust.edu.cn (Y. Zhu), czli@ecust.edu.cn (C. Li).

http://dx.doi.org/10.1016/j.nantod.2016.07.005
1748-0132/

Introduction

Two-dimensional (2D) nanomaterial was predicted to be unstable in nature for ages until 2004, when graphene, a one-atom-thick faveolate structure consisted of carbon atoms, was successfully fabricated [1]. The discovery of graphene has attracted much interest due to its potential prospects in both basic and applied research [2,3]. Since many unconventional properties have been observed in graphene including integral quantum Hall effects (IQHE) [4–6], ultrahigh electron mobility [7], as well as many other novel phenomena and characters [8,9], because of its Dirac-cone structure, and the rapid development of graphene also throws new light on discovering more 2D materials [10,11].

Thus far, more than hundreds of 2D materials have been developed, such as metal chalcogenides, complex oxides, compounds of group-IV elements, binary group III–V systems and so on [11]. And in recent years, these 2D inorganic nanomaterials, particularly mono- and multi-layered nanosheets, have received increasing research [12]. These distinctive ultrathin thickness and 2D morphology perform some unaccustomed physical, chemical or electronic characters compared to their bulk congeries, and thus show inspirational potentials for a variety of applications such as catalysis, energy storage and photovoltaics [11,13,14].

It is expected that these 2D nanosheets, in bulk or in composite systems, could maintain their extraordinary properties. However, the irreversible aggregation or accumulating of 2D nanosheets due to the strong van der Waals interactions, extremely decrease their accessible surface area [15]. Many efforts have been devoted to solve this problem. One option is to manipulate the 2D nanomaterials such that individual 2D nanosheets could bonded together to construct three-dimensional (3D) architectures, thus avoiding the aggregation of individual 2D nanosheets [16]. This is important for preservation of these 2D nanomaterials' connatural properties in the bulk and promoting their applications in practical. More recently, with the recognization of the tremendous interest of these 2D structures, scientists noticed that the performance of certain devices could be significantly improved by utilizing 3D architectures and/or aerogels due to the increase of unit activity of the materials [17–19]. On the other hand, the development of methods for controlling the organization of functional objects on a nanometre scale to build larger objects is of fundamental and technological interest. Especially, 3D graphene networks in the form of foams, sponges and aerogels have attracted much attention [20–22]. Zhi et al. reviewed 3D graphene-based composites had attracted significant attention for lithium ion battery applications due to their unique structures and attractive properties in the past few years [23]. Shi et al. summarized the synthesis of graphene based functional gels with desired 3D interconnected porous microstructures, including hydrogels, organogels, aerogels, and their composites, which had demonstrated great potential applications in the fields of energy storage and conversion, environmental remediation and bio-related systems [24]. Feng and his colleague described the typical preparation methods for graphene materials with micro-, meso-, and macro-porous structures, and discussed the structure-property relationships and the application of these porous materials in enhanced electrochemical energy storage and conversion [25]. These 3D structures provide graphene materials with large pore volumes, strengthened mechanical properties, high specific surface areas and rapid mass and electron transport, due to the combination of the excellent connatural properties of graphene materials and the 3D porous structures [20,26–30].

Until recently, other kinds of 2D graphene analogues, including hexagonal BN (*h*-BN), carbon nitride, transition metal dichalcogenides, etc. derived from their layered bulk crystals [13,31–34], have also been extensively investigated because of their promising characters and potential applications, such as catalysis, electronics, optoelectronics, energy storage devices and so on [1,35–44]. Chen et al. had present inorganic graphene analogues and their concomitant advantages for lithium ion batteries electrodes, summarized general preparation strategies, and discussed the performances of their composites as lithium ion batteries electrodes [45]. Yu and his collaborators provided a summary on the liquid-phase synthesis, modifications, and energy-related applications of 2D nanostructured metal chalcogenide materials [46]. Of course, these inorganic graphene analogues not only can be used in energy storage, they also have a wide range of applications in other fields recently [47]. The appealing physical, chemical and electronic properties of these 2D graphene analogues rise a variety promising potential applications, including, catalysis, sensors, biomedicine, electronic/optoelectronic devices, and energy storage and conversion [13,48,49]. Moreover, manipulating advanced nanocomposites by combination of two or more materials is the most fascinating approach to tackle the weaknesses of individual components while optimize their performance or even generate new functional properties for practical applications [50,51]. A number of materials, such as noble metals [52–57], oxides [58–62], polymers [63–67], metal chalcogenides [68–74], carbonaceous materials [75–80], and so on [81–83], have been demonstrated to hybridize with 2D graphene analogues to generate functional hybrid nanoarchitectures. Zhang et al. have introduced the recent progress in hybrid nanoarchitectures based on 2D transition metal dichalcogenides nanosheets [84,85], moreover, they also summarized the preparation, characterization, and applications of 2D nanomaterials on 1D and 3D templating structures to form porous hierarchical architectures [51]. Very recently, more research is biased in favor of the aerogels have highly porous and ultrafine 3D networks consisting of 2D materials (graphene, transition-metal dichalcogenides, *h*-BN, and others 2D nanosheets) with high surface areas, low densities, and high electrical conductivities [86–88].

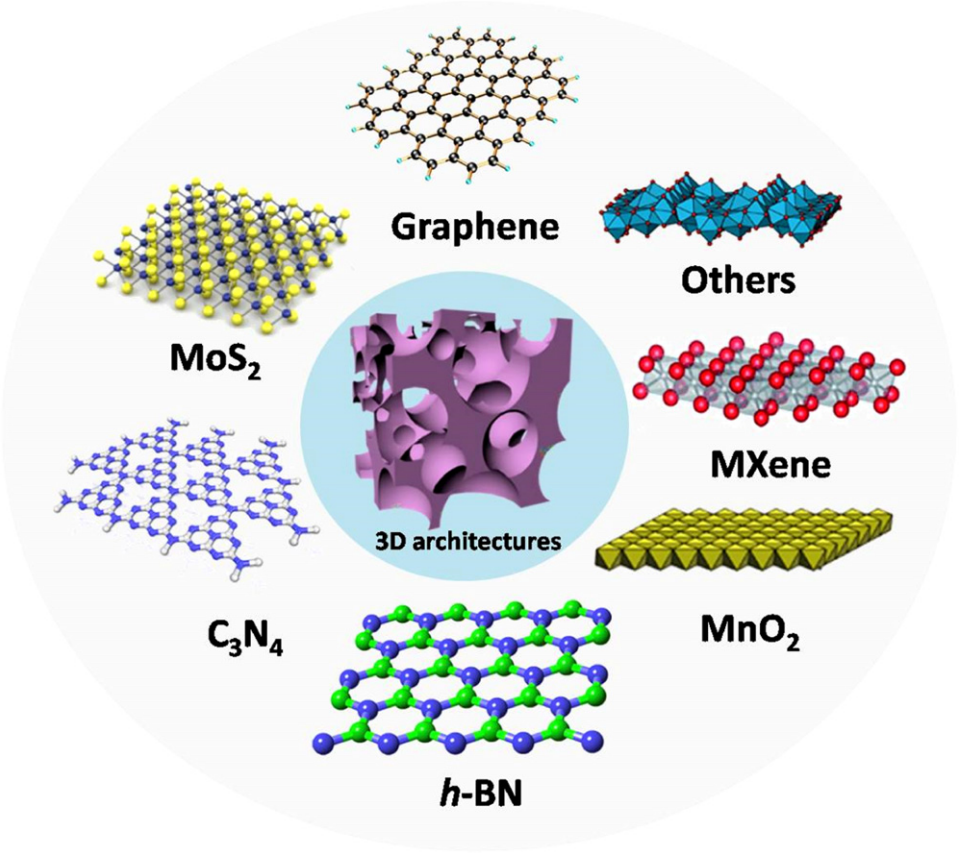

Fig. 1. Schematic illustration of 3D architectures based the classical 2D nanomaterials.

Although this review summarizes much of the historically significant work on 2D nanomaterials, the most recent developments are emphasized. The more prominently, this review aims to describe the different synthetic process used for preparation of 2D graphene analogues based 3D architectures and/or aerogels containing either any or their composites (Fig. 1), and the different application areas where the unique structure of these materials significantly enhanced the efficacy as compared to their 2D analogues or even opened a door for novel applications. We highlight recent developments in the synthesis 3D architectures methods from each classical 2D nanosheets, such as graphene, transition metal dichalcogenides, C_3N_4, *h*-BN, transition-metal oxides or hydroxides and so on. On these based, we further discuss their electrochemical applications for energy storage (including both supercapacitor and lithium ion battery applications), electrocatalysis, sensing and others. Finally, the conclusions and a forward-looking outlook of these emerging composites are discussed as well.

Graphene-based 3D nanostructure

In the past few years, a number of synthetic methods to fabricate 3D graphene-based networks with various morphologies, structures and properties have been developed, which are based on the strategies of either by growth directly from carbon source or by assembly of graphene oxide (GO) or graphene. These 3D structures provide graphene materials with strengthened mechanical properties, high specific surface areas and rapid mass and electron transport kinetics, due to the combination of the excellent connatural properties of graphene materials and the 3D porous structures. And these 3D structures could be applied in many fields. Here, we would focus on the latest advances in the fabrication and properties of 3D micro-/nano-architectures of graphene/GO-based materials.

Assembly of graphene

The assembly of 2D graphene oxide or graphene to form 3D nanostructure based on either physically or chemically linked to each other. As early as 2010, Wang et al. prepared 3D self-assembly of graphene oxide with low density and tunable macro- and microstructures via the hydrothermal method, which exhibited high conductivity and strength endurance despite the porous structure [89]. Henceforth, there were a lot of follow-up researches, and our group has also prepared a variety of 3D graphene-based networks [90,91]. Shi and his group developed macroporous graphene monoliths by hydrothermal reduction of emulsions formed by shaking mixtures of hexane and an aqueous dispersion of GO to form a graphene gel containing hexane [92]. We prepared the 3D foam architecture of ultrafine TiO_2 nanoparticles embedded in N-doped graphene networks via a facile hydrothermal self-assembly (Fig. 2a) [93]. The obtained 3D graphene foam dominated a macro/mesoporous structure with large surface area and high-level nitrogen content (7.34%). Such unique hierarchical structure processed multi-dimensional electronic networks, numerous open channels for the access of the electrolyte, and enlarged contact area between electrolyte and electrode, and thus favoring diffusion kinetics for both electrons and lithium ions. Meanwhile, electrochemical activity and electrical conductivity of the composite during electrochemical processes could be further improved by nitrogen doping. In addition, we also prepared the ternary nanocomposites graphene-TiO_2-SnO_2 by the hydrothermal two-step method [94]. Niu et al. described these prepared 3D graphene areogels immersed into the cetyltrimethylammo-

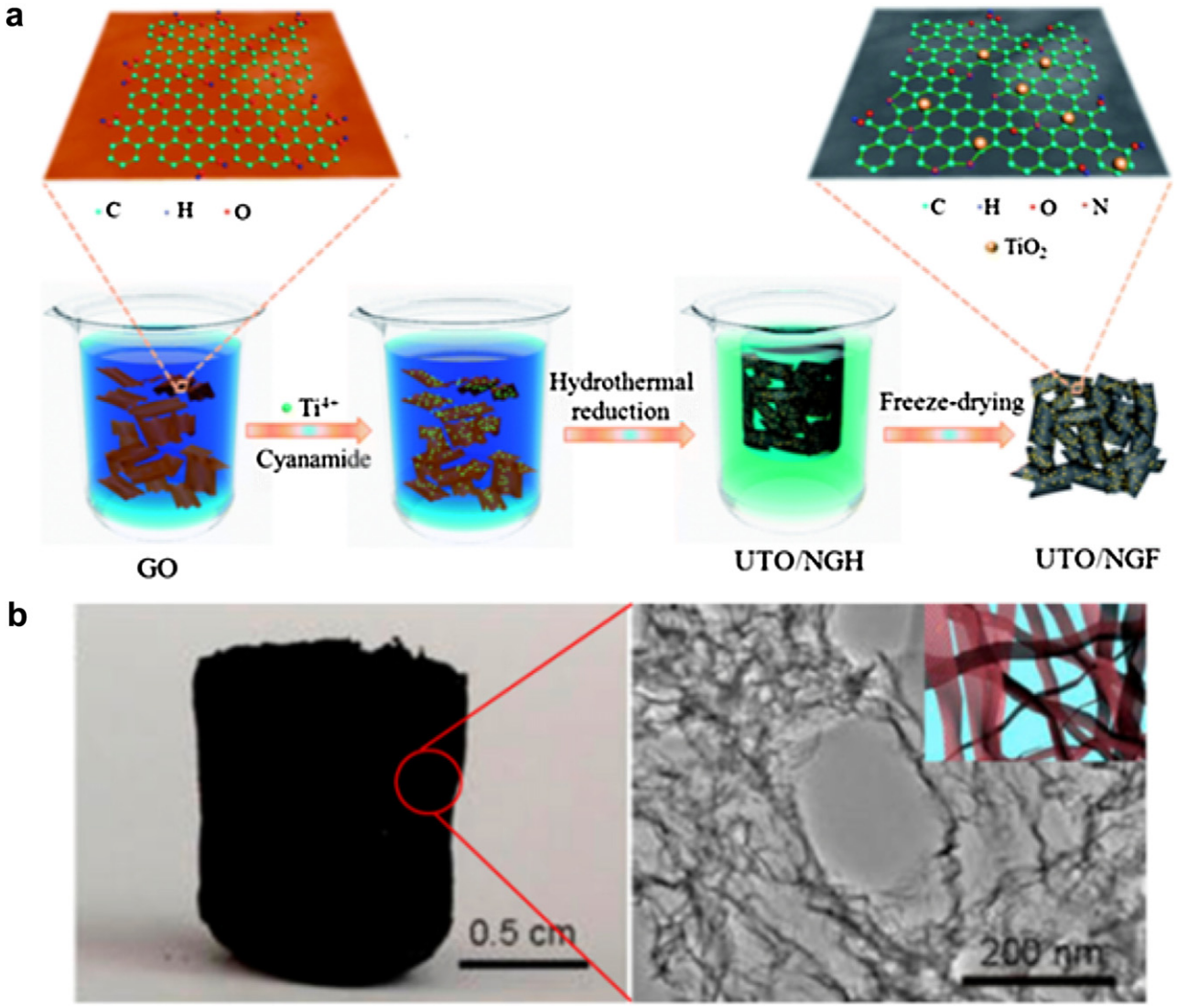

Fig. 2. (a) Schematic illustration for fabricating ultrafine TiO_2 nanoparticles/N-doped graphene foams. Reproduced with permission from Ref. [93]. Copyright 2014, Royal Society of Chemistry. (b) Photograph showing the morphology of boron- and nitrogen-codoped graphene nanoribbons aerogels, and TEM image of the boron- and nitrogen-codoped graphene nanoribbons aerogels showing its 3D porous structure, inset is the schematic diagram.
Reproduced with permission from Ref. [101]. Copyright 2015, American Chemical Society.

nium bromide (CTAB) solution. The alkyl chain of the CTAB was channeled to the graphene aerogels, and leaving the Br^- pendant toward the solution. Then, the Br^- reacted equally with the Ag^+, which caused a homogeneous in situ growth of AgBr nanoparticles (NPs) on the surface of the hierarchical pores [95]. Qu et al. [96] employed the counter-diffusion method to directly deposit metal-organic framework on 3D graphene obtained by hydrothermal method. Yu et al. developed a low-temperature hydrothermal route to synthesize the resorcinol-formaldehyde and graphene oxide metal compressible aerogel, using GO sheets as template skeletons and metal ions (Co^{2+}, Ni^{2+}, or Ca^{2+}) as catalysts and linkers [97]. Gogotsi et al. synthesized ultralight, conductive, and magnetically responsive 3D graphene aerogels decorated with Fe_3O_4 nanoparticles (Fe_3O_4/GA) by self-assembly of graphene with simultaneous decoration by Fe_3O_4 nanoparticles using a modified hydrothermal reduction process [98]. And the ultralight magnetic elastomer demonstrated excellent field-induced strain and adjustable electrical resistance, which can be exploited for its applications in smart soft actuators, microsensors, and switches, remotely controlled oil absorption, and recycling, to name a few. Zhou et al. [99] demonstrated $MnCO_3$/large-area graphene composites via the solvothermally treatment, whose large-area character enabled them to self-assemble face-to-face into orderly packed electrodes. However, the major limitation of previous studies of 3D graphene hybrids is that the graphene aerogels were prepared by freeze-drying of the hydrogel precursor, which would disturb the initial microstructure of the graphene networks, and thus prevent the achieving of full potential of the 3D graphene. The convenient solvent-exchange-induced preparation of solvated graphene frameworks where the stacking of graphene layers and the initial microstructure within the pore structures are notability different from that of unsolvated graphene frameworks [100]. In addition to the use of graphene nanosheets, Ajayan et al. further prepared graphene oxide nanoribbons aerogels by the hydrothermal treatment in aqueous solution (Fig. 2b), the graphene oxide nanoribbons were prepared by unzipping multiwalled carbon nanotubes with a solution-based oxidative process [101]. And then the prepared aerogels doped boron and nitrogen by the subsequent employment of boric acid and ammonia, the resulting products possessed abundant edges, thin walls, tunable

BN content, and multilevel porous structures. Yi et al. [102] fabricated 3D nitrogen-doped graphene nanoribbons aerogel via the hydrothermal method, which exhibited an ultra-low density, large surface area, and good conductivity.

Layered graphene hydrogel membrane, another self-assembly of graphene, was fabricated by vacuum filtration of dispersed chemically converted graphene colloid solution through a filter membrane. The self-supporting and flexible graphene hydrogel membrane can be readily peeled off from the filter and were stored in water before following experiments [103]. The thickness of graphene hydrogel membrane was readily tunable via filtrating desirable amount of chemically converted graphene dispersion with a fixed concentration. The interlayer water, as well as the electrostatic interactions associated with the polarized groups, serves as an effective spacer to counterbalance the interlayer van der Waals attractions that prevents the restacking of graphene sheets. In multilayer graphene oxide, mobilized protons can change path from one layer to the surrounding layers through nanopores, which results in increased conductivity [104]. Proton mobility and hydrogen bond reformation in single- and multilayer graphene oxide films is supported by single and double graphene oxide walls, respectively. Our group on this basis demonstrated the novel graphene/Co_3O_4 composite paper [105]. The graphene nanosheets were deposited onto the Co_3O_4 fibers and forms a coating under controlled infiltration by filtering the graphene oxide solution and modified electrospun Co_3O_4 fibers through membrane filters (Fig. 3). The flexible structure of carbon scaffold and the strong interaction between graphene and Co_3O_4 fibers are beneficial for efficiently preventing volume expansion/contraction and aggregation of Co_3O_4 during the Li charge/discharge procedure. Therefore, such composite paper could be suitable for effectively utilization of the good conductivity, mechanical flexibility, expectation electrochemical performance of graphene, and also for the large effective electrode/electrolyte contact area, and short average path length for Li transport. In addition to the above graphene/inorganic hybrid membranes, alternating stacked graphene-conducting polymer compact membranes were made by alternate deposition of electrochemically exfoliated graphene and mesoporous graphene-conducting polymer nanosheets [106].

Wei et al. [107] prepared the freestanding 3D porous graphene membrane with high flexibility and interconnected pores via vacuum filtration, and $CaCO_3$ particles formed in situ in graphene oxide dispersion were used as the template to facilitate the formation of the porous structure, which was a sacrificial template that can be removed easily by dilute acidic solution. By utilizing such skeleton as a substrate, PANI nanowire arrays grew on both the inner and outer surface of 3D porous graphene by a diluted polymerization procedure. Such as cast drying [108], electrophoresis deposition [109], traditional electrostatic layer-by-layer (LbL) assembly [110], spreader coating [111], other methods for preparing these graphene-based nanohybrid membranes had been developed in the past two years. Our group demonstrated a novel strategy for the fabrication of a reduced graphene oxide-encapsulated multifunctional magnetic [112] and mesoporous Co_3O_4 [113] composite microspheres by an electrostatic layer-by-layer self-assembly.

Unlike traditional preparation methods, 3D printing is widely considered a revolutionary manufacturing technology, with significant promise in a broad range of fields. For the implementation of the next generation of graphene-based devices, 3D patterning of graphene nanostructures will be the hot research. Seol and coworkers developed the nanometer-scale 3D printing approach which utilizing a size-controllable liquid meniscus to print freestanding reduced graphene oxide wires without any additional supporting materials [114]. Graphene oxide nanowires were locally grown at room temperature by utilizing the meniscus shaped at the tip of a micropipette that filled with a colloidal suspension of graphene oxide sheets, and was then reduced by thermal or chemical treatment with existence of hydrazine. Graphene oxide deposit was obtained by pulling the micropipette for the rapid evaporation of the solvent, which enables the growth of graphene oxide wires. The radius of the reduced graphene oxide wire was precisely controlled by adjusting the pulling rate υ of the micropipette, and minimum radius could reach ca. 150 nm. They also prepared arrays of different freestanding reduced graphene oxide architectures: bridges, straight wires, woven structures, and suspended junctions. Every structure could be grown directly at the chosen sites with the precision of 250 nm. Shah et al. presented the 3D printable graphene inks, which comprised graphene flakes and the biocompatible, biodegradable, and hyperplastic polyester polylactide-co-glycolide [115]. These 3D printable graphene inks could be written at room temperature via extruding into self-supporting, customized structures with accuracy and fidelity. The resulting robust graphene structures were plastic in nature, with thin constructs showing high flexibility. Branched copolymer surfactant had been used to modified graphene to create "responsive" sheets whose interaction in water can be regulated using an external stimulus in the case pH [116]. And they were formulated water-based inks with their viscoelastic properties optimized to print self-supporting 3D structures through nozzles with diameters ranging from 500 down to 100 μm. Worsley et al. reported the fabrication of periodic graphene aerogel micro lattices with modulated architecture via the 3D printing method known as direct ink writing [117]. Such 3D printed graphene aerogels have good properties including highly conductive, lightweight and supercompressibility (up to 90% compressive strain). Furthermore, the Young's moduli of the 3D printed graphene aerogels showed tens fold of improvement compare to bulk graphene materials with similar density distribution and dominate large surface areas. Utilizing the 3D printing method to generate graphene aerogels brings new fields of complex aerogel architectures for a wide range of applications.

Some other self-supporting graphene materials were prepared by one-pot spray pyrolysis. These 3D porous graphene materials were directly prepared by spray pyrolysis at high temperatures. For instance, the 3D porous graphene-SnO_2 microspheres were formed from single droplets [118], the ultrafine SnO_2 nanocrystals were found to be randomly distributed inside the individual graphene nanospheres consisted of layered graphene. The size of the individual graphene nanospheres for the construction of 3D porous microspheres could be easily controlled by tuning the size of the polystyrene nanobeads as sacrificial templates while the content of the SnO_2 active material could be the adjusted by changing the concentration of the tin salt dissolved in the spray solution. Graphene-wrapped Fe_2O_3 composites with a 3D hierarchical structure has been made by a facile and efficient spray drying route with a following mild heat reduction in air [119]. Interestingly, another novel method utilized an anti-solvent to fabricate non-stacked reduced graphene oxide directly from non-stacked graphene oxide, which was found to be the easiest, safest and most efficient strategy [120]. The nonpolar aprotic anti-solvent for the hydrophilic GO and hexane would not interact with any oxygen groups of GO, and thus could not disperse the GO sheets, causing a hydrogen bonding interaction of functional oxygen groups from different segments within GO, hence forbids the re-stacking of the GO sheets and resulting in the construction of a highly crumpled non-stacked GO powder.

Except the above self-supporting 3D graphene materials, there are other supporting materials, including metal foams or polymer skeletons. As we all know, nickel or copper foams are often used as current collector. Due to their large porous and continuous structure, graphene-based materials attached to them to form 3D multi-level micro-/nanostructures. As shown in Fig. 4, a new nanohybrid material was displayed, which made up of graphene supported mesoporous single crystal Si on Cu foam

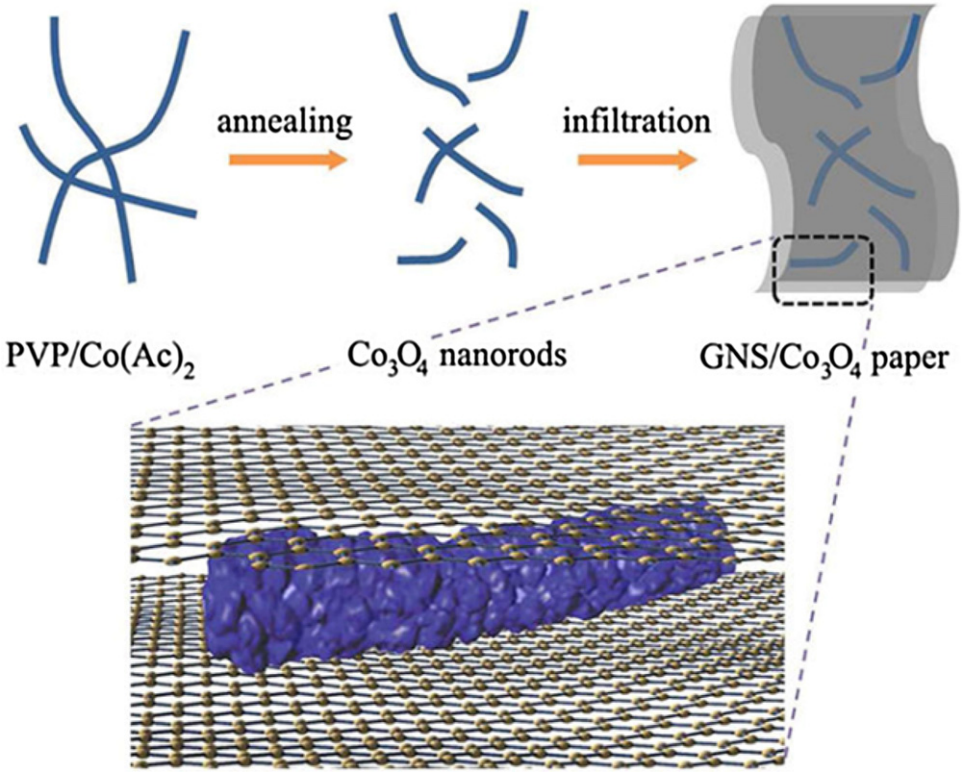

Fig. 3. Fabrication of graphene nanosheets/Co_3O_4 fiber composite paper.
Reproduced with permission from Ref. [105]. Copyright 2013, American Chemical Society.

by a facile method [121]. Firstly, mesoporous single crystal Si was prepared by boron doping, followed by silver nitrate etching of the pristine Si nanoparticles. The obtained mesoporous single crystal Si is then dispersed in ethanol, alternately dip-coating on the Cu foam with the GO suspension. After reduction by hydroiodic acid, graphene supported mesoporous single crystal Si on Cu foam are finally obtained. Hereafter, ternary polyaniline/SnO_2/graphene nanohybrids were successfully developed by a simple dip-coating of SnO_2@polyaniline and graphene dispersion on Cu foam [122]. Mai et al. designed and elaborated one special interwoven 3D frame architecture of cobalt oxide nanobrush-graphene@$Ni_xCo_{2x}(OH)_{6x}$ electrode materials through a facile modified hydrothermal method followed by two-step calcination and two-step optimized electrodeposition on the nickel foam [123]. Additionally, graphene and carbon nanotubes composites builded the 3D interpenetrating network structure [124]. Furthermore, the 3Dnanostructure comprised of ternary graphene/carbon nanotubes/MnO_2 nanocomposites was successfully developed [125], in which carbon nanotubes were grown within the graphene nanosheets layers by a simple chemical vapor deposition (CVD) forming provocative 3D nanostructures, and the MnO_2 nanoflakes were then loaded on this 3D structure. Carbon nanotubes were used as stabilizers or spacers between graphene layers in such architecture, forming a 3D conductive network, and therefore avoiding the aggregation of graphene as well as promoting electron transportation. Moreover, the as-designed nanostructures could also generate amounts of porous configurations, which may further shorten the diffusion path of ions.

As one of the conductive nanofillers, carbon nanomaterials, like carbon nanotubes (CNTs) and graphene (G), have attracted the attentions of researchers because of their superior electrical, thermal and mechanical properties. Jiang et al. [126] prepared silicon carbide nanowires@graphene sheets with 3D structure by high frequency heating, the unique structure endowed the high throughput transportation of phonon, resulting in excellent thermal conductive performances for polyimide composites. Wang et al. [127] have developed a method for the preparation of novel hierarchical porous nanocomposite based on graphene nanosheets/acidtreated poly(1,5-diaminoanthraquinone) supported by multi-walled carbon nanotube. To make full use of the intrinsic performance of graphene nanosheets, the graphene nanosheets/acidtreated multi-walled carbon nanotube had been mildly reduced using ^{60}Co γ-ray irradiation to effectively restrain the aggregation, to which the nanostructured poly(1,5-diaminoanthraquinone) is firmly deposited by π-π stacking. In addition, camphor sulphonic acid (CSA), which was not only a dopant for poly(1,5-diaminoanthraquinone), but also play the role of a soft template for the polymerization, had been utilized and obtained a perfect nanoporous structure for the nanocomposite. However, the strong Van der Wals forces and π-π interaction between carbon nanomaterials would induce aggregation in graphene-based polymer composites. Our group constructed uniformly dispersed conductive networks of carbon nanotubes and/or graphene by using special-designed method. Then, high-quality conductive polymer composites were successfully prepared by infiltrating these networks with polymer. Meanwhile, we also creatively designed a porous polymer substrate, and combined it with 3D conductive network of carbon nano-materials. The carbon nanotubesand graphen were prepared into 3D carbon aerogel structures by using organic sol-gel method [128]. The stable structure has high porosity, can supports 10300 times its weight. The connection of nanotubes/graphene/carbon nanoparticles can improve the stability of structure, after infiltrating with poly(dimethylsiloxane) (PDMS), the stretchable and conductive materials with high conductivity can be successfully obtained. During stretching process, nanotubes absorbed slid past one another would still contact on the conductive sheet and that would retard the conductive pathway damage to a great extent. We reported a novel and facile method

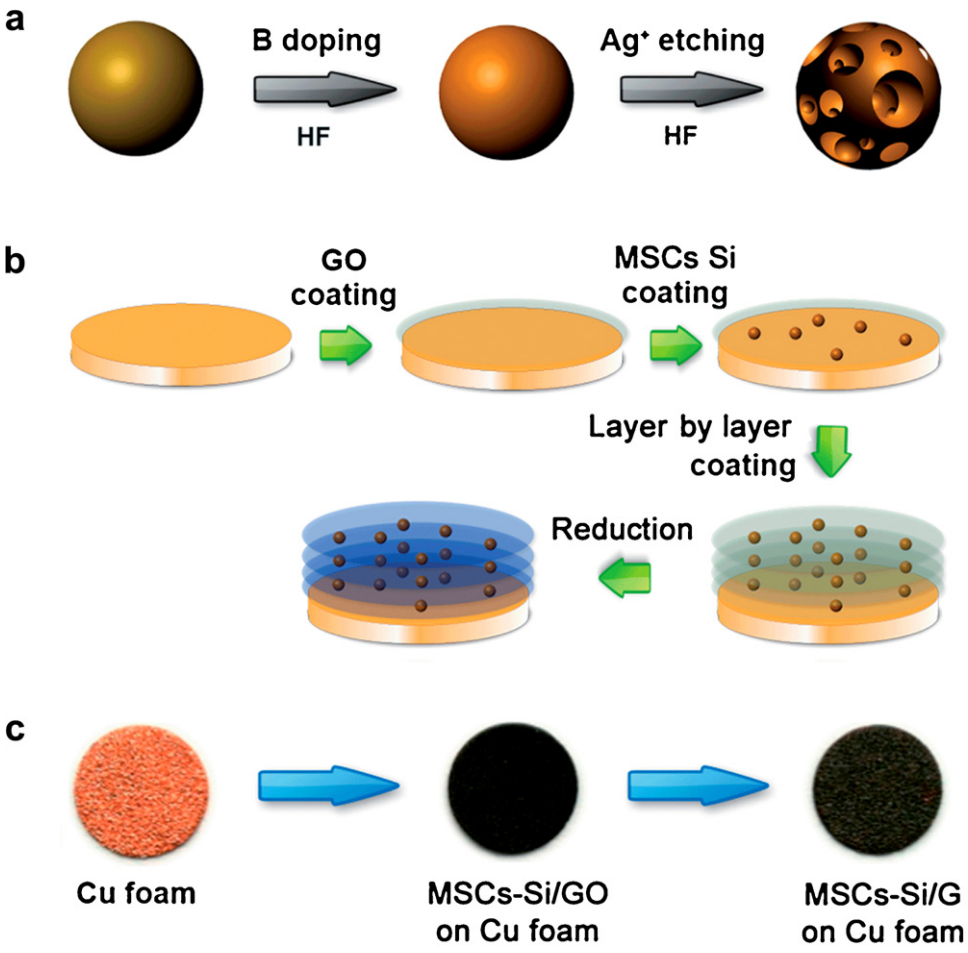

Fig. 4. Schematic illustration of (a) the preparation of mesoporous single crystal Si nanoparticles, (b) the preparation process of Si/Graphene nanohybrids on Cu foam, and (c) the corresponding photographs of anodes.

Reproduced with permission from Ref. [121]. Copyright 2014, Royal Society of Chemistry.

for manufacturing a new stretchable conductive material that integrates 3D carbon nanotubes/reduced graphene oxide network with porous PDMS (p-PDMS) elastomer (pPCG) (Fig. 5a) [129]. This reciprocal architecture alleviates the aggregation of carbon nanofillers while significantly enhances the conductivity of pPCG under large strains. The simulation of the mechanical properties of the p-PDMS model demonstrated that local rotations and bending of cell walls of the material enables it to accommodate an extremely large applied strain. Of course, there is more research about graphene aerogels crosslinking by phenolic resin [20,97,130]. A layer of silicon has been successfully coated onto 3D graphene/CNTs aerogels (CAs) framework with face-to-face contact and balanced open void by CVD method. The designed contact interface between CAs and Si provides high-efficiency paths for the fast electrons and lithium ions transport. With the help of balanced open-void, the free expansion of Si during cycling which maintaining high structural integrity because of the robust mechanical strength of 3D CAs framework (Fig. 5b) [130].

Synthesis of 3D graphene-based nanostructure

CVD is a facile method to produce graphene with controlled sizes and layers. Generally, conventional CVD process for graphene growth utilizes flat metal substrates as catalysts, and 3D graphene networks could be grown by CVD using pre-fabricated 3D metal substrates (e.g. nickel foam) as the templates and catalysts [15,131]. After the removal of the nickel template by etch, the free-standing 3D graphene networks with tailored structures and properties remained. Cheng and his group first reported the synthesis of 3D graphene foams by CVD method using nickel foam as the template [131]. After then, the 3D graphene foams doped with hetero-atoms (e.g. N-doping, B-doping) were prepared by the CVD method with different sources [132], and other materials have also been used as templates to produce 3D graphene networks [133–137].

In this based, we further introduced conducting polymer (PEDOT:PSS) into 3D network of CVD graphene foam (GF), and the PEDOT:PSS layer can significantly improve the electrical property of CVD graphene by doping effect (Fig. 6a) [138]. Then, a highly conductive and stretchable composite was prepared by backfilling the 3D graphene-PEDOT:PSS skeleton with poly(dimethylsiloxane) (PDMS) (CGPP). The conductive network of CVD graphene is coherent and complete, and the PEDOT:PSS coating is homogeneous, no cracks appeared over all this framework. Wei and his group successfully synthesized 3D CNT/graphene hybrid materials by a two-step CVD process. High quality graphene was first synthesized on Cu foils by CVD, then transferred onto $Fe/Al_2O_3/SiO_2/Si$ substrates for the growth of vertical aligned CNT arrays by a second CVD process [139]. Then on this basis, they further developed a metal-embedded supported bifunctional catalyst to propose for the in-situ growth of aligned CNT/graphene sandwiches via a two-step CVD growth [140]. In detail, exfoliated vermiculites impregnated with Fe/Mo were utilized as bifunctional catalysts for in situ growth of aligned CNTs at 750 °C under C_2H_4 flow, and then graphene deposition was conducted at 950 °C in CH_4 atmosphere. Parallel

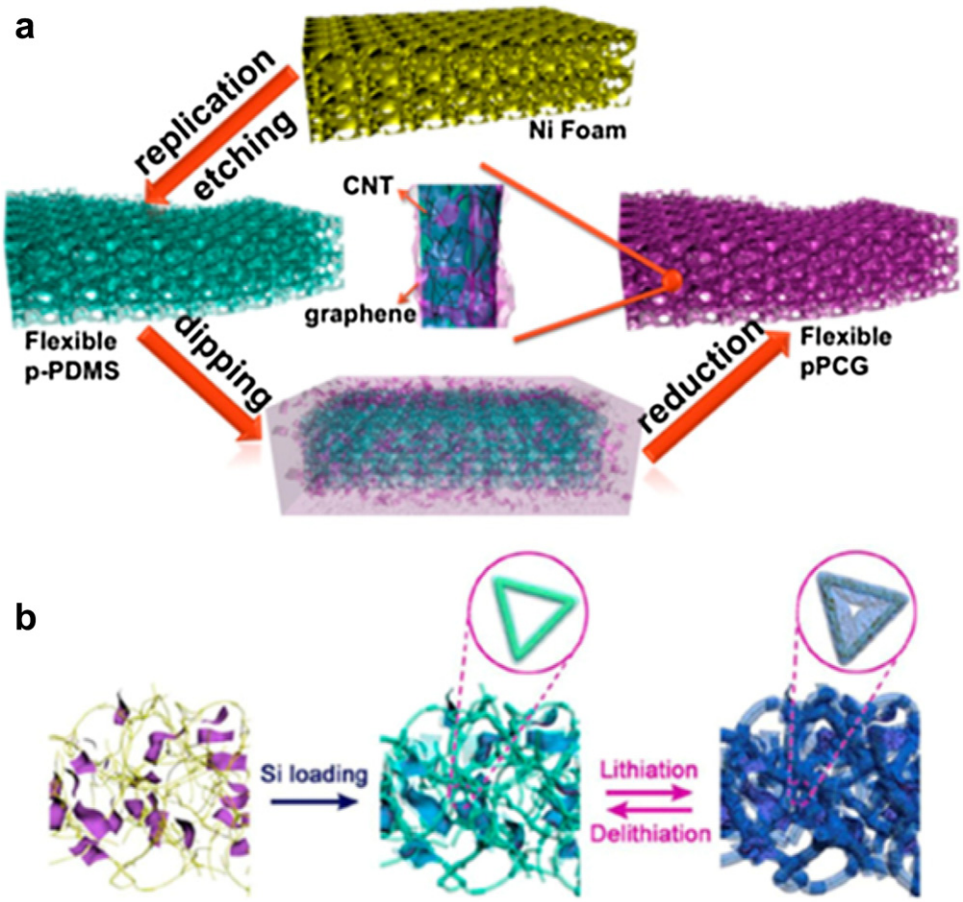

Fig. 5. (a) Schematic illustration of the pPCG preparation. Reproduced with permission from Ref. [129]. Copyright 2014, John Wiley & Sons, Inc. (b) Schematic illustration of the sample structures: Graphene/CNTs aerogels (CAs), Si/CAs nanohybrids, and Li^+-intercalated Si/CAs nanohybrids. Reproduced with permission from Ref. [130]. Copyright 2015, John Wiley & Sons, Inc.

graphene sheets are pillared apart by vertically linked aligned CNTs, leading to a 3D freestanding porous network, and NH_3 was simultaneously introduced during the CVD growth for the incorporation of nitrogen atoms into the carbon framework (Fig. 6b). Apart from the template-assisted CVD method, non-template approaches to directly grown 3D graphene networks have also been developed [141,142]. Chen et al. [142] reported the direct current plasma-enhanced CVD method to directly grow vertical graphene sheets on different kinds substrates, including stainless steel and Au. The vertical graphene sheets growth evolution consisted of three stages: the initial nucleation, the growth and connecting of graphite nanosheets on nanoislands, and further coagulation and agglomeration of as-grown graphite nanosheets.

Moreover, there are various graphene-based nanohybrids via different small molecules polymerization and carbonization. Bando and coworkers, inspired by an ancient food art of 'blown sugar', reported a sugar-blowing technique to grow the 3D self-supported graphene bubble network [143]. The 3D graphene bubble network was synthesized through the controlled heating of glucose and NH_4Cl (Fig. 7a). A molten syrup was gradually polymerized, whereas chemically released gases from NH_4Cl blew glucose-derived polymers, into plenty large bubbles, which features the sugar blowing. The bubble walls were gradually reduced by the gas release and flowing, surface tension induced removal of the macromolecules fluid out of the walls and leaching of small molecules from the macromolecules. The macromolecule walls were then graphitized into ultrathin graphitic layers at high temperature, resulting in a black foam-like 3D graphene bubble framework. This bubble framework was constructed with either mono- or several-layered graphitic membranes, which were rigidly fixed, tightly glued and spatially scaffolded by micrometer-scale graphitic struts. Such a topological configuration provides intrinsical structural interconnectivities, a highway for electrons/phonons to transport, a huge approachable surface area and robust mechanical properties. This approach is a facile method to synthesize 3D graphene analogues. Lu et al. presented a novel and general strategy referred to as "mussel-inspired surface chemistry" for the construction of 3D hierarchically porous N-doped carbon materials with a super-high surface areaby using polydopamine (PDA)-modified mixed cellulose ester filter films (MCEFs) as a sole template [144]. And in our group, multiple carbon nanohybrids were prepared by the carbonation polydopamine [145–150]. As a general approach, the prepared templates (e.g. nanostructured metals, metal oxides, SiO_2) were coated by the polydopamine due to surface polymerization, and then the resulting products were carbonized and reduced under high temperature in an inert environment. Meanwhile, for the generating of the mesoporous structures, the triblock copolymer PEO-PPO-PEO (P123) can be used during the surface polymerization assembly, which can be completely removed during the carbonization. As such mesoporous carbon nanohybrid materials, the outer mesoporous carbon shells not only construct the conducting pathway for the system's electron transfer but also prevent the inner nanoparticles from aggregation and pulverization. Our group also successfully prepared hierarchical porous carbon foams by poly(vinyl alcohol)/polystyrene (PVA/PS) hydrogel composites as in situ templates [151]. An illustration of the

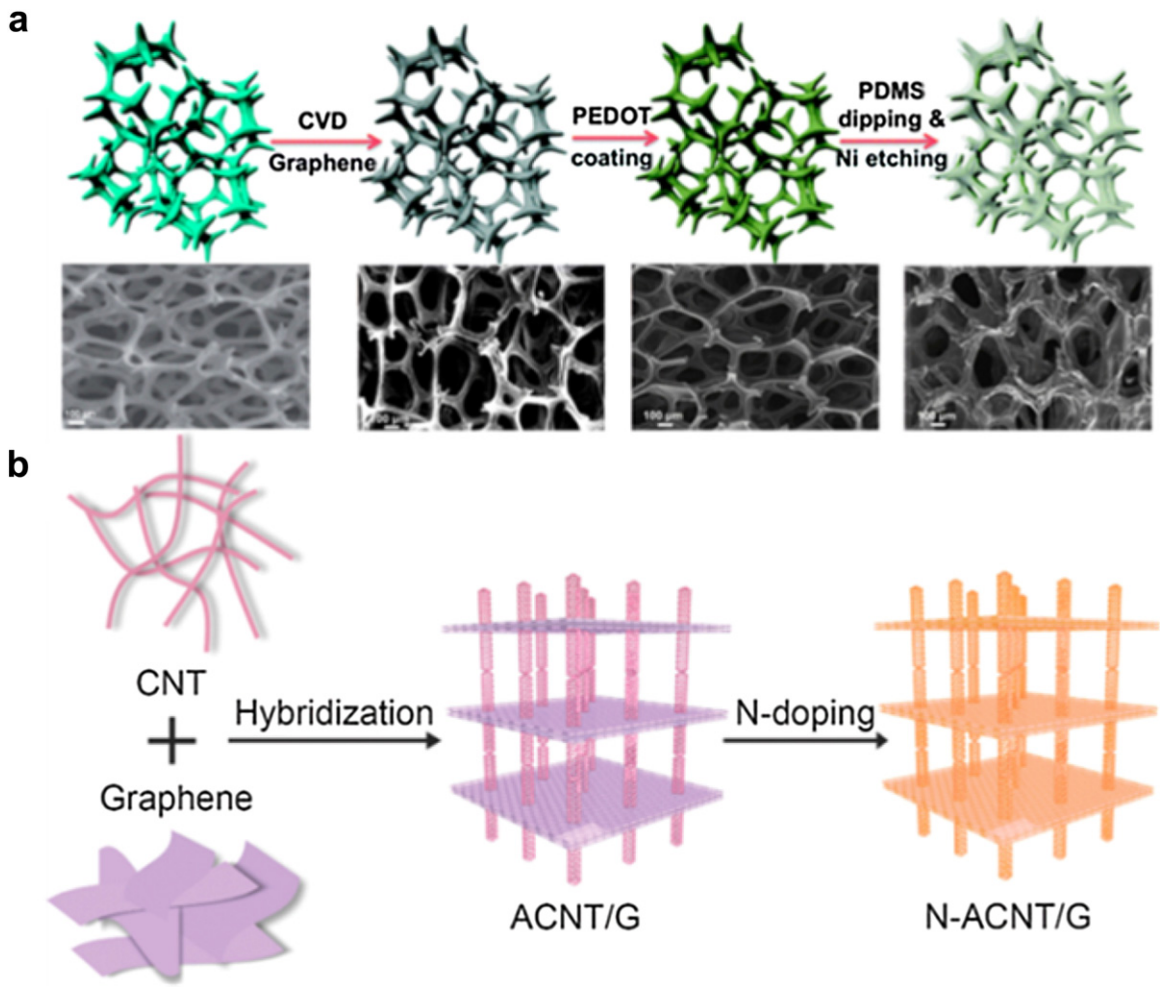

Fig. 6. (a) Schematic illustration of CGPP preparation; SEM images of Ni foam, graphene grown on it by the CVD method, the thin layer of PEDOT:PSS coated, and after backfilling the 3D graphene-PEDOT network with PDMS. Reproduced with permission from Ref. [138]. Copyright 2014, Royal Society of Chemistry. (b) Conceptual scheme of the design of N-ACNT/G hybrids with graphene and aligned CNTs as building blocks. Reproduced with permission from Ref. [140]. Copyright 2014, John Wiley & Sons, Inc.

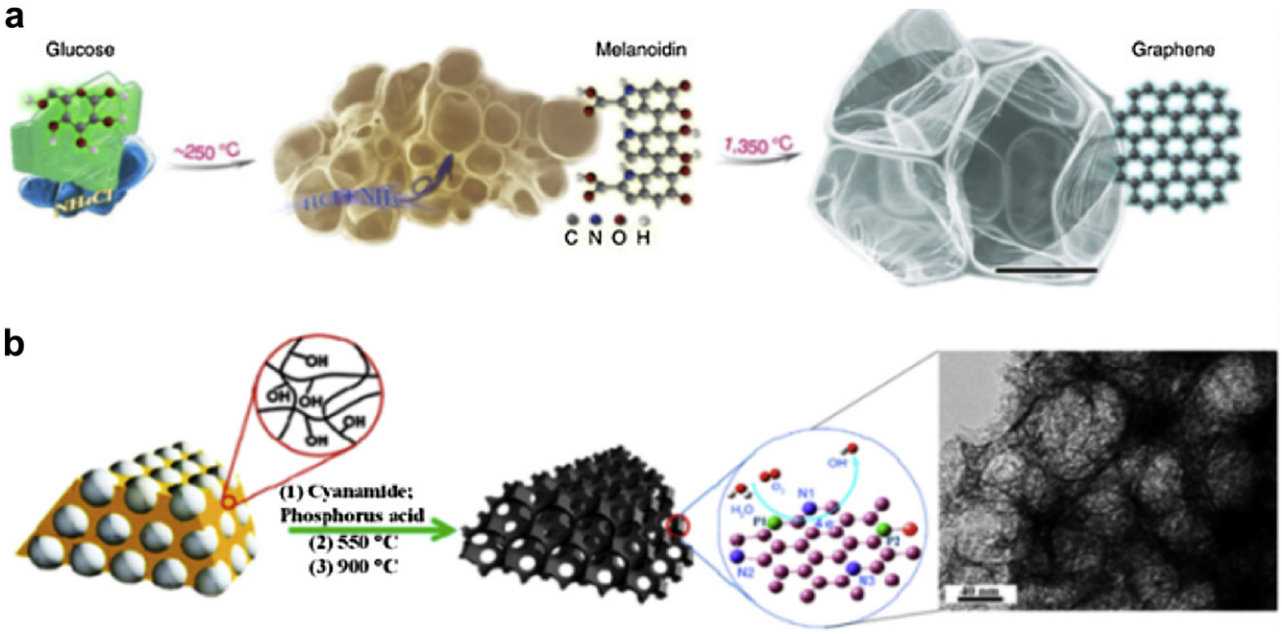

Fig. 7. (a) Growth process and structural regulation of sugar-blowing production. Reproduced with permission from Ref. [143]. Copyright 2013, Nature Publishing Group. (b) Schematic diagram of the fabrication of the HP-NPCs, and TEM image. Reproduced with permission from Ref. [151]. Copyright 2014, John Wiley & Sons, Inc.

fabrication process of hierarchical porous carbon foams is shown in Fig. 7b. The key feature of our strategy was the utilization of PVA hydrogel. For the fabrication of PVA/PS hydrogel-based templates, a free-standing composite monoliths could be formed by the embedment of PS spheres within PVA hydrogel through a well-known freezing-thawing cycling [152]. Moreover, the presence of PVA hydrogel results in enhanced hydrophilicity of the templates, therefore allowing the uniform infiltration through the templates. Most importantly, the abundant functional hydroxy groups on the PVA are favorable for the binding of metal ions or hetero atom [153,154]. The obtained products were dried and calcined. After then, we also prepared nitrogen and phosphorus dual-doped multilayer graphene with a high dopant content and well-developed porosity by utilizing a one-step solid-state reaction of glucose, urea and phosphoric acid [155]. This method leads to cross-linked and crumpled graphene sheets with a high dopant content and well-distributed porosity. Wang et al. [156] developed graphene quantum dots supported by graphene nanoribbons through a one-step template-free simultaneous reduction reaction of two reactants (i.e., methylbenzene and hexabromobenzene) by Na. The intimate contact between the graphene quantum dots and graphene nanoribbons could effectively prevent graphene quantum dots from aggregation, and more importantly, ensure efficient charge-transfers between them; both are advantages for oxygen reduction reaction electrocatalysis.

Feng and his group fabricated the novel graphene-based porous nanohybrids, compact 2D coupled graphene and porous polyaryltriazine-derived frameworks with tailormade pore structures, by using various molecular building blocks under ionothermal conditions [157]. Dynamic trimerization of aromatic polynitriles has guaranteed the syntheses of porous crystalline or amorphous covalent triazine frameworks [158]. The graphene-based 2D carbanions (RGONa) were fabricated by direct reaction between reduced graphene oxide and sodium in anhydrous tetrahydrofuran under ultrasonication. And then, the graphene-based 2D carbanions were utilized as initiators for the anionic polymerization of acrylonitrile on the surfaces of graphene, and thus affording polyacrylonitrile-functionalized graphene nanosheet (RGO-PAN) as a black powder. Finally, to achieve tailored pore structures, the desinged polymerization of diverse molecular building blocks was triggered on the surface of RGO-PAN in molten $ZnCl_2$ at different temperature (vacuum). Such porous nanosheets maintained nanoscale thickness, high specific surface area, and strong coupling of electroactive polyaryltriazine-derived frameworks after cooperated with graphene. Using in situ polymerization, polyaniline (PANI) nanofibers/3D graphene framework was prepared, and it obtained excellent supercapacitance performance [159–161]. Liu et al. reported the synthesis of vertically aligned PANI nanocone arrays on 3D graphene network by a template-free electrodeposition method [162]. The forming of PANI nanocone arrays was attributed to the electronegativity of PANI molecules and low current density. Anodic current was introduced to the 3D graphene network, and the surface of 3D graphene network was positively charged. Due to the acidity of electrolyte, aniline monomers exist in the form of Ph-NH_3^+ cation, and the electrostatic repulsion prevents them from approaching 3D graphene network surface.

Transition metal dichalcogenides-based 3D nanostructure

For over decades, layered materials have been investigated intensively, whereas the recent research focus on single-layered graphene in sheet fashion that triggered the increasing research efforts on this kind of materials because of many unique physicochemical properties resulted from the reduction of the graphene thickness to single or few layers. For instance, the indirect bandgap of bulk MoS_2 is 1.3 eV which could convert to a direct bandgap of 1.8 eV in its single-layer structure [163,164]. Various kinds of single- or few-layer transition metal dichalcogenides nanosheets have been successfully constructed for a range of applications [10,11,48,81,164–170]. However, with the development of 3D nanomaterials, transition metal dichalcogenides-based 3D nanostructure was also receiving considerable research interest. To date, a number of synthetic methods have been developed for the preparation of various classes of transition metal dichalcogenides-based 3D nanomaterials. Generally, these synthetic methodologies can be divided into two distinct categories, i.e. co-assembly and *in-situ* synthesis approaches.

Co-assembly transition metal dichalcogenides-based 3D hierarchical nanostructure

2D nanosheets, compared to a spherical structure of the same volume, could contribute much more to viscosity in their stretched state, and the channeled network from these 2D nanosheets would also assemble to the 3D hierarchical nanostructure. As the self-assembled graphene aerogels, transition metal dichalcogenides-based 3D hierarchical frameworks are also prepared by the self-assembly. While the first step was to prepare 2D graphene analogues, including mechanical exfoliation [31,171,172], liquid-phase exfoliation [35,173], ion-intercalation and exfoliation [33,36], chemical vapor deposition (CVD) [174–178], hydro-/solvo-thermal synthesis [32] and chemical solution-phase synthetic strategy [179]. The typical method is the mechanical-exfoliation approach, which was first used to produce graphene sheets. Geim et al. [31] successfully prepared several types of single-layer nanosheets such as graphene, $NbSe_2$, $Bi_2Sr_2CaCu_2O_x$, BN and MoS_2. Another method, chemical exfoliation of layered bulk crystals in liquid is one of the most developed strategies to synthesize 2D nanosheets, especially for the quantity production that is easy to control the crucial structural/compositional parameters of prepared 2D nanosheets. The intercalation of bulk transition metal dichalcogenides crystals by lithium ions (Li^+) have been proven to be an effectively high-yield production method of single-layer transition metal dichalcogenides nanosheets. As a typical paradigm, an electrochemical Li-intercalation and exfoliation method could be combined to precisely control the intercalation procedure and improve the product yield [33]. By using this method, single- and few-layer transition metal dichalcogenides nanosheets such as MoS_2, TaS_2, TiS_2, WS_2, ZrS_2, $NbSe_2$, WSe_2, Sb_2Se_3, Bi_2Te_3, and BN can be prepared in high yield and large scale [33,36]. Zhang et al. further reported a general method, that is, a combination of a grinding and sonication process, to prepare a number of layered transition metal dichalcogenides nanodots (e.g. MoS_2, WS_2, ReS_2, TaS_2, $MoSe_2$ and WSe_2), in high yield from the corresponding bulk transition metal dichalcogenides crystals at room temperature [180]. All the prepared transition metal dichalcogenides nanodots with sizes of less than 10 nm exhibited a narrow size distribution with high dispersity. To obtain small sized transition metal dichalcogenides nanodots, the in-plane bonds should be broken. Grinding [181] and Sonication [35,182] are two typical methods to reduce the van der Waals interaction of transition metal dichalcogenides, such that few-layer transition metal dichalcogenides nanosheets could be obtained [183]. Moreover, the shear/compress force of polishing and the powerful sonication could be able to break up the covalent chemical bonds and tear down the bulk crystals [181,184]. For instance, recently, high-yield black phosphorus quantum dots have been successfully fabricated from the bulk crystal form [184].

After mentioned top-down methods would be only applicable to the layered bulk materials. Alternatively, the bottom-up strategies including wet-chemical method and CVD growth, are

commonly used for the fabrication of transition metal dichalcogenides nanosheets. The CVD method can produce high-quality and large-area transition metal dichalcogenides nanosheets with atomic thickness. Such as, MoS_2 nanosheets can be deposited onto SiO_2 substrates by the CVD process [178,185]. By etching the SiO_2 substrate, the fabricated MoS_2 nanosheets could be transferred to arbitrary substrates for further characterizations and applications. Furthermore, large-area ReS_2 monolayers on a clean Si/SiO_2 wafer was also prepared by a similar CVD approach with ammonium perrhenate (NH_4ReO_4) and sulfur as the reactants at 450 °C [186]. Xie et al. [187] developed the synthesis of hexagonal ZrS_2 monolayer and few layers on hexagonal boron nitride (BN) using $ZrCl_4$ and S as precursors by the low-pressure CVD method. The number of layers of ZrS_2 was controlled by tuning the evaporation temperature of $ZrCl_4$. The stacking angle between ZrS_2 and BN characterized by transmission electron microscopy shows a preferred stacking angle of near 0°. Field-effect transistors (FETs) fabricated on ZrS_2 flakes showed n-type transport behavior with an estimated mobility of 0.1–1.1 $cm^2 V^{-1} s^{-1}$. They further synthesized triangular domains and continuous films of 2D $MoS_{2(1-x)}Se_{2x}$ ($0 \le x \le 0.40$) semiconductor alloys used the three-zone furnace, $MoSe_2$ and MoS_2 powders were put in the first and second zones, respectively, at temperatures of $T = T_1$ and T_2, respectively, and directly vaporized at high temperatures (T = 940–975 °C) [188]. Heterojunctions within monolayer $MoSe_2$-WSe_2 [189] and MoS_2-WS_2 [190] lateral nanosheets were also prepared by the CVD method with the different source.

Hydro-/solvo-thermal synthesis is expected to produce high quality 2D transition metal dichalcogenides nanosheets [32]. Previous results showed that single- or few layer MoS_2 nanosheets could be synthesized by the hydrothermal treatment of molybdic oxide and KSCN in deionized water at 453 K [32]. Interestingly, a high stable 1T-WS_2 nanoribbon with an unusual zigzag-chain type superlattice structure was also synthesized by the hydrothermal with ammonium tungstate hydrate and thiourea [191]. The ammonium ion-intercalated WS_2 ultrathin layers was revealed W–W reconstruction and W-S distorted octahedral coordination in the nanoribbons. The nanoribbons exhibited very distinctive features in electrical transport and Raman scattering properties.

In addition, a solution-phase synthetic protocol to form 2D single-layer transition-metal disulfide [179], called "diluted chalcogen continuous influx (DCCI)", which controlling the chalcogen source influx (e.g., H_2S) during the reaction with the transition-metal halide precursor is the critical parameter for the formation of single-layer sheets as examined for the cases of group IV transition-metal disulfide. The control of key synthetic parameters, which renders the continuous growth of lateral facets, is critical, and the dilute and continuous influx of H_2S plays such a role. The new synthetic principle can be potentially useful for the single-layer sheet formation of other 2D layered materials. Another novel method has been developed to synthesize the lamellar transition metal disulfide [192,193]. As general synthetic procedure, oleylamine and/or 1-octadecene is used as a high-boiling point coordinating solvent [194,195]. The synthesis started with dissolving and heating a transition metal precursor in a mixed solvent of oleylamine and/or 1-octadecene under N_2 atmosphere. The sulfur precursor (e.g. sulfur powder, CS_2) dissolved in oleylamine was injected into the resulting solution at high temperature (above 300 °C). Oleylamine has a high boiling point of over 360 °C, and elemental sulfur displays a considerable solubility in this medium [196]. Together, these properties make oleylamine an ideal solvent for the high-temperature solutionphase synthesis of sulfide nanocrystals [197,198]. The mode of reaction can be described as follows: (1) formation of an oleylammonium dithiocarbamate (either at room temperature or during injection); (2) thermal decomposition of the dithiocarbamate leading to an oleylammonium sulfide precursor [199,200]; and (3) reaction of the transition metal precursor with the sulfide ions to form transition-metal disulfide. After centrifugation and redispersion in the non-polar solvent, the nanostructures are colloidally stable but tend to partially aggregate over time. Cheon et al. [201] also demonstrated the single-layer nanosheets of MSe_2 (M = Mo, W) by the similar solution-phase growth approach. And the use of specific surface capping ligands with different binding energies to the reactive edge facets of transition-metal chalcogenides is the most important factor to produce thickness-controlled transition-metal chalcogenides from multi- to single-layer.

The self-assembly of above 2D nanosheets into 3D framework structures could mostly maintain the unique characters of individual 2D nanosheets and has recently attracted great interest for fundamental investigations and practical applications in diverse technologies. Kong et al. [86] reported a facile general approach for 3D aerogels from nanostructured 1D and 2D materials. This strategy for various material aerogels production includes three steps: (i) the preparation of a well-dispersed, individual nanowire/nanotube/nanosheet suspension; (ii) gel formation by controlled concentration increase from dilute suspension; (iii) aerogel formation of the gel through supercritical drying. Ajayan et al. demonstrated 3D architectures by adopting the 2D nanosheets of GO and MoS_2 as co-building blocks via their controllable assembly characters [202]. MoS_2 nanosheets and graphene oxide were firstly fabricated via liquid exfoliation and the modified Hummers method, then the prepared MoS_2 and graphene oxide nanosheets were then employed as building blocks to co-assemble by the hydrothermal process. Finally, graphene oxide in the resulting samples was chemically reduced to graphene, giving rise to MoS_2-graphene architectures with different MoS_2 content. The as-prepared MoS_2-graphene architectures possess a 3D structure with interconnected pores ranging from several nanometers to several micrometers. The sectional overlapping or connecting of flexible nanosheets might result from the cross-linking of the functional groups in graphene sheets (Fig. 8a), similar to those above-mentioned pure GO and graphene hydrogels. Liu and his group also demonstrated the similar porous hybrids by the ultrathin defect-rich MoS_2 nanosheets [203]. The crystal fringes along the curled edge of defect-rich MoS_2 nanosheets were discontinuous, which could be attributed to the existence of abundant defects on the surfaces of defect-rich MoS_2 nanosheets. Qiao et al. [204] fabricated a 3D van der Waals heterostructure via artificial assembly of 2D WS_2 nanosheets with almost 100% exposed surface atoms, and N-, O-, and P-doped graphene sheets via a vacuum filtration process, which featured utmost exposed active centers, continuous conductive network, highly expanded surface area, hierarchical porous structure, and strong synergistic effects between the components. Also the MoS_2 nanodots were embedded in the 3D porous frameworks of N-doped graphene via in-situ pyrolysis of glucose, a layered C_3N_4 sacrificial template and monolayer MoS_2 NDs [205].

Very recently, our group [206] also prepared a novel materials' design on the fabrication of 2D MoS_2/mesoporous carbon (MoS_2/m-C) hybrid nanostructure with ideal MoS_2/m-C atomic interface, in which single-layer MoS_2 and m-C are alternating ranged, by first the amidation of oleic acid (OA)-protected single-layer MoS_2 nanosheet with dopamine, then self-polymerizing dopamine in the interlayer of MoS_2, and finally annealing the obtained MoS_2/polydopamine (MoS_2/PDA) at high temperature (Fig. 9a). The MoS_2 nanosheets were prepared via hydrothermal synthesis by Na_2MoO_4 and thiourea precursors and modified by oleic acid. Such ultrathin hierarchical nanosheet superstructure could provide the perfect atomic interface contact between carbon nanosheets and single-layer MoS_2, resulting in the maximization of synergistic interaction. The strong interface synergistic effect of this intriguing architecture allows it work as a novel kind of anode

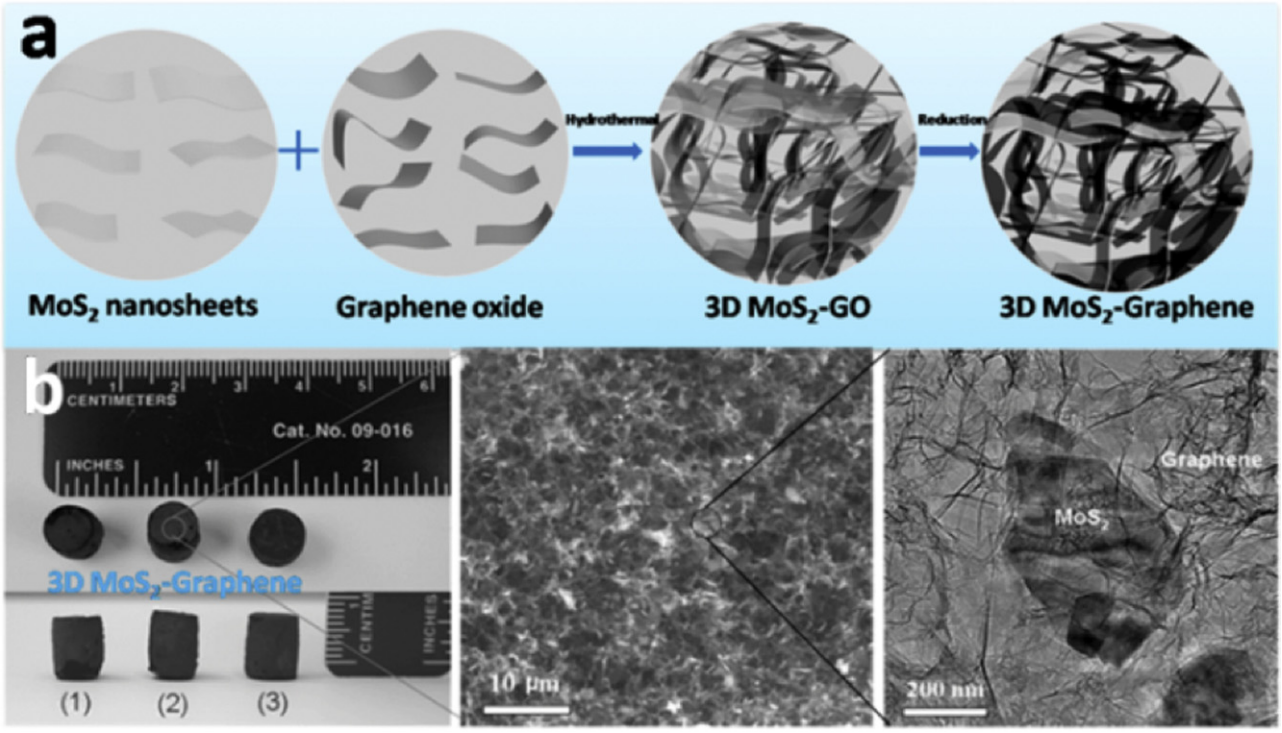

Fig. 8. (a) Schematic illustration for the fabrication of 3D MoS2-graphene framework, which mainly involves three steps: firstly, MoS_2 and graphene oxide nanosheets were prepared by liquid exfoliation and Hummers methods, respectively; then, the mixture of MoS_2 and GO nanosheets in IPA (Isopropyl alcohol)/water (1:2, v/v) was hydrothermal treated at 180 °C for 12 h; finally, chemical reduction of GO to produce 3D MoS_2-graphene structure. (b) 3D MoS_2-graphene architectures. Photographs of MoS_2-graphene architectures with different concentration of MoS_2 nanosheets after chemical reduction and dryness; Typical SEM and TEM images of MoS_2-graphene architecture (84%). Reproduced with permission from Ref. [202]. Copyright 2014, John Wiley & Sons, Inc.

materials for developing LIBs with high power densities, very high energy, and extremely high stability. The first-principle DFT calculation of lithium storage on MoS_2/m-C nanosheet superstructure demonstrates that there should be an evident improvement for Li ion intercalated in the MoS_2/G (or MoS_2/G/MoS_2) atomic interface structure, in comparison with the isolated MoS_2 monolayer (or MoS_2/MoS_2 interface) (Fig. 9b). Especially, the MoS_2/r-G interface with a carbon vacancy provides a more prominent capacity to adopt Li atoms. The improvement could be attributed to the synergetic effect of the single-layer carbon and MoS_2 nanosheets. Meanwhile, using DFT calculations, the interaction of individual functional groups present in a rGO sheet were studied [207]. The interaction energy obtained from the optimized geometry for the rGO flake was about 0.85 and 1.06 eV as the sheet was functionalized with —O— and —OH groups, respectively. The energy gains due to the —OH group is thus about 1.24 times higher than the —O—. So the synergetic interfacial force between graphene and zirconia nanoparticles was explained, which was similar to our results.

Zhang et al. [208] reported a facile and universal approach for the high-yield and scalable preparation of chiral nanofibers based on the self-assembly of various ultrathin one dimensional and 2D nanomaterials in vigorously stirred polymeric solutions. The obtained chiral nanofibers can be further transformed to same-handed chiral nanorings. Various materials with different compositions or dimensionalities, such as metals (e.g., Au-Ag nanowires), carbonaceous materials (e.g. MWCNTs and GO), and semiconductors (MoS_2, TiS_2, TaS_2, $TaSe_2$, and WSe_2), can be assembled into chiral nanofibers with 100% left-handedness. Soon afterwards, they further reported the preparation of noble metal nanoparticles MoS_2 hybrid nanobelts by utilizing single- or few-layer MoS_2 nanosheets as the precursor [209]. By using polyvinyl pyrrolidone (PVP) as surfactant and complexing agent while benzyl alcohol as both solvent and reductant, the metal precursors (e.g., $AgNO_3$ and H_2PtCl_6) were instantly reduced on the MoS_2 nanosheets, and then the combined metal NP-nanosheet gradually transferred into metal NP-MoS_2 hybrid nanobelts. The formation of 1D soft-template from PVP through self-assembly is the crucial step for the fabrication of the metal NP-MoS_2 hybrid nanobelts [210]. Importantly, this method is universal and could be utilized to produce other transition metal dichalcogenides nanobelts such as TaS_2, TiS_2, WSe_2 and $TaSe_2$, decorated by noble metal NPs. In addition to the above-mentioned transition metal dichalcogenides-based nanobelts, flexible hybrid fibers were fabricated by incorporation of 2D MoS_2 and rGO nanosheets into wellaligned MWCNT sheets followed by twisting [211]. Three-layer-stacked MWCNT sheets were laid on a polytetrafluoroethylene (PTFE) substrate, and then 2D nanomaterials, such as GO nanosheets or single-layer MoS_2, could be drop-casted with a pipette and moved along the stacked MWCNT sheet. The amount of nanomaterial that introduced into the MWCNT sheet could be adjusted by repeating the casting process. The resulting hybrid sheet could be easily peeled off the PTFE substrate after being dried in vacuum. One end of hybrid sheet was fixed on a glass holder by using a scotch tape while the other end was fixed to an electric motor, thus the sheet could be twisted at a rotating speed of 200 rpm, and the hybrid fiber was obtained after 3 min. The resulting GO/MWCNT fiber was then transferred to the rGO/MWCNT fiber by reduction with hydroiodic acid (HI).

Accept these transition metal dichalcogenides-based nanomaterials, the more nanocomposites were designed and prepared, including inorganic nanoplate [212], conducting polymer [213] and noble metal nanoparticles [214]. Self-supporting 3D hierarchical nanostructure MoS_2@$Ni(OH)_2$ nanocomposites were synthesized via a facile single-mode microwave hydrothermal technique [212]. The flowerlike MoS_2 nanosheets were fabricated through microwave irradiation in a single-mode microwave reactor. The prepared flowerlike MoS_2 nanosheets were dispersed in a solu-

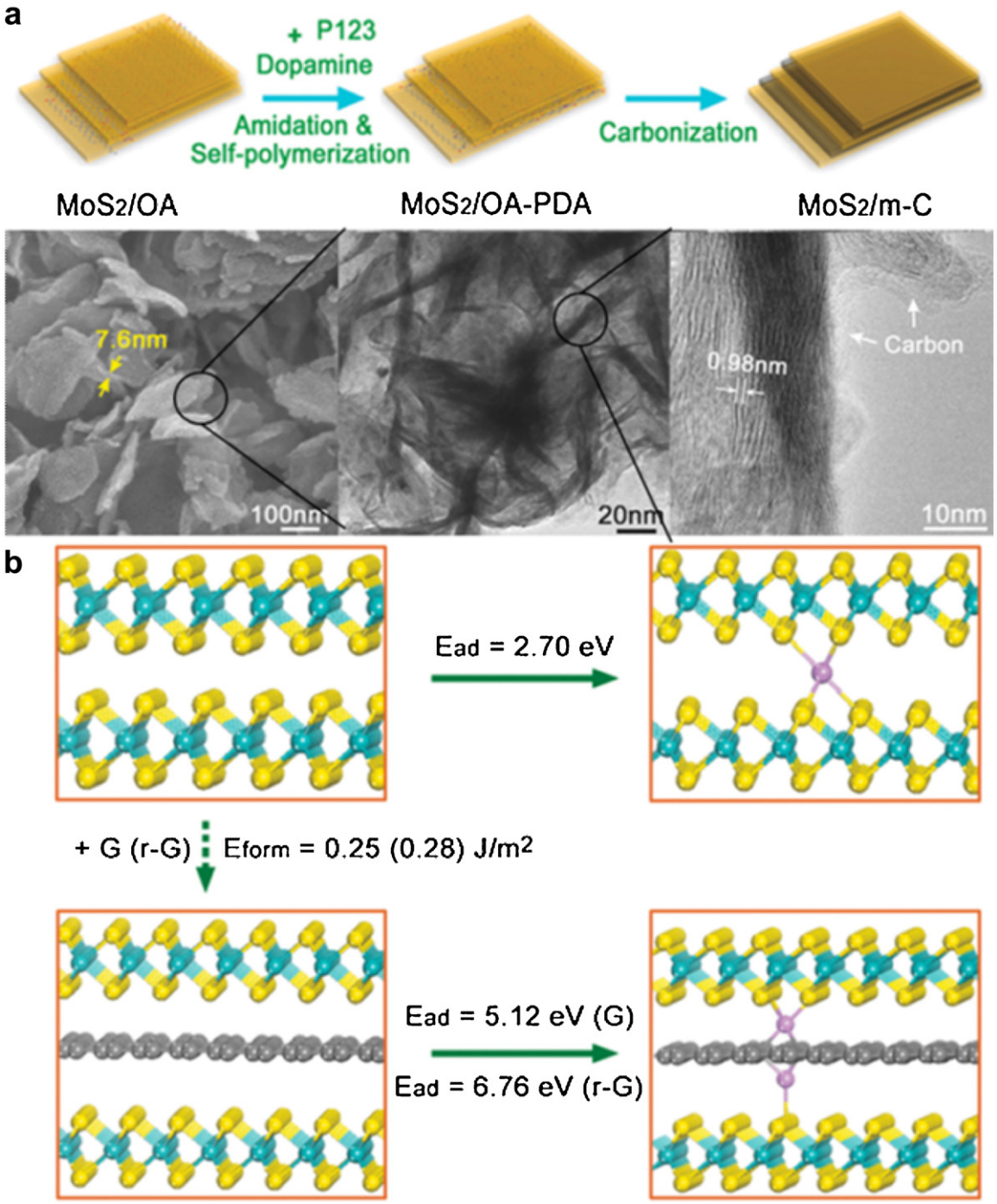

Fig. 9. (a) Schematic illustration on the synthesis process of the MoS_2/m-C nanosheet superstructure. Typical SEM and TEM images of the as-synthesized MoS_2/m-C nanosheet superstructure. (b) Lithium adsorption in MoS_2/MoS_2 and $MoS_2/G/MoS_2$ interlayer, respectively. Reaction energetics for $MoS_2/G/MoS_2$ interface formation and its synergetic effect in promoting Li storage.

Reproduced with permission from Ref. [206]. Copyright 2015, John Wiley & Sons, Inc.

tion including $Ni(NO_3)_2{\cdot}6H_2O$ and carbamide, and was treated at 180 °C for 3 h under single-mode microwave hydrothermal technique. During the reaction procedure, carbamide and nickel ion could easily move into the interfaces of the MoS_2 nanosheets, where the $Ni(OH)_2$ nanoplates were form on the MoS_2 nanosheets after the reaction. Tang et al. developed the nanocomposites of MoS_2 and polypyrrole by in situ oxidative polymerization of pyrrole monomers on single-layered MoS_2 in presence of ammonium persulphate solution [213]. By varying the ratio of MoS_2 monolayers to pyrrole monomers in polymerization procedure, the sandwich structured lamellar hybrid material consists of ultrathin-layered polypyrrole and MoS_2 monolayers with controllable thickness could be obtained. Exclusive and homogeneous polymerization on the 2D MoS_2 surfaces could occur because of the strong coordination interactions between N groups of pyrrole monomers and Mo ions of MoS_2 monolayers, and thus forms the sandwiched nanocomposites. An active system of plasmonic-metal Au nanorods/MoS_2 nanosheets hybrids was desired activity of catalysts toward hydrogen evolution reaction [214], it is essential to improve the efficiency of light adsorption of Au rods, the

electron–hole separation, and the transfer of intermediated hot electron from Au rods to MoS_2 active sites. Plasmon-excited hot electrons injection mechanism is an efficient and promising strategy to improve the catalyst activity. Through electron injection, the carrier density of catalysts can be adjusted to match the energy level of interesting reactions.

In-situ synthesis of 3D transition metal dichalcogenides-based nanomaterials

As previously described, there are many methods to prepare transition metal dichalcogenides nanosheets. And the different 3D nanostructures were designed and builded by these nanosheets. However, in earlier before, there have been a lot of researches about the directly 3D nanostructure transition metal dichalcogenides materials. For instance, by utilizing an atmospheric pressure chemical vapor deposition method with the reaction of chlorides and sulfur, MoS_2 and WS_2 inorganic fullerene-like (IF) nanostructures (onion-like nanoparticles and nanotubes) and elegant 3D nanoflowers (NF) could be successfully prepared [215]. Then using a facile liquid-phase solution method, 3D flower-like nanostructures of TiS_2 and 2D flake-like nanostructures of crystalline TiS_2 were synthesized [216].

3D $MoSe_2$ and WSe_2 porous microspheres, which are composed of the corresponding monolayer flakes, were also prepared by a facile colloidal route [217]. The solvents trioctylamine and oleylamine were found to play important roles in the formation of $MoSe_2$ microspheres, whereby trioctylamine determined the 3D microspherical morphology and oleylamine directed the formation of $MoSe_2$ monolayer flakes. Vertically aligned nanosheet heterostructures with partly reduced MoO_3 cores and adjustable MoS_2 shells were fabricated via two-step chemical vapor deposition [218]. Besides, 3D tubular architectures constructed by single layered MoS_2 were described through a mix-solution reaction where the size of the tubes could be adjusted by varying the kind of alcohol that mixed in the solution (Fig. 10) [219]. In a typical synthesis, S powder and ammonium molybdate was dissolved in the mixed solution of octylamine and ethanol, and then the mixture was solvothermal treatment at 180–220 °C for several hours. The as-prepared assembled tubes have a high specific surface area and mesopores resulting from the assembly of ultrathin MoS_2 layers (Fig. 10). In our group, very recently, we developed a reciprocal hybridization of MoO_2 nanoparticles and few-layer MoS_2 via a facile two step hydrothermal reaction [220]. The MoO_2 nanoparticles loaded on few-layered MoS_2 nanosheets can effectively avoid the restacking of MoS_2 nanosheets, and meanwhile promote the well-dispersion of MoO_2 nanoparticles on the surface of MoS_2 nanosheets, and hence it is a reciprocal hybridization.

Of course, similar to 3D graphene-based nanostructure, more hybrid transition metal dichalcogenides-based 3D nanostructure possessed the synergistic interaction between the main and guest materials. And their hybrid components are generally diverse, e.g. metal, carbon, polymer, inorganic semiconductors et al. For example, a core-shell molybdenum sulfide@dealloyed nanoporous gold composite was prepared by the nanoporous electrocatalyst via chemically plating a thin layer of amorphous molybdenum sulfide on the internal surface of dealloyed nanoporous gold [221]. Li et al. [222] developed the commercially available sponges as a template for loading MoS_x, where the sponges loaded with the ammonium tetrathiomolybdate precursor can be converted to 3D porous MoS_x after simple thermolysis processes with the gas mixture of H_2 and Ar. The 3D MoS_2 nanosheets (3D MoS_2-Graphene-Ni) structure was synthesized by a CVD process [78,223]. First, graphene was grown on the 3D Ni foam surface by CVD to form the 3D Graphene-Ni structure. And then the vapor of molybdenum and sulfur source started to react and MoS_2 nanosheets were deposited on the surface of graphene in the tube furnace. Another 3D MoS_2@C nanocomposites were prepared by the instant gelation [75]. Silicate sol with Mo precursors and carbon source was form a transparent semisolid "jelly". The 3D cross-linked network can be turned into a 3D $MoS_2/SiO_2/C$ dense network in a post annealing step. After the removal of SiO_2, 3D porous MoS_2@C nanocomposites are obtained [224].

The most commonly used materials for hybridization with hybrid transition metal dichalcogenides nanosheets to form hierarchical nanostructures are carbonaceous nanomaterials (including graphene, CNTs and carbon fibers) by the hydrothermal method. As a typical example, Chen et al. developed a facile process for the synthesis of layered MoS_2–graphene composites by an L-cysteine-assisted hydrothermal method with subsequent annealing treatment by using sodium molybdate, GO and L-cysteine as precursors [75]. The growth of the MoS_2 nanoflake arrays on the surface of the graphene sheets depends greatly on the hydrothermal reaction time [225]. MoO_4^{2-} was first produced in an alkaline solution and was then reduced to MoS_2 by thiacetamide under subsequent hydrothermal treatment. The graphene sheets serve as substrates for the nucleation and growth of MoS_2 during the hydrothermal process. Beside, the two-step hydrothermal synthesized the titania-based composite photocatalysts containing a layered MoS_2/graphene [226]. Mechanically robust and electrically conductive MoS_2/graphene 3D hierarchical frameworks were prepared by a one-step hydrothermal process with an aqueous dispersion of graphene oxide, ammonium molybdate, and thioacetamide [227]. The defect-rich MoS_2 nanosheets possessed an enlarged interlayer spacing due to oxygen incorporation from graphene oxides nanosheets. Furthermore, on the surface of the MoS_2 nanosheets one can see a defect-rich structure with nanodomains of short-range ordering, and the exposed molybdenum edges are likely the active sites. Liu et al. examined the stability and electronic structure of 3D graphene-MoS_2 hybrid structures using the first-principle calculations [228]. The results proved that 3D graphene-MoS_2 could easily self-assembled by zigzag MoS_2 nanoribbons and graphene nanosheet which are thermodynamically stable at room temperature. More importantly, 3D graphene-MoS_2 with zigzag MoS_2 nanoribbon not only own the large surface area and effectively avoid the aggregation between the different nanoribbons, but also can remarkably enhance Li adsorption interaction. Our group also developed 3D SnS_2/graphene aerogels by utilizing an in-situ macroscopy self-assembly method which embedded SnS_2 nanoplates into graphene sheets during a hydrothermal treatment [229], and the 3D monolithic architectures could be maintained after a freeze-drying process. Highly concentrated graphene sheets were easily restacked into 3D architectures driven by combined hydrophobic and π-π stacking interactions during hydrothermal reduction reaction, meanwhile SnS_2 facilitate stabilizing such novel graphene networks. The resulted 3D SnS_2/graphene aerogels revealed large surface area, interconnected graphene networks and large numbers of macropores. Also more complex nanocomposites have been studied and prepared. Chen et al. presented the fabrication and characterization of 2D porous g-C_3N_4 nanosheets/nitrogen-doped graphene/layered MoS_2 (CNNS/NRGO/MoS_2) ternary nanojunction [230]. Nitrogen-doped partially reduced graphene oxide (NPRGO)-based CNNS were first prepared by pyrolysis of urea on the surface of GO at 550 °C under an argon atmosphere. The CNNS/NPRGO hybrid was dispersed by the hydrothermal treatment in an aqueous solution of sodium molybdate and thiourea. Such structure provided a broadened optical window for effective light harvesting, short diffusion distance for excellent charge transport, as well as a large contact area for fast interfacial charge separation and photoelectrochemical reactions, which exhibited good photoelectrochemical and photocatalytic activities under visible light. Recently, flexible 3D nanoarchitectures have received tremendous

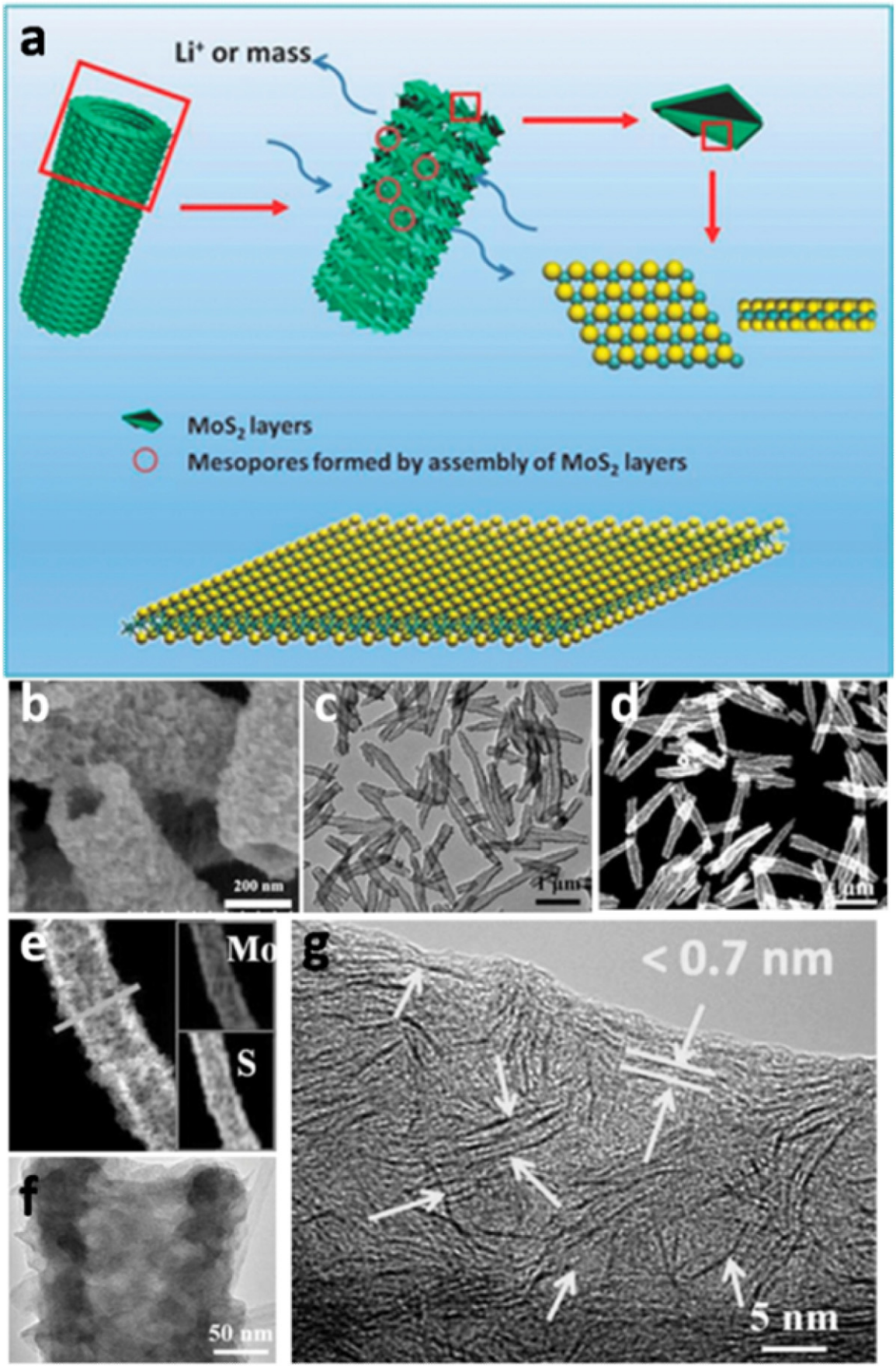

Fig. 10. (a) Schematic illustration of the 3D structures assembled by single-layered MoS_2 (top panel). Bottom panel shows the ball-stick model of a single-layered Mo S_2. SEM (b), TEM (c), and STEM (d, e) images show the 3D structures assembled by single-layered MoS_2. The EDX elemental maps (insets in (e)) clearly show that sulfur and molybdenum are uniformly distributed in the assembled structures. (f) TEM image of a single tube. (g) Enlarged image in (f). The arrows indicate the separated layers with thickness below 0.7 nm.

Reproduced with permission from Ref. [219]. Copyright 2014, John Wiley & Sons, Inc.

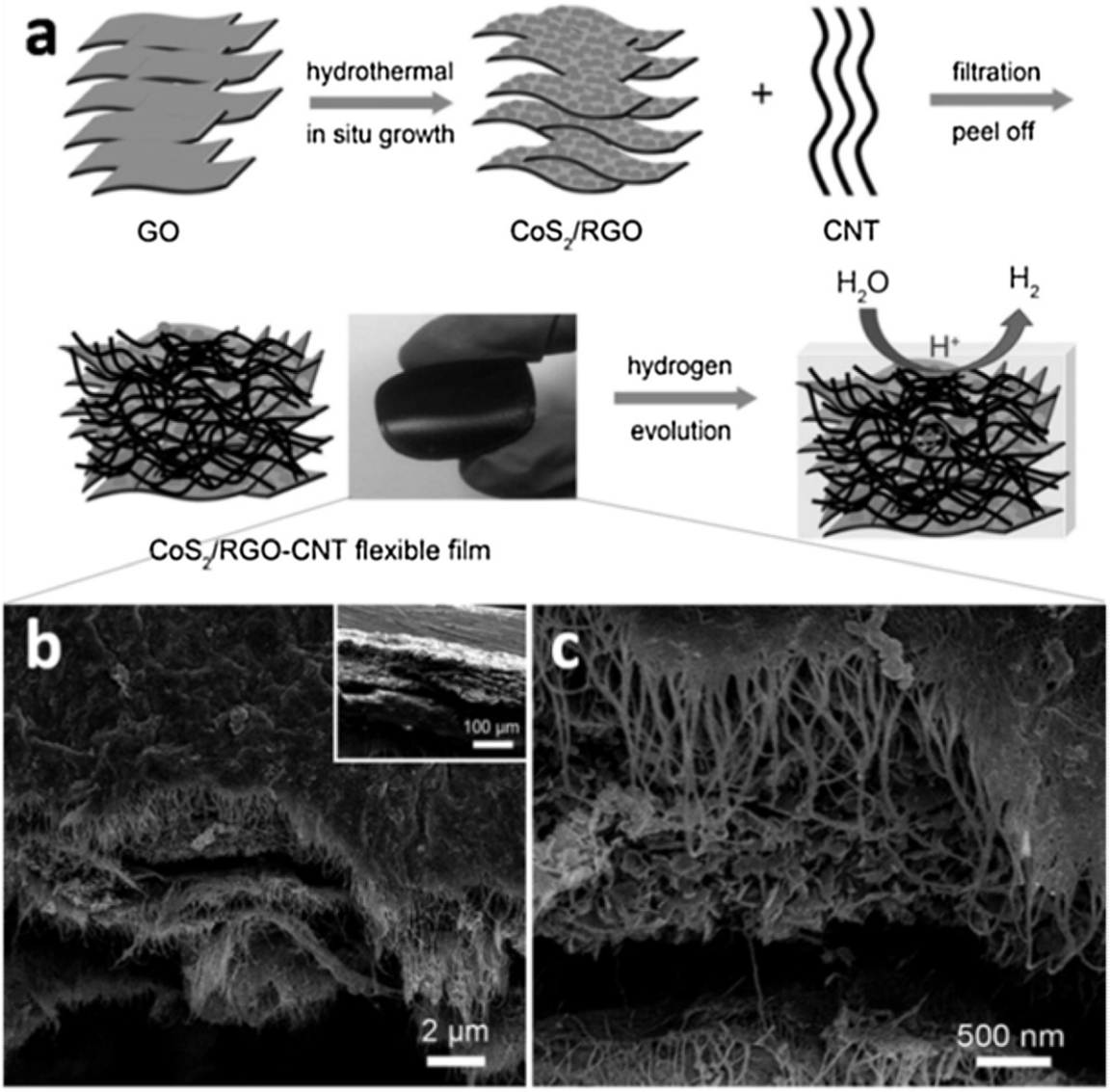

Fig. 11. (a) Fabrication procedure and hydrogen evolution process of the freestanding CoS_2/RGO-CNT hybrid electrode. (b) Cross-sectional and (c) corresponding magnified SEM.

Reproduced with permission from Ref. [231]. Copyright 2014, John Wiley & Sons, Inc.

interest due to their potential applications in roll-up displays, wearable electronics and other devices. The design and preparation of a robust and flexible electrode based on cobalt sulfide/reduced graphene oxide/carbon nanotube (CoS_2/RGO-CNT) nanocomposites are discussed [231]. An efficient hydrothermal and vacuum filtration combined process was utilized to prepare such composite architecture, which was subsequently embedded into a porous CNT network. The CoS_2 nanosheets were first in situ grown on the surface of RGO substrates conductive and porous properties are beneficial for electronic and ionic transport. Moreover, the process is facile by using CNT and CoS_2/RGO as raw materials without any polymer binder in the film, which possessed porous structures, high mechanical strength, and superior flexibility (Fig. 11). Kang et al. reported the design and synthesis of 3D flower-like MoS_2 hierarchical structures, on reduced graphene oxide/oxidized multiwalled carbon nanotube backbone, through one-pot hydrothermal method [232]. Chen et al. recently presented the production of 2D polyethyl eneglycol (PEG)-modifed MoS_2 nanosheets by solvothermal treatment of $(NH_4)_2MoS_4$ and PEG-400 aqueous solution [233]. Furthermore, they designed and prepared MoS_2/Bi_2S_3-PEG composite nanosheets, due to the reaction with two extra S atoms and Bi atoms during the solvothermal treatment [234]. A part of the utilized PEG-400 chains could be branched on the MoS_2/Bi_2S_3-PEG nanosheet surface, which enables the excellent biocompatibility and colloidal stability of the nanosheets. More importantly, a sensitive computed tomography (CT) imaging capacity and radiation enhancement effect could be obtained by the integration of Bi, whereas the MoS_2 framework enables the MoS_2/Bi_2S_3-PEG nanosheets with an excellent photothermal transformation capacity and photoacoustic (PA) imaging [235]. Therefore, such a MoS_2/Bi_2S_3-PEG composite nanosystem was realized both in vitro and in vivo CT and PA imaging-guided combined tumor PTT and sensitized RT. In addition, 3D hierarchical MoS_2/polyaniline (PANI) nanoflowers were fabricated via a simple hydrothermal method by Xu et al. [236]. And then, the prepared MoS_2/polyaniline (PANI) nanoflowers were annealed in a N_2 atmosphere at 500 °C for 4 h, 3D hierarchical MoS_2/C nanoflowers were further obtained.

In addition, CNTs, carbon fibers/tubes and other inorganic oxide fibers have also been widely used as templates or matrices for growth of or hybridization with transition metal dichalco-

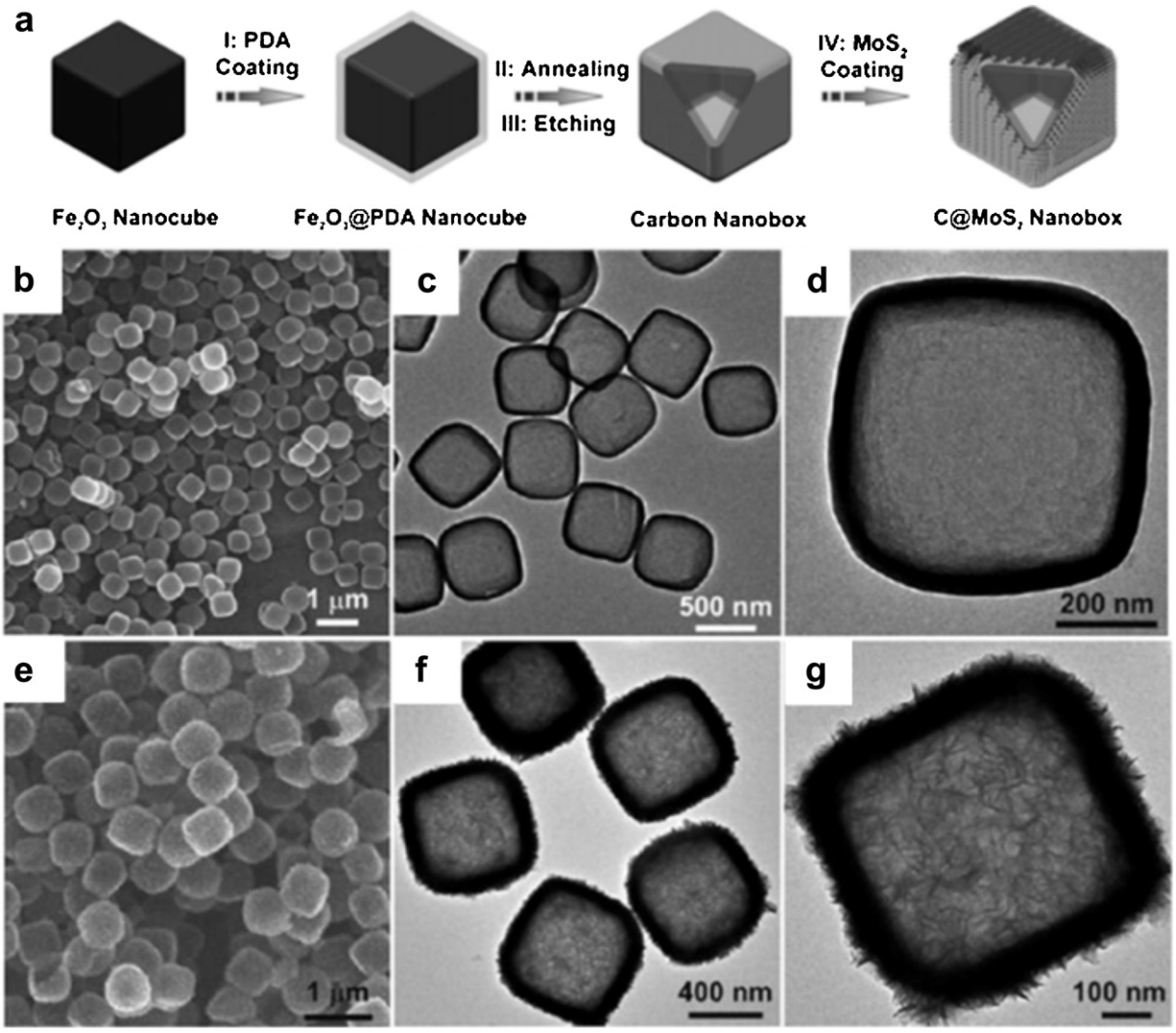

Fig. 12. (a) Illustration of the synthesis process of C@MoS_2 nanoboxes. FESEM (b) and TEM (c,d) images of carbon nanoboxes, and FESEM (e) and TEM (f, g) images of C@MoS_2 nanoboxes.

Reproduced with permission from Ref. [245]. Copyright 2015, John Wiley & Sons, Inc.

genides nanosheets by hydrothermal reaction. For instance, our group demonstrated the in-situ self-assembly of few-layer MoS_2 nanosheets on a CNT backbone via the hydrothermal reaction with a subsequent annealing process [237]. The few-layer MoS_2 nanosheets with controllable contents were alternately and vertically grown on the surface of CNTs, forming 3D hierarchical nanostructure. Zhang et al. showed a facile and efficient method to fabricate a flexible, 3D, binder-free electrode architecture consisting of highly conductive carbon nanotube paper conformally covered by MoS_2 nanosheets [238]. Moreover, the few-layered MoS_2 nanosheet-coated, electrospun SnO_2 nanotube heterostructures with 3D configurations were fabricated by a simple template sintering combined with a one-step solvothermal approach [61]. Morphological characterization showed that SnO_2 nanotubes were uniformly covered by sheet-like MoS_2 subunits on both the outer and inner surfaces. Yu et al. developed a simple strategy to synthesize well-defined CNFs@MoS_2 coaxial nanofibers [239]. A double-coating stratagem was utilized to synthesize CNFs@MoS_2 where uniform hydrothermal carbonaceous nanofibers with diameter of c.a. 80 nm were used as supports, which enables the solution-based growth of MoS_2 nanosheets [240]. The precursor was then annealed by carbonization of the core and crystallization of the sheath under nitrogen atmosphere. And these synergistic effect nanostructures can help to build a hierarchically conductive network, contributing to much improved electrode kinetics and cycling stability for lithium-ion batteries. The strategy for the first design and synthesis of a cubic cobalt sulfide–layered molybdenum disulfide core–shell/carbon nanofibers (Co_9S_8@MoS_2/CNFs) hybrid system was obtained through a simple S vapor assisted graphitization of polyacrylonitrile (PAN) nanofibers containing cobalt nitrate and ammonium tetrathiomolybdate [241]. The Co_9S_8@MoS_2 core-shell nanostructure consists of a shell of fullerene-like MoS_2 layers and a core of Co_9S_8 nanoparticle. The CNFs serve as a substrate for the anchor of Co_9S_8@MoS_2 as well as used as hosts and reactors for the inoculation of Co_9S_8@MoS_2. A 3D flexible carbon fiber foam with MoS_2 nanoparticles was obtained by the solvothermal reaction of $(NH_4)_2MoS_4$ and hydrazine immersed with bacteria-cellulose derived carbon fiber foam [242]. Firstly, the bacteria-cellulose hydrogel was freeze-dried to remove the water while maintaining its porous nanostructure. Subsequently, the carbon fiber foam hydrogel was fabricated by directly pyrolyzing the freeze-dried bacteria-cellulose hydrogel under the inert atmosphere. The MoS_2 was in situ decorated into the carbon fiber foam framework by the one-step solvothermal method. 3D hierarchical MoS_2 nanoflake array/carbon cloth was synthesized by one-step hydrothermal method, in which the spacing of the (002)

crystal plane was significantly expanded [243]. Cui et al. developed nanostructured MoS_2 particles with preferentially exposed edge sites on the 3D carbon fiber paper substrate by the facile pyrolysis and sulfurization methods [244]. By Li electrochemical intercalation and layer exfoliation, the electronic structures of MoS_2 can tune from 2H to 1T phase. MoO_3nanoparticles were synthesized on a carbon fiber paper substrate, carbon fiber paper was first treated by O_2 plasma to make it hydrophilic and then dipped into the ammonium heptamolybdate solution and dried on a hot plate with the salt uniformly distributed on the substrate. The substrate was then heated up to 600 °C under Ar atmosphere in a tube furnace, where the ammonium heptamolybdate decomposed to produce MoO_3nanoparticles. The as-grown MoO_3 nanoparticles were then put into a tube furnace for rapid sulfurization and converted into MoS_2 nanoparticles. Importantly, PVP can help to disperse the salt on the carbon fibers and was coated on the surface of the nucleated nanoparticles during the pyrolysis process to prevent them from further aggregation. Moreover, there is also widespread concern that the novel morphology core-shell nanostructures of transition metal dichalcogenides-based hybrid materials. For instance, Lou and his coworkers developed the rational design and synthesis of a novel nanosheets-on-box nanostructure composed of ultrathin MoS_2 nanosheets on N-doped carbon nanoboxes designated as C@MoS_2 nanoboxes (Fig. 12) [245].

Very uniform α-Fe_2O_3 nanocubes with an average size of about 500 nm synthesized by a facile coprecipitation method [246] are used as templates to synthesize N-doped carbon nanoboxes. In the first step, Fe_2O_3 nanocubes are uniformly coated with a smooth layer of polydopamine (PDA) with c.a. 40 nm in thickness. Then, these core-shell Fe_2O_3@PDA nanocubes are transformed into Fe_3O_4@C nanocubes after carbonization in N_2 [247]. The carbon nanoboxes could be obtained by easily dissolved the Fe_3O_4 core in HCl. Lastly, a layer of ultrathin MoS_2 nanosheets was grown on the surface of carbon nanoboxes via a facile solvothermal method, leading to the formation of C@MoS_2 nanoboxes. So these well-defined C@MoS_2 nanoboxes performed enhanced electrocatalytic properties and lithium storage due to their unique structure. Specifically, the hollow structure of carbon nanoboxes and ultrathin building blocks could effectively alleviate the strain caused by the large volume change during cycling since the N-doped carbon nanoboxes substrate has relatively high conductivity. The ultrathin MoS_2 nanosheets dominate a high surface area for electrode/electrolyte interface such that the diffusion length of electrons and ions could be efficiently reduced. In addition, 3D graphene-like MoS_2 hierarchical nanoarchitectures with embedded amorphous carbon layers were prepared via a hydrothermal route [248]. Due to the introduced amorphous carbon into the layer structure of the MoS_2 nanosheets, the interlayer distance of MoS_2 (002) increased 0.62–1.38 nm. 3D MoS_2-CdS-γ-TaON hollow composites were synthesized by anchoring MoS_2-CdS nanocrystals on the surfaces of γ-TaON hollow spheres via a two-step ion-exchange route with assistance from a hydrothermal process [249]. The activity of the prepared composites heterojunction in H_2 evolution can be dramatically improved when a small amount of MoS_2 is introduced into the hybrid cocatalyst. It is believed that the matched energy band of 3D MoS_2-CdS-γ-TaON hollow composites heterostructures favors the charge transfer and suppresses the photoelectronhole recombination, and the unique features of MoS_2 make it a substitute for noble metals, leading to the enhanced photocatalytic hydrogen production.

Others 2D nanosheets-based 3D architectures

The typical 2D semiconductors MoS_2, $MoSe_2$, WS_2, and WSe_2 have garnered tremendous interest for their unique electronic, optical, and chemical properties [250]. Such extreme thinning indeed results in substantial changes in their electronic structures and thus in new optoelectronic properties and applications in devices [251]. Up to now, over hundreds of 2D materials have been found, including group-IV compounds (e.g. graphene, silicene and germanene), binary systems of group III–V elements (such as BN), metal chalcogenides, complex oxides, and so on [252]. Recently, black phosphorus nanosheets were also successfully fabricated [253]. Zhang et al. reported a facile solution-based method for the preparation of black phosphorus quantum dots from the bulk black phosphorus, which were an average size of 4.9 ± 1.6 nm and thickness of 1.9 ± 0.9 nm (about 4 ± 2 layers) [184]. Zeng and his group [254] identified two novel 2D wide-band-gap, high stable semiconductors, namely antimonene (Sb monolayer) and arsenene (As monolayer), by using density functional theory (DFT) calculations. However, these novel materials still could not be synthesized in the laboratory. Furthermore, in the family of newly developed 2D nanostructured materials, 2D soft nanomaterials, including $B_xC_yN_z$ nanosheets (such as graphene, *h*-BN, BCN_2, BC_2N, *g*-C_3N_4), 2D supramolecular organic nanostructures, covalent organic frameworks (COFs) and 2D polymers, have great advantages in light-weight, structural control and diversity, flexibility of preparation approaches, and so on [255]. So in this part, we discuss these novel 2D materials to build 3D architectures.

C_3N_4-based 3D architectures

Graphene with C atoms substituted by B and N atoms exhibits p-type and n-type semiconducting electronic properties [256,257]. Graphitic carbon nitride, generally known as *g*-C_3N_4, is recognized as the most stable allotrope among various carbon nitrides under ambient conditions. *g*-C_3N_4-based photocatalysis has become a very hot research topic since the pioneering work in 2009 on *g*-C_3N_4 for visible-light photocatalytic water splitting [258]. *g*-C_3N_4 could be synthesized via the thermal polymerization of the nitrogen-rich precursors such as dicyandiamide, cyanamide, thiourea, urea, melamine and so on [259–264]. And as a polymer, *g*-C_3N_4 possesses the flexible structure, which could be suited to form different morphologies with the different templates. And several typical nanostructures of *g*-C_3N_4 have been obtained. Hard and soft templating methods are often used because they allow tuning of the porous structure of *g*-C_3N_4 by choosing different templates. Mesoporous *g*-C_3N_4 has been successfully obtained by using various precursors in the presence of silica nanoparticles used as a hard template, the removal of which generated a 3D interconnected structure of *g*-C_3N_4 with a large surface area [265,266]. Moreover, the seaweed-like *g*-C_3N_4 architecture has been prepared by direct calcination of the freeze-drying-assembled, hydrothermally treated dicyandiamide fiber network [267]. Dicyandiamide was used as the starting material undergoing the hydrothermal treatment and vacuum freeze-drying technology was exploited to activate the self-assembly for the formation of the macroscopic network of fiber-like structures. Subsequently, the calcination of the precursor generated the network architectures of *g*-C_3N_4 "seaweed" which is rich in mesopores. Yang et al. prepared the macroscopic 3D porous *g*-C_3N_4 monolith via the one-step template method, which was calcined the urea inside the framework of melamine sponge template without any other crosslinking or functionalizing agents [268]. The general preparation route leading to the macroscopic 3D porous *g*-C_3N_4 monolith is displayed in Fig. 13. The commercial melamine sponge was used as the template and supporting framework without any treatments. After dipping and freeze-drying, the melamine sponge with urea was completely. Heating the melamine sponge with urea at 550 °C for 4 h resulted in a macroscopic 3D PCNM. The resultant PCNM could be easily cut into different shapes with a blade. In addition, the 3D

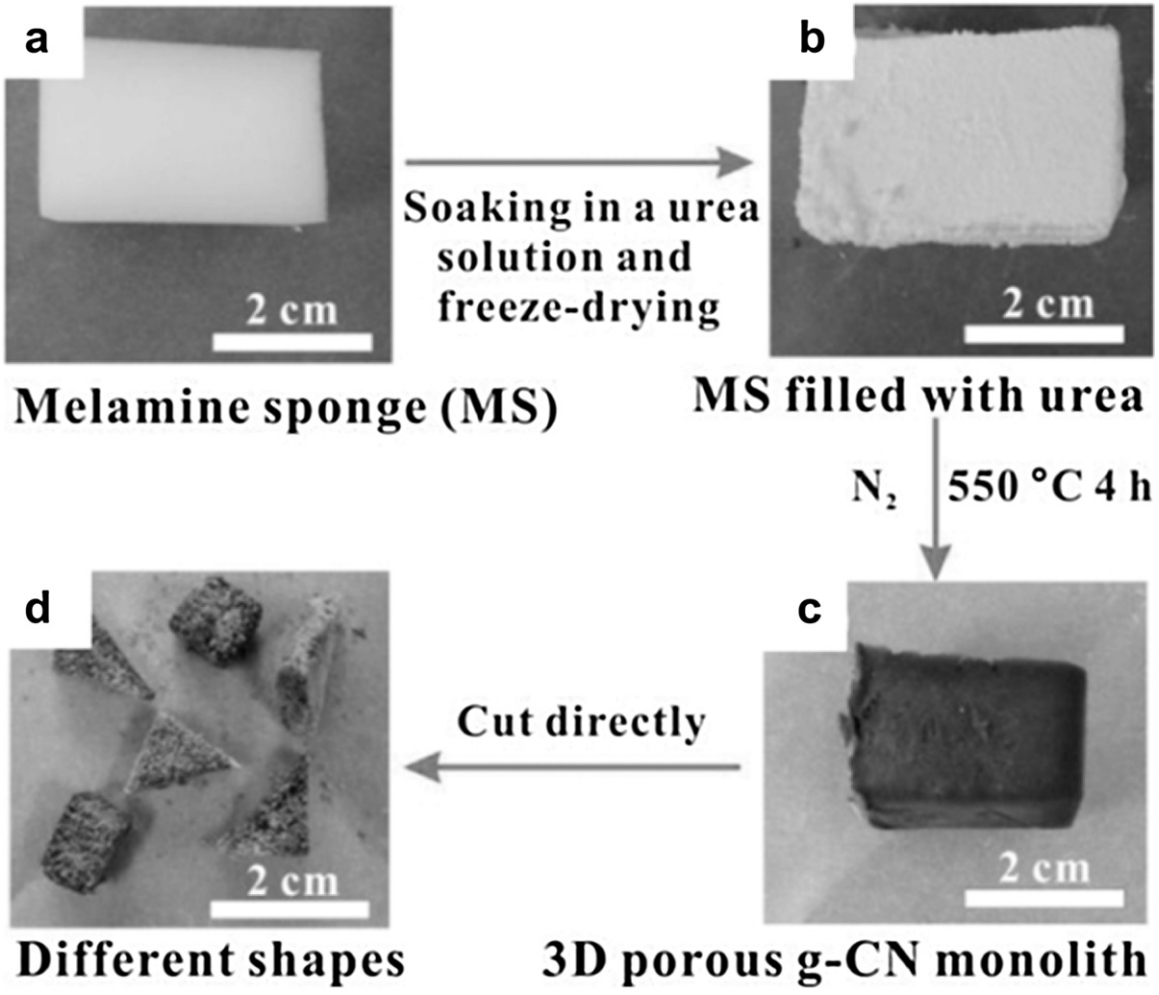

Fig. 13. Illustration of the preparation of a macroscopic 3D PCNM.
Reproduced with permission from Ref. [268]. Copyright 2015, John Wiley & Sons, Inc.

ordered mesoporous g-C_3N_4 with *Fm3m* mesostructures was prepared by carbon tetrachloride and ethylenediamine as precursors and FDU-12 as a hard template [269]. Stucky et al. presented the method to prepare 3D macroscopic assemblies of low-dimensional g-C_3N_4, such as nanoparticles, nanotubes, and nanosheets [270]. Due to the hydrogen-bonded molecular assembly between triazine molecules, the g-C_3N_4 could be tailored to demonstrate preferential growth by changing the crystallization solvent, system temperature, and hydrogen bonding donor–acceptor pair, and characterize their cooperative properties, which could allow the design and synthesis of various nanostructure g-C_3N_4 and their nanocomposites with specified dimension and chemical functionality.

As is well known graphene can be used as a versatile building block for self-assembling into specific architectures, which is essential for converting the remarkable microscopic characteristics of graphene sheets into macroscopic properties of practical significance [271,272]. It was found that the combination of g-C_3N_4 with graphene could improve the conductivity and electrochemical performance of g-C_3N_4 [273]. Qiao et al. [274] developed the preparation of a flexible 3D film by integrating porous g-C_3N_4 nanolayers with nitrogen-doped graphene sheets via a simple vacuum filtration method. This 3D N-graphene-C_3N_4 hybrid material has the structure comparable to previously reported van der Waals heterostructures, but with the 3D macroscopic architecture (Fig. 14a). As compared to its 2D counterpart, this 3D heterostructure has many intriguing properties for favored catalysis, such as highly exposed catalytic centers, hierarchical pores, and strong mechanical flexibility. Furthermore, 3D g-C_3N_4-graphene foam or aerogels were also prepared by the hydrothermal process [275]. Ajayan et al. developed an efficient approach to large-scale production of Pt-decorated 3D architectures built from graphene and g-C_3N_4 nanosheets, which can not only provide the through multi-level channels for the fast reactants transportation to the electrochemically active positions, but are also conducive to keeping the high conductivity of overall catalysts [276]. In Fig. 14b, monolayer graphene oxide sheets were prepared from natural flake graphite according to a modified Hummers method, and few-layer g-C_3N_4 nanosheets were produced by liquid phase exfoliation of bulk g-C_3N_4 by the ultrasonic treatment. Afterward, these two kinds of nanosheets were mixed together by the sonication to form the homogeneous suspension. Then the prepared suspension was sealed in an autoclave and hydrothermal maintained at 180 °C for 12 h. During hydrothermal process, the functional groups of graphene oxide such as carboxyl and hydroxyl groups interconnected to support the 3D architectures, similar to the graphene oxide hydrogels, while the g-C_3N_4 nanosheets were confined in the pores or interspaces between the graphene oxide layers. Furthermore, the resulting samples were critical point dried in CO_2 to maintain the 3D porous structure. Finally, Pt nanoparticles were progressively grown on the surfaces of graphene and g-C_3N_4 nanosheets of the as-prepared 3D architectures in ethylene glycol solution, generating 3D Pt/G-CN hybrids. Qu et al. further

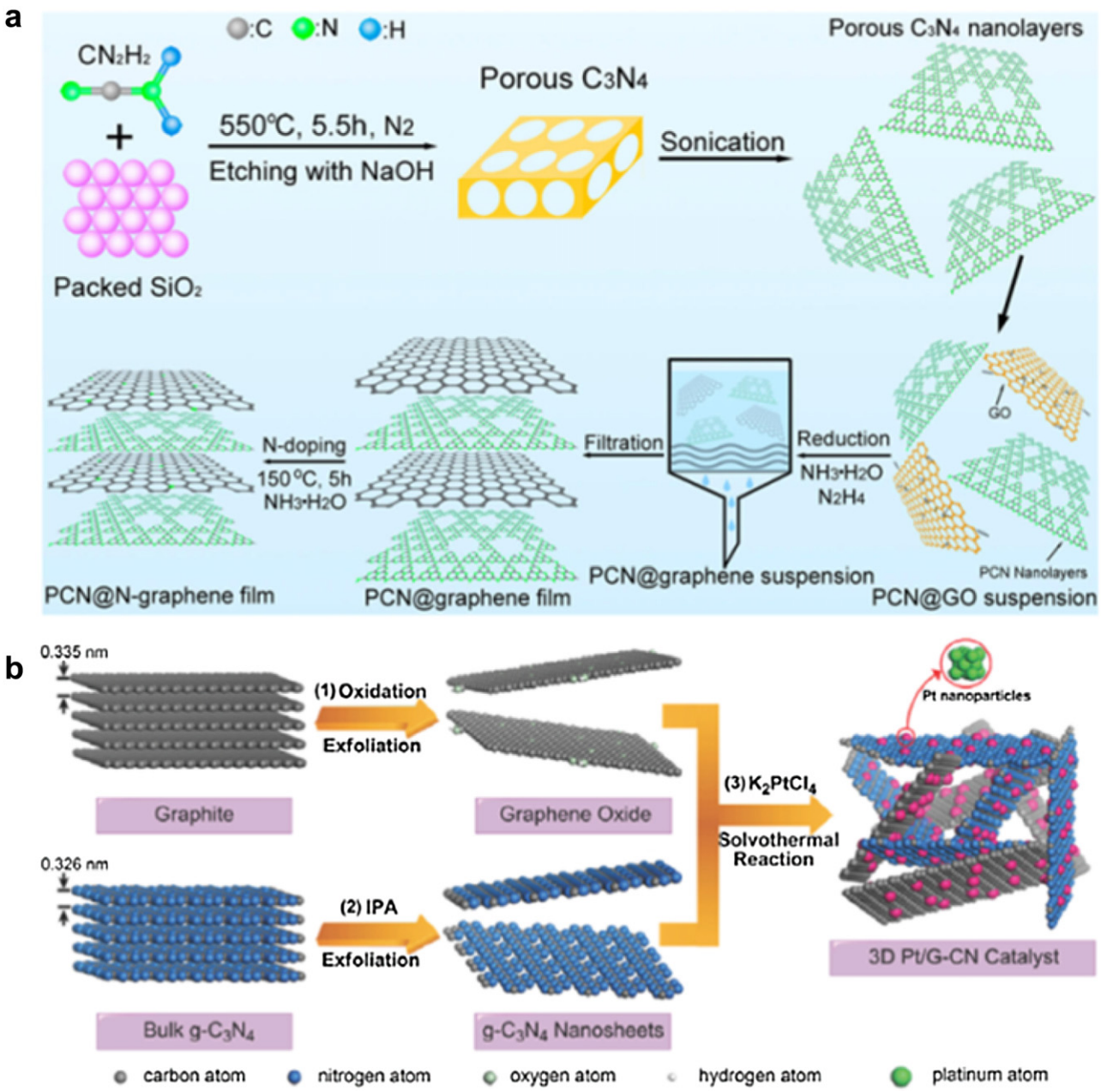

Fig. 14. (a) Schematic illustration of the preparation process of PCN@N-graphene film. Reproduced with permission from Ref. [274]. Copyright 2015, American Chemical Society. (b) Schematic illustration of the synthesis process of the 3D Pt/G-CN catalyst, (1) the fabrication of graphene oxide from graphite by the Hummers method, (2) the liquid-exfoliation of bulk g-C_3N_4 into g-C_3N_4 nanosheets by the ultrasonic treatment, (3) formation of 3D porous G-CN architectures by solvothermal treatment and controllable growth of Pt nanoparticles on the surfaces of graphene and g-C_3N_4. Reproduced with permission from Ref. [276]. Copyright 2014, John Wiley & Sons, Inc.

achieved the assembly of 1D in situ formed g-C_3N_4 nanoribbons on 2D graphene sheets to form 3D interconnected networks (g-C_3N_4 nanoribbon-G) by the one-step hydrothermal treatment [277]. Such 3D hierarchical architecture of g-C_3N_4 nanoribbon-G provided the large open surface area, multi-electron transport channel and short diffusion distance for the remarkable charge separation and transfer, that effectively improves their electrochemical properties. Meantime, 3D porous supramolecular architecture of ultrathin g-C_3N_4 nanosheets and rGO was constructed via solution self-assembly of g-C_3N_4 and GO [278]. The resulting 3D hybrid possessed multilevel porous structure, high surface area, efficient electron transport network, excellent electron conductivity, and a fast charge transfer kinetics at g-C_3N_4/rGO interfaces. Of course, in addition to the g-C_3N_4 and graphene nanohybrid materials, there are other g-C_3N_4-based architectures with other carbon materials, such as CNTs [279] and C-Dots [280]. Qiao et al. reported 3D g-C_3N_4 nanosheets and CNT porous composites through the self-assembly by π-π stacking and electrostatic interactions [279]. The utilization of g-C_3N_4 nanosheets as the precursor instead of bulk g-C_3N_4 facilitates the robust assembly to form 3D interconnected network. 2D g-C_3N_4 nanosheets were first prepared by sonication/exfoliation of protonated g-C_3N_4. The spontaneous assembly between the mildly oxidized CNTs (zeta potential of −19.3 mV) and the positively charged g-C_3N_4 nanosheets (zeta potential of +25.6 mV) was then achieved by the hydrothermal method driven by theπ-π stacking and electrostatic interactions to build the porous 3D nanocomposites. Kang et al. then reported the design and preparation of the metal-free carbon nanodot-C_3N_4 nanocomposites and demonstrated their distinct performances for photocatalytic solar water splitting [280]. And then, our group also demonstrated the novel

carbon–nitrogen quantum dots by the hydrothermal method using melamine and glutaraldehyde, which exhibited catalytic activity for the oxygen reduction reaction [281].

'White graphene'-based 3D architectures

Hexagonal boron nitride (*h*-BN) is similar to graphite, the monolayer *h*-BN, which is a structural analogue of graphene, has been defined to 'white graphene' [251]. *h*-BN is comprised of alternating B and N atoms replacing carbon in a honeycomb arrangement. Like to graphite, there are strong covalent bonds within the plane and weak bonds with van der Waals forces between different planes due to the sp2-bonded in *h*-BN. At present, there are many methods to design and preparation of high-quality BN nanosheets, such as chemical exfoliation, mechanical exfoliation, chemical vapor deposition, unzipping BN nanotubes, and thermal decomposition [251]. Similar to graphene, BN nanosheets are also built the 3D architectures.

3D white graphene foams with hierarchical pores were prepared by a vesicant-assisted gas-foaming approach [282]. As shown in Fig. 15, the foaming process and formation of 3D BN white graphene foams is illustrated. First, ammonia borane was used as the raw material, which can be transformed into a B–N–H polymeric liquid derivate at temperatures as low as 100–200 °C [283]. The mass of ammonia borane decreased about 55% under 200 °C due to the release of hydrogen, which leaved behind the polymer-like aminoborane and polyiminoborane [283]. And then, the thiourea and aminothiourea were selected as the vesicants. Additionally, the adequate gas release from these vesicants compensated for the inadequate decomposition of the NH_3BH_3 precursor and thus ensured the large void volume in the intermediate product. With further increase in temperature, the void-impregnated intermediates tended to crystallize *in-situ*. And then, they were progressively transformed into 3D white graphene foams with the large pores and thinness *h*-BN walls. And the more likely, the method of building the structural parts of 3D foams was revealed using hybrid 2D atomic layers made of stacked graphene oxide nanosheets reinforced with *h*-BN discs [284]. The presence *h*-BN domain avoided the graphene oxide nanosheets from crumbling and binded them to form the large discs. These restacking discs constituted the distinct ordered 3D structures. The mechanical and thermal stabilities were obviously promoted compared to the disorderly open porous networks of graphene oxide foams without the *h*-BN. And these novel structural were further corroborated by the molecular dynamics simulation to explain the improved mechanical properties. The as-prepared foam by the simple wet chemistry and lyophilization can also obtain the morphology of the container, which could allow large-scale and low cost synthesis of these 3D structures. Teo et al. further demonstrated the controllable complex of 3D carbon and 3D *h*-BN into a completely 3D-BNC network with different C:BN component prepared by the chemical vapor deposition using Ni foams as the template [285]. Due to the difference in growth rate of BN and C, these 3D-BNC could be prepared by a two-step method under the low pressure in order to attain well controllability of C:BN composition. During the growth process, BN was utilized by the sublimating borazane under 120 °C, and then, ethanol was bubbled into the system. The Ni foams were represented as the 3D porous blocks, which can build up the 3D structures by the stacked sheets in the porous Ni. The stochastic blocks of *h*-BN layers were displayed as the neighbouring BN domains combine together. The BN growth was quenched rashly before the continuous layer of BN was constituted throughout the Ni foams, which lead to the partial coverage of 3D-BN. The method process of acquiring fractional coverage 3D-BN patch was similar to the 2D counterpart, and the various controlled growth parameters had already been well studied [174,286]. For instance, BN growth needed ca. 1 h to cover the Ni foam completely. After the terminated BN growth, carbon source was introduced into the quartz tube for carbon growth. Graphene nucleated and grown over the surface of Ni regions continuously and attaching or overlapping with the existing BN, forming hybridized BNC layers which cover the overall Ni template. The similar synthesis of patched and stacked graphene and *h*-BN 2D structure had also been reported recently [287]. Furthermore, BN nanostructure materials as the supports loaded noble metal nanoparticles as the new and efficient catalyst materials [288].

Transition-metal oxides and hydroxides

Properly speaking, materials with few-layered atomic planes and 2D scalability should be named '2D crystals', which can also be intuitively defined as 'ultrathin nanosheets'. Besides the above well known 2D materials, some metal oxide and oxyhydroxide also have this nanostructure. Their electronic and magnetic performances are highly sensitive to the dimensionality of the materials [289,290], which supplies the routes to control these ground states by confining the thickness to a few atomic layers. But the traditional exfoliation approach is very difficult to achieve atomically thintransition-metal oxides nanosheets, due to the hard and inefficient cleavage of the strong inherent chemical bonding. Very recently, 1.5 nm thickness Co_3O_4 nanosheets have been prepared after the initial liquid exfoliation of $Co(OH)_2$ [291]. Monoclinic VO_2 nanosheets with a thickness of ca. 3.0 nm have also been synthesized via a structural phase transition-assisted liquid exfoliation strategy, and they exhibited half-metallic character and a thermally induced phase transition [292]. Compared to the top-down methods, the bottom-up approach of epitaxial growth had been evidenced to be an effective way to grow the thinner layered materials [293,294]. So the atomically thin layer of transition-metal hydroxide, which has very weak hydrogen bonding between the adjacent layers [295,296], can be orientedly grown at first, the corresponding transition-metal oxides ultrathin nanosheets could be easily obtained via the subsequent process of topochemical transformation. Halfunit-cell nanosheets of α-Fe_2O_3 were synthesized by a "template-assisted oriented growth" strategy [297]. Even isolated single-atom Rh dopants in 2D titanium oxide crystals were prepared by $Cs_{0.7}Ti_{1.82-x}Rh_xO_4$ converted into the protonated form by acid-exchange processing in HCl solution [298]. Exfoliation of the layered titanium oxide to single nanosheets has a lepidocrocite-like structure with a thickness of 0.7 nm, and some quantity of defects exist at the Ti sites. Xie et al. report the successful synthesis of clean fiveatomic-layer-thick SnO_2 sheets by the chemical reaction between $SnCl_2{\cdot}2H_2O$ and ethylenediamine [299]. Our group also prepared ultrathin MnO_2 nanosheets [300–303]. Beside these metal oxides, the other compounds have the similar nanostructures, such as metal hydroxide [304–306], layered double hydroxide [307–309], clays [310], transition-metal phosphates [311], spinel structured nanosheets with oxygen deficiencies [312] and so on.

There are also some reports about the above-mentioned metal oxide or hydroxide to build 3D nanostructures, and our group has the in-depth researches. Three kinds of 3D hierarchical porous nanostructures assembled from ultrathin MnO_2 nanoflakes with different sizes and crystallinities were prepared by the simple and scalable approach [303]. The size, pore size distribution and crystalline nature of the ultrathin nanoflakes can be tuned easily by changing the reaction temperature. In a typical procedure, $Mn(NO_3)_2$ and triblock copolymer PEO-PPO-PEO (P123) were firstly dissolved in deionized water. Then, $KMnO_4$ as an aqueous solution was slowly added dropwise into the above mixture at different temperature (0, 25 and 100 °C). Finally, the black precipitate was collected, washed and dried. In addition, uniform $Ni(OH)_2$

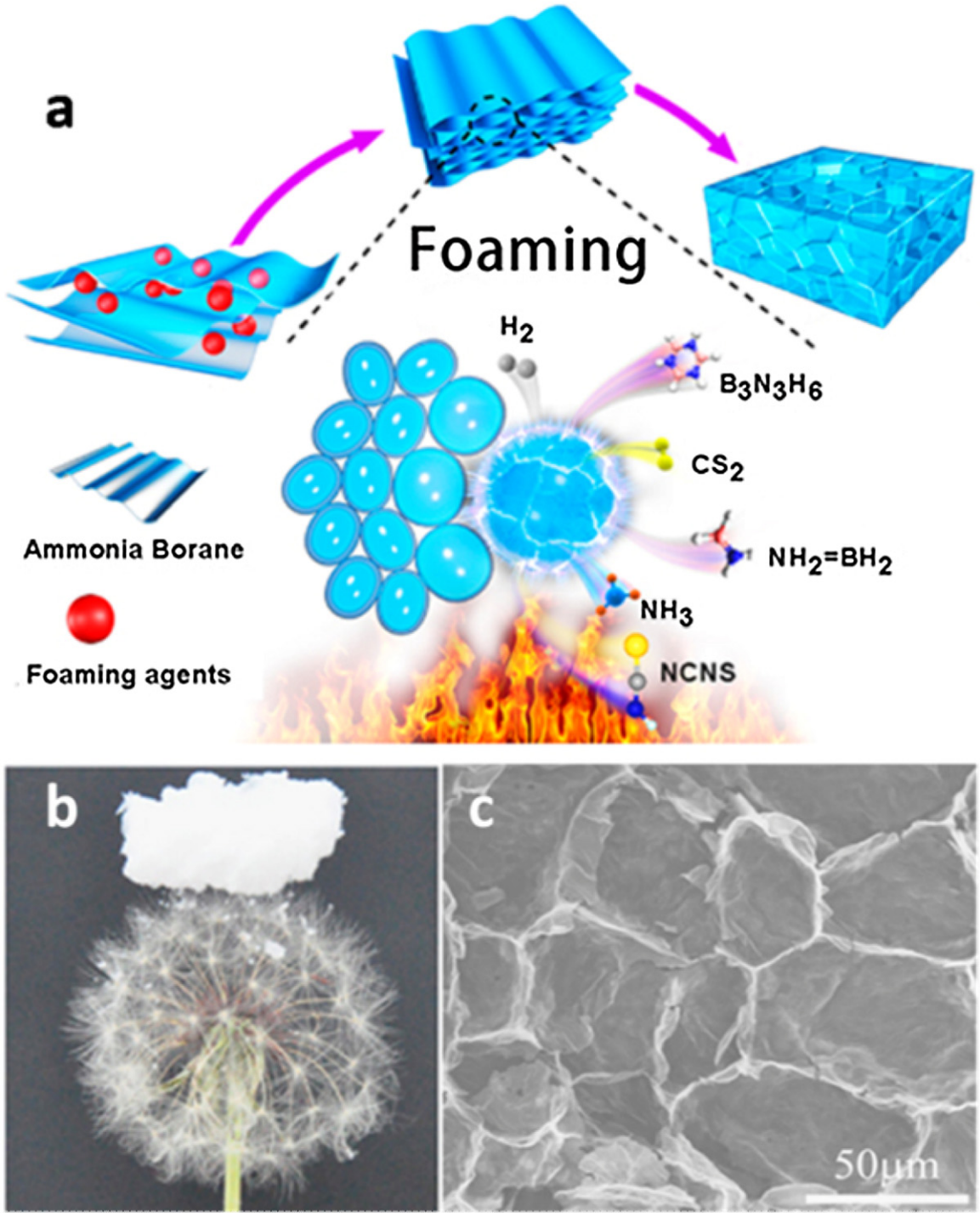

Fig. 15. (a) Illustration of 3D white graphene foams by the vesicant-assisted method. The gas released from the vesicants leads to the bubbles in the intermediate polymeric derivate and then the *h*-BN foams. (b) A piece of a WG foam standing on a dandelion. (c) SEM image of freestanding 3D WG foams, showing 20–100 μm pores. Reproduced with permission from Ref. [282]. Copyright 2015, Nature Publishing Group.

hierarchical nanostructures consisting of ultrathin nanoflakes with thickness of only about 7.4 nm were successfully synthesized via a simple HMT-assisted hydrothermal route without any catalysis or template at low temperature [305]. Gao et al. prepared the 3D honeycomb-like birnessite networks composed of ultrathin 2D nanosheets via the easy and low-cost synthetic method [313]. By using the carbon microspheres as the template instead of graphene, hierarchical birnessite structures (including york-shell and hollow) assembled by ultrathin nanosheets were received besides the ultrathin birnessite nanosheets with ca. 0.7 nm thickness. Owing to the novel structure with 3D inverse opal structure, ordered macropores, interconnected walls and regular periodicity, 3D macroporous network structures displayed greatly enhanced electrochemical performances for lithium-ion batteries. Of course, in addition to the above 2D nanomaterials, there are many kinds of other 2D nanostructure materials, such as MXenes, 2D polymers, covalent organic

frameworks (COFs), and 2D supramolecular organic nanostructures etc. MXenes, a novel family of 2D metal carbides, have demonstrated their potential as promising electrode materials for energy storage devices with volumetric capacitance exceeding all carbon materials [314–317]. Furthermore, the flexible and sandwich-like MXene/CNT composite paper electrodes were synthesized through alternating filtration of CNT and MXene dispersions [318]. The films containing onion-like carbon and reduced graphene oxide were prepared and compared with those. These sandwich-like electrodes exhibited distinguished enhanced electrochemical performances compared to those of pure MXene and stochastic mixed MXene/CNT papers. However, these 3D nanostructures with the other 2D nanomaterials are not introduced in this review, due to the greater cross-border areas and the author's limited capacity.

Applications

3D architectures are composed of 2D nanosheets, which generally possess a large surface area and macro/mesoporous structure. In addition, the composites of distinct hierarchical architecture usually provided multi-dimensional electronic networks, intend contact surface area between electrolyte and electrode, and varieties open channels for the access of the electrolyte, therefore favoring diffusion kinetics for both electrons and electrolyte solution in an electrochemical system. Even more interesting, the combination of these 2D nanosheets composite structures may generate the better performances. Thus, they inherit the excellent properties and wide range of applications of the pure 2D nanosheets. Furthermore, as the shortcomings of these 2D nanosheets have been overcome, and there are the combinations between them, at least partially, by constructing into 3D networks, the 3D hierarchical nanomaterials show more excellent performance in practical applications.

Energy storage

Because of the high conductivity of the interconnected networks, the 3D porous structure, especially the carbon-based composites, which possess the high electrochemical stability and the promise of high elasticity and mechanical stability, are considered as attractive and competent materials for application in energy storages, including both lithium-ion batteries and supercapacitors.

Lithium-ion battery

Lithium-ion battery (LIB) is one of the most attractive rechargeable batteries, which is widely used for powering electronic devices in the daily lives. Similar to the 2D nanomaterials (e.g. graphene, MoS_2, MnO), 3D architectures have been used as active electrode materials in lithium-ion batteries. To meet the ever-increasing performance demands, the search for high-performance anode materials (i.e., high capacity and desired stability) is urgent in building the next-generation LIBs. Searching the long-life active electrode materials for lithium ion batteries (LIBs) is still a great challenge because of the issue related to the volumetric expansion during lithiation. Our group demonstrated an unexpected result that a peapod-like MnO/C heterostructure with internal void space can be facilely prepared by annealing the MnO precursor (MnO-P) NW/polydopamine core/shell nanostructure in an inert gas [145]. We found that such porous heterostructure with internal void space was highly particular for high-performance LIBs, which could address all the issues related to active materials dissolution, conversion, aggregation and volumetric expansion during the Li^+ insertion/extraction. So these 3D architectures can be able to solve these problems.

As the prepared solvated graphene frameworks display distinct hierarchical solvated porous networks and can be used as electrodes with a greatly enhanced electrochemical properties compared to the unsolvated graphene frameworks, including quite high reversible capacities (1158 mAh g^{-1} and 753 mAhc m^{-3} at 0.1 A g^{-1}), outstanding rate capabilities (472 mAh g^{-1} and 307 mAh cm^{-3} at 5.0 Ag^{-1}), and excellent cycling stabilities (93% capacity retention after 500 cycles at 5.0 A g^{-1}) [100]. These performances are directly due to their higher specific surface area and faster lithium-ion diffusion as well as the increased intersheet distance arising from the unique solvated porous network of solvated graphene frameworks. The birth defects of pure 3D graphene materials are the limited theoretical capacity and poor rate performance. Our group fabricated 3D macroporous SnS_2/graphene aerogels with high reversible capacity and excellent rate capability for LIBs [229]. It can be found the combination of the high capacity active materials and 3D graphene frameworks can supply the favoring diffusion kinetics for both electrons and lithium ions by the numerous open channels and multidimensional electronic networks [93,99,105,113,157,319]. Additionally, the specific capacity and rate capability have been extremely enhanced due to the full face-to-face contact between silicon and graphene [130]. Zhou et al. used the $MnCO_3$/large-area graphene composites to offer fascinating advantages over small graphene electrodes for energy storage [99]. Because of the ordered and mutually connected configuration, the $MnCO_3$/large-area graphene composite creates uninterrupted conductive networks and effective ion transport paths, which result in compact Li storage with high-power performance. Zhi et al. prepared silicon nanoparticle-impregnated assemblies of templated carbon bridged oriented graphene by the vacuum filtration process and thermal treatment [320]. The prepared electrode was direct use as anodes with excellent lithium storage performances, which possessed outstanding volumetric capacity (1807 mAh cm^{-3}), outstanding gravimetric capacity (1390 mAh g^{-1} at 2 A g^{-1} with respect to the total electrode weight), superior rate capability (900 mAh g^{-1} at 8 A g^{-1}), competing areal capacity (as high as 4 and 6 mAh cm^{-2} at 15 and 3 mA cm^{-2}, respectively), and exceptional cyclic stability (0.025% decay per cycle over 200 cycles). Such combined level of performance can be attributed to the well designed interface interaction, nanostructure and microstructure [321]. They further synthesized graphene sheet-supported uniform ultrasmall Si quantum dots by a simple and effective self-assembly strategy [322]. And they exhibited unprecedented fast, surface controlled lithium storage behavior, rather than conventional slow, diffusion-controlled mechanisms in most battery materials.

As shown above, the well structure design, interfacial assembly and microstructure control would be effective for the fabrication of the electrode materials with outstanding performance [321]. The build of 2D nanosheets can be classified into two categories, face-to-face stacking and edge-to-edge or edge-to-face packing. Face-to-face stacking always resulted in graphite-like structures which had small interlayer spacing and high density, but due to the tightly stacked structure the ion transport was usually limited. The spatial interlinking of 2D nanosheets would provide sufficient space for ion transfer while sacrificing the density of the materials. So, increasing the interlayer spacing of the face-to-face stacked layers and decreasing the pore volume of the edge-to-edge interlinked 2D nanosheets would effectively lead to a balance between the ion transport and density, which would result in improved their performance [323–325]. In addition, another important approach was the incorporation of other components with an outstanding electrochemical capacity. The appropriate content of the high capacity materials would give rise to the synergistic effect to improve their performance [326–329]. The key issue for the incorporation of other components was the controllable interaction between 2D nanosheets and other materials, the 3D structures contributed to

the conductivity and facilitate fast ion transport while the high capacity materials were responsible for improving the overall capacity.

Molybdenum disulfide (MoS_2) displays the higher theoretical lithium storage capacity (670 mAh g^{-1}), good rate capability and outstanding cycling stability [46,220]. The weak van der Waals interaction between the MoS_2 layers can promote the reversible Li^+ intercalation and extraction without a significant volume change and also prevents the pulverization problem of active materials during the repeated lithiation and delithiation process [206,330]. However, their limited conductivity and low cycle stabilities hindered their developments. Thus, in an attempt to solve these issues, recent remarkable advances have focused on engineering novel MoS_2/C-based nanocomposites with particular design for partly improving the capacity, rate capability, and stability of LIBs by the inventing/or introducing the MoS_2/carbon interface [75,202,225,245]. Although these strategies can enhance the rate of ion and electron transport with the suppressed mechanical fracture by conductive carbon guardianship for a partly enhanced capacity and stability for LIBs, these specifically designed MoS_2-based nanocomposites have to suffer from the limited interface efficiency between carbon and MoS_2 (Fig. 16). Our group prepared 2D MoS_2/mesoporous carbon (MoS_2/m-C) hybrid nanoarchitecture with ideal MoS_2/m-C atomic interface was highly particular for improving LIBs because such architecture can supply much larger atomic interface contact/interaction between single layer MoS_2 and graphene nanosheet for LIBs than the conventional MoS_2/C nanocomposite with the limited interface contact [206]. The majorizing MoS_2/m-C hybrids can well avoid almost all the key challenges for MoS_2-based anode materials for LIBs: (a) progressing the MoS_2 electrical conductivity, particularly in the *c*-direction, (b) conquering the aggregation and restacking of the MoS_2 nanosheets, (c) tolerating the volume expansion upon lithiation, (d) alleviating the polysulfide shutting, (e) supplying the much larger interface contact for Li^+ storage. As the prepared MoS_2/m-C nanosheet architecture displays a maximum reversible specific capacity of 1183 mAh g^{-1} at 200 mA g^{-1} with outstanding rate capability (943 mAh g^{-1} at 6400 mA g^{-1}) and long cycle life (over 500 cycles), evidencing the great potential as anode electrode materials for LIBs. Under even low temperature (3 °C) and high temperature (50 °C), the prepared anode materials also demonstrate the excellent electrochemical performance in terms of rate ability, capacity and stability (Fig. 16). Four more, density functional theory (DFT) calculations indicated that the ideal MoS_2/m-C atomic interface could supply the most vigorously favored process for boosting Li^+ storage, displaying the distinct synergetic effect between MoS_2 nanosheet and single-layer carbon.

Of course, the other 2D nanosheets-based 3D architectures also have been used as electrodes for LIBs [311,313]. Due to the novel structure composed of ultrathin MnO_2 nanosheets with a 3D inverse opal structure, ordered macropores, interconnected walls and regular periodicity, these 3D macroporous networks display greatly improved electrochemical properties with outstanding cycling stability, high capacities and good rate capability as the anode materials for LIBs [313]. Yan and coworkers reported ultrathin 2D nanoflakes of transition-metal phosphates and used as the cathode for a lithium-ion battery, which exhibits excellent stability and high rate capabilities [311]. Furthermore, the as-prepared 3D architectures were also used as a 3D scaffold to accommodate sulfur for high-rate lithium-sulfur (Li-S) battery [111,140]. Wei and coworkers used a 3D sandwich-like nitrogen doped aligned CNT/graphene hierarchical architecture as cathode electrode materials for Li-S batteries, greatly improved cyclic and rate properties were demonstrated [140]. The initial reversible capacity of 1152 mAh g^{-1} can be available at 1.0 C, and keeping about 880 mAh g^{-1} after 80 cycles. Even though the high 5.0 C current density, their reversible capacity can achieve about 770 mAh g^{-1}. As the promising alternative for LIBs, sodium-ion battery is also accepting increasing attention in the past few years owing to the relative abundance of sodium compared to lithium [12]. In addition, the well designed and prepared 3D architectures are generally applicable, opening up fresh perspectives to original advanced functional composites, specifically interface-modified hierarchical 2D nanosheets for wide applications, such as lithium batteries, supercapacitors, catalysis, sensors, and hydrogen storage.

Supercapacitors

Supercapacitors have attracted intense attention owing to the high power density, fast charging and discharging, wide thermal operating range, long lifespans (>100 000 cycles), and excellent safety [90]. 3D architectures have been used as electrodes in both double-layer capacitors and pseudo-capacitors [75,143,225,331–334]. Owing to the interesting inherent properties as well as extraordinary performance, these well-designed 3D architectures nanomaterials are accepting increasing attention as the electrode materials for supercapacitors. 2D nanosheets such as graphene, due to the strong π–π interaction, these nanosheets tend to restack when they are processed into the actual electrode materials, which can extremely reduce the specific surface area and lead to inefficient utilization of the nanosheets for energy storage [75,225]. The construct of 2D nanosheets into 3D framework structures can greatly retain the unique performances of individual 2D nanosheets and has garnered violent interest for fundamental investigations and potential applications in multitudinous technologies. Herein, we also mention the recent advances in preparing 3D macrostructures and investigating them as the unique platform for supercapacitor devices. With a distinct framework structure in which the nanosheets are interlocked into 3D space to avoid the restacking, the macrostructures feature very high specific surface areas, rapid ion and electron transport, and excellent mechanical strength, which can be directly used as the electrodes for supercapacitor with rate capabilities, superior specific capacitances and cycling stabilities.

Previously, our group have reviewed mesoporous carbon incorporated metal oxide nanomaterials as supercapacitor electrodes [90,91]. In last several years, multitudinous research effort has been committed to increasing the energy density of supercapacitors without sacrificing the high power capability. For this purpose, two important problems should be solved: (1) it is critical to develop methods to prepare the high performance electrode materials for supercapacitors; (2) it is need to realize controllably assembled supercapacitor types (such as symmetric capacitors including double-layer and pseudo-capacitors, and asymmetric capacitors) [333]. The supercapacitor performance of self-supported 3D graphene networks has been studied in detail. Zhao et al. [334] reported a nitrogen-doped graphene framework with a high specific capacitance of 484 F g^{-1}, which was approaching to the theoretical EDL capacitance of 550 F g^{-1} for pure graphene. Wei and coworkers used freestanding porous graphene film with PANI nanowire arrays as electrode materials of supercapacitors [107]. The particular capacitance reached up to 385 F g^{-1} at 0.5 A g^{-1}, with a rate maintaining of 94% as current density was changed from 0.5 to 10 A g^{-1}. The excellent rate property is attributed to the interconnected porous structure in the film, which allowed electrolyte ions to pass through quickly during the charge and discharge process. Incidentally, the flexible film can be assembled into the flexible supercapacitor, which also display excellent superior supercapacitor property. Similar improved capacitances are observed in other composite 3D graphene networks. The resultant all-solid-state micro-supercapacitors, with the graphene-conducting polymer nanosheets and exfoliated

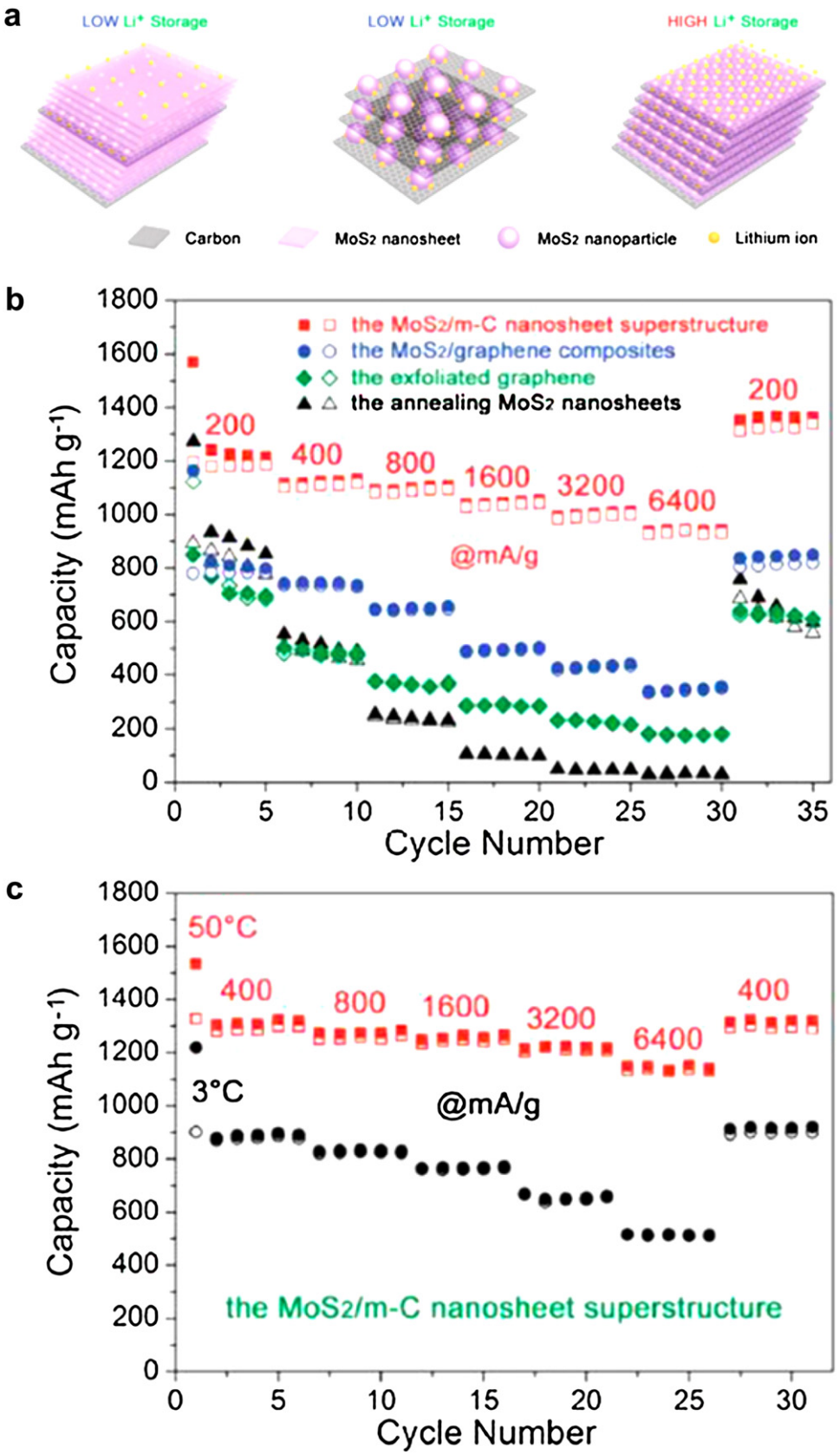

Fig. 16. (a) Illustration of Li^+ storage at MoS_2/carbon atomic interface. (b) The capacities retention of the MoS_2/m-C nanosheets, MoS_2/graphene, graphene and the annealed MoS_2 nanosheets at current densities from 200 to 6400 mA g^{-1}. (c) The capacity retention of MoS_2/m-C nanosheets at different current densities under different temperatures. Reproduced with permission from Ref. [206]. Copyright 2015, John Wiley & Sons, Inc.

graphene alternating film thickness of 5 μm, displayed an areal capacitance of 196 mF cm^{-2}, volumetric capacitance of 377 F cm^{-3}, and energy density of 10.1 mW h cm^{-3} at 10 mV s^{-1} [112]. The graphene nanosheets/acid-treated multi-walled carbon nanotube-supported poly(1,5-diaminoanthraquinone) supercapacitor in 1 M Et_4NBF_4-AN electrolyte could be reversibly cycled in a potential window of 2.8 V and displayed a high energy density of 86.4 W h kg^{-1} at a power density of 0.73 kW kg^{-1}, and maintained 55.5 W h kg^{-1} even at an ultrahigh power density of 153.9 kW kg^{-1} [127]. In addition, superior cycling stability, with 93% capacitance retention, was achieved after 10,000 cycles. The excellent property described was outstanding to that of other reported organic supercapacitors and was comparable to that of nickel-metal hydride batteries. Moreover, such a high power density surpasses the power target for the hybrid vehicles, thereby supporting its applicability for power provide components.

Among the various materials, MnO_2 has been considered as the most promising candidate owing to its environmentally friendly nature, low cost and specifically the high theoretical capacity [147,302]. However, the intrinsic poor conductivity of MnO_2 leads to an unsatisfying charge–discharge rate performance. Our group used 3D rGO/CNTs/MnO_2 nanocomposites for high-rate supercapacitors [125]. The optimized nanocomposite displayed a high particular capacitance of 319 F g^{-1} with improved rate capability (222 F g^{-1} even at 60 A g^{-1}) and cycling stability (85.4% retention of original capacity after 3000 cycles) in a 1 M Na_2SO_4 aqueous solution. In addition, direct self-assembly of 2D nanosheets and graphene was carried out for high-performance supercapacitors, such as layered double hydroxide/graphene [308] (the high capacity up to ca. 650 F g^{-1}), g-C_3N_4@Graphene [275] (264 F g^{-1}), MoS_2-rGO/MWCNT [211] etc. Tang et al. reported MoS_2/PPy as high performance supercapacitor electrodes, which displayed record high specific capacitance, remarkable rate capability and improved cycling stability, compared with all the reported conducting polymerbased electrode materials [213]. The energy density of MoS_2/PPy-2 nanocomposites received 83.3 W h kg^{-1} at a power density of 3332 W kg^{-1} and still maintained 57.5 W h kg^{-1} at a power density of 46 kW kg^{-1}. Liu et al. reported MoS_2@Ni$(OH)_2$ nanocomposites for flexible all-solid-state supercapacitors [212]. The fabricated sandwich structure all-solid-state supercapacitor with MoS_2@Ni$(OH)_2$ nanocomposites is found to have the advantages of high capacitance (14.07 mF cm^{-2} in area and 37.53 F cm^{-3} in volume), superior flexibility, high energy and power density. The resulting supercapacitors can operate at high rate up to 1000 V s^{-1}, have outstanding long-life cycling stability, remaining 94.2% of the initial capacitance after cycling for 9000 times, and mechanical flexibility during extreme bending, respectively.

Electrocatalysis

In addition, the key to advancing renewable-energy technologies is the development of electrocatalysts with high catalytic activity, low cost and remarkable stability. Noble metals, especially Pt and Pd, are well known electrocatalysts that are commercially available. To minimize the use of Pt or Pd and thereby reduce cost, they have been hybridized with the other materials. Meantime, non-precious metals or metal-free electrocatalysts with high catalytic activity are also under intensive research.

Oxygen reduction reaction (ORR)

Fuel cells have been considered as future green energy conversion devices due to potential high conversion efficiency, high power density, quiet operation, and no pollution. However, the commercial application of fuel cells is severely hindered by sluggish kinetics of oxygen reduction reaction (ORR) on cathode, which dominates the overall performance of a fuel cell. The catalytic ORR is a multi-electron process with a number of elementary steps, involving different reaction intermediates. One is a direct four-electron pathway, in which O_2 is reduced directly to water without involvement of hydrogen peroxide: $O_2 + 4H^+ + 4e^- \rightarrow 2H_2O$. The other is two-step two-electron pathway in which hydrogen peroxide is formed as an intermediate: $O_2 + 2H^+ + 2e^- \rightarrow H_2O_2$; $H_2O_2 + 2H^+ + 2e^- \rightarrow 2H_2O$. The former reaction route is highly desirable for its high deliver voltage, and meanwhile the latter pathway should be avoided. In nature, the ORR process is very slow, and hence some catalysts must be used to facilitate the four electron pathway to boost the efficiency of fuel cells. To date, Pt and its alloys have long been regarded as the most efficient catalysts for the ORR, but these catalysts suffer from some problems restricting their large-scale application, e.g., high cost and rarity of materials, diffusion of fuel molecules into the electrodes and CO poisoning. Therefore, Pt-free catalysts with high ORR activity, low cost and superior stability have been actively pursued [279]. It has been demonstrated almost all carbon materials have some electro-catalytic activity toward ORR, but the pure graphene usually catalyze a 2-electron transfer oxygen reduction, producing H_2O_2 with low voltage output. In recent years, exciting results have been reported for the N-doped graphene and graphene-based catalysts for ORR with high efficiency (4e transfer) and low cost, making them attractive for the further practical applications of fuel cells [281,335,336]. Some interesting results about N-doped 3D graphene network and composite integrated electrodes are also reported with enhanced ORR performance.

For instance, Su et al. [337] prepared 3D N-doped or S-doped graphene network for ORR by hydrothermal or solvothermal methods. Remarkably, the as-fabricated 3D graphene networks with heteroatom doping showed much better ORR performances with almost 4e transfer and higher output voltage than the unmodified graphene counterpart in alkaline solutions. Boron- and nitrogen-substituted graphene nanoribbons made into 3D porous constructs displayed the highest onset and half-wave potentials among the reported metal-free catalysts for this reaction and show excellent property compared to the commercial Pt/C catalyst [101]. And first-principles calculations represented that such remarkable electrocatalytic performances originate from the plentiful edges of boron- and nitrogen-co-doped graphene nanoribbons, which extraordinary reduced the energy barriers of the rate determining steps of the ORR reaction. Our group prepared nitrogen and phosphorus dual-doped hierarchical porous carbon foams, which displayed not only superior catalytic activity for ORR in neutral, basic, and acidic media, but also much better tolerance for methanol oxidation and much higher stability than the traditional commercial Pt/C catalysts [151]. To further improve the electro-catalytic properties, we further developed the N-doped 3D graphene network by a common approach [153,154]. Meanwhile, N-doped 3D graphene network supported transition metal ions (Co and Fe) was demonstrated with more positive onset potential, higher cathodic current density and higher electron transfer number. In addition, other nanosheets-based architectures are also used as ORR catalysts and a great advance has been achieved [46,278,338]. The enhanced ORR properties are mainly from the unique 3D porous architecture. (1) The heteroatom doped graphene networks have much more and new catalytic active sites introduced by the heteroatom (e.g. N, S, P). (2) The introduction of heteroatom can change the absorption way of O_2 and accelerate the 4e ORR reaction. (3) The 3D porous structure can provide large surface area for sufficient and efficient contact with O_2 leading to high cathodic current density. (4) For the composite, the synergistic effects (e.g., better disperse of metal oxides, more absorption/reaction sites and faster electron transfer path, improved anti-toxicity, etc.) between metal oxides and 3D N-doped graphene network improve the ORR performance.

Hydrogen evolution reaction (HER)

Hydrogen is deliberated to be the promising and appealing fuel in the future world. Compared with the widely employed steam reformed hydrogen (such as the reaction of methane and water to form H_2 and CO_2), electrocatalytically produced H_2 from water splitting can be more renewable, scalable and environment-friendly. The key step in water splitting is the hydrogen evolution reaction (HER, $2H^+ + 2e^- \rightarrow H_2$), which demands the superior catalyst to reduce the over potential and thence increase the efficiency of this important electrochemical process. Until now, electrochemical water splitting still highly relies on the use of Pt noble metal as the HER catalyst, but which is among the rarest elements in the world. It maintains challenging to develop highly effective HER catalysts which rely on materials that are more plentiful at low costs. Among all the studied alternatives, transition metal dichalcogenides-based nanomaterials have been showed to be one of the most promising non-precious catalysts for HER. Two key requirements of transition metal dichalcogenides nanosheets for HER are the effectively active sites and conductivity, such as better conductivity and more active sites result in much higher catalytic activity. And the variety of approaches have been developed to engineer functional hybrid nanomaterial based transition metal dichalcogenides nanosheets, so as to optimize the conductivity and improve active sites.

For instance, the WS_2 nanosheets-decorated rGO nanocomposites possessed much higher activity for HER than the pure WS_2 nanosheets [77]. The better property is attributed to the configuration of an interconnected conducting rGO network, leading to the speedy electron transfer from the electrode to the catalyst. Another possible reason for the improved activity of the WS_2-rGO nanocomposites might arise from the stochastic orientation of WS_2 nanosheets aligned on rGO surface which can avoid the retaking of WS_2 nanosheets to some extent during the electrode fabrication process, thereby finally retaining the effectively active sites of the catalyst. The functionalization of MoS_2 nanosheets on rGO surface to form MoS_2-rGO nanocomposites has also been confirmed to be the great way to realize the extremely active catalysts for HER [79]. Qiao et al. fabricated 3D van der Waals heterostructure WS_2@P,N,O-graphene films as a HER catalyst electrode without extra binders [204]. The prepared WS_2@P,N,O-graphene film has exhibited extraordinary HER performance, with a low over potential to achieve significant hydrogen generation, a small Tafel slop, a high exchange current density, and a robust durability (Fig. 17). The great HER performance can be ascribed to the 3D hierarchical porous structure, the highly active 1T-WS_2, and the heteroatoms-doping onto the graphene sheets in the heterostructured film. The designed flexible and robust 3D CoS_2/graphene-CNT nanoarchitecture was directly used as the catalytic electrode for the HER [231], which was one of the best non-precious electrocatalysts in acidic medium. The enhanced electrocatalytic activities of HER can also be achieved by growth of transition metal dichalcogenides nanosheets on other 3D substrates, such as amorphous carbon [339], carbon fiber paper [244], SnO_2 nanotubes [61], $SrTiO_3$ single crystals [62], graphene-mediated 3D Ni networks [223], graphene frameworks [227] and carbon fiber foam [242].

We also developed the common bottom-up method to synthesize N and P dual-doped graphene with a high dopant content and well-developed porosity, which causes to the excellent catalytic activity in HER with the comparable onset over potential (0.12 V) and Tafel slope (79 mV per decade) to some of the traditional metallic catalysts (Fig. 18) [155]. *g*-C_3N_4 with a graphite-like structure has attracted considerable attention owing to its high in-plane nitrogen content, excellent chemical and thermal stability, appealing electronic structure, and environmental friendly feature. Furthermore, it was found that the combination of *g*-C_3N_4 with graphene could improve the conductivity and electrocatalytic performance of *g*-C_3N_4 for the oxygen reduction reaction (ORR) [273,278], oxygen evolution reaction [279], and HER with catalytic activity even better than metal-based electrocatalysts [267,270,274,277,340]. Although much effort has been exclusively focused on the modification of *g*-C_3N_4 with conductive materials to promote its electronic and electrocatalytic behavior, little attention is paid to assembling the *g*-C_3N_4s into specifically nanostructured architectures for highly efficient catalytic performance. Qiao et al. [340] prepared a nanocomposite consisting of *g*-C_3N_4 and graphene with the structure similar to van der Waals heterostructures, which exhibited a good HER activity as evidenced by the over potential shifted from >700 mV for individual *g*-C_3N_4 to ~250 mV for *g*-C_3N_4 (vs RHE @ 10 mA cm^{-2}). They further developed the preparation of a flexible 3D film by integrating porous C_3N_4 nanolayers with nitrogen-doped graphene sheets, which can be directly utilized as HER catalyst electrodes without substrates [274]. This nonmetal electrocatalyst has displayed an unbeatable HER performance with a very positive onset-potential close to that of commercial Pt (8 mV vs 0 mV of Pt/C, vs RHE @ 0.5 mA cm^{-2}), high exchange current density of 0.43 mA cm^{-2}, and prominent durability (seldom activity loss >5000 cycles). The outstanding HER property stems from intense synergistic effect originating from (i) extremely exposed active sites generated by introduction of in-plane pores into C_3N_4 and exfoliation of C_3N_4 into nanosheets, (ii) hierarchical porous structure of the hybrid film, and (iii) 3D conductive graphene networks. The rationally assembled 3D architecture of in situ formed 1D *g*-C_3N_4 nanoribbons with 2D graphene has been realized by using a simple one-step hydrothermal approach, which displays extremely efficient electrocatalytic ability for the HER with low over potential and highly large exchange current density, comparable to or even better compared to that of the existing metal-free and well fabricated metallic catalysts [277].

Oxygen evolution reaction (OER)

As shown in the above, *g*-C_3N_4 and their composites can be utilized as OER ($2H_2O \rightarrow O_2 + 4H^+ + 4e^-$) catalyst electrodes, which is another key step in the process of water splitting. Compared with HER, the OER process is much more challenging in that it involves the removal of a total of four electrons and four protons from two water molecules to form one oxygen molecule. The multiple bond rearrangements as well as sluggish OER kinetics severely test the OER catalysts, which should be not only fast, stable, but also capable of water oxidation at a potential minimally above the thermodynamic value [46,341]. At present, the best and usually used catalysts for the OER are Ru and/or Ir oxides, but unfortunately they contain rare and expensive metals. Thereby, searching for cost-effective alternatives which supply the availability for large-scale application and also excellent efficiency are critical to viable water electrolytic systems. 3D *g*-C_3N_4 nanosheets-CNT porous composites were reported to display the highest activity among the nonmetal OER catalysts and better property with more advantageous kinetics and intenser durability compared to noble-metal catalysts [279]. Their excellent activity could be attributed to the large numbers of active sites, related to the high N content, and the enhanced charge and mass transport abilities owing to the 3D interconnected porous framework. Further efforts would be made toward fabrication of self-supported electrodes to promote their long-term stability and toward replacement of the CNTs with other low-price carbon supports to decrease the cost. Of course, the other 2D nanomaterials are now emerging as interesting low-cost and effective catalysts for the OER, such as Co-based materials [309,312,342]. Hu et al. reported that ultrathin nanoplates of cobalt–manganese layered double hydroxide (CoMn LDH) were a highly active and stable OER catalyst [309]. And its turnover frequency (TOF) is more than 20 times higher compared to the TOFs

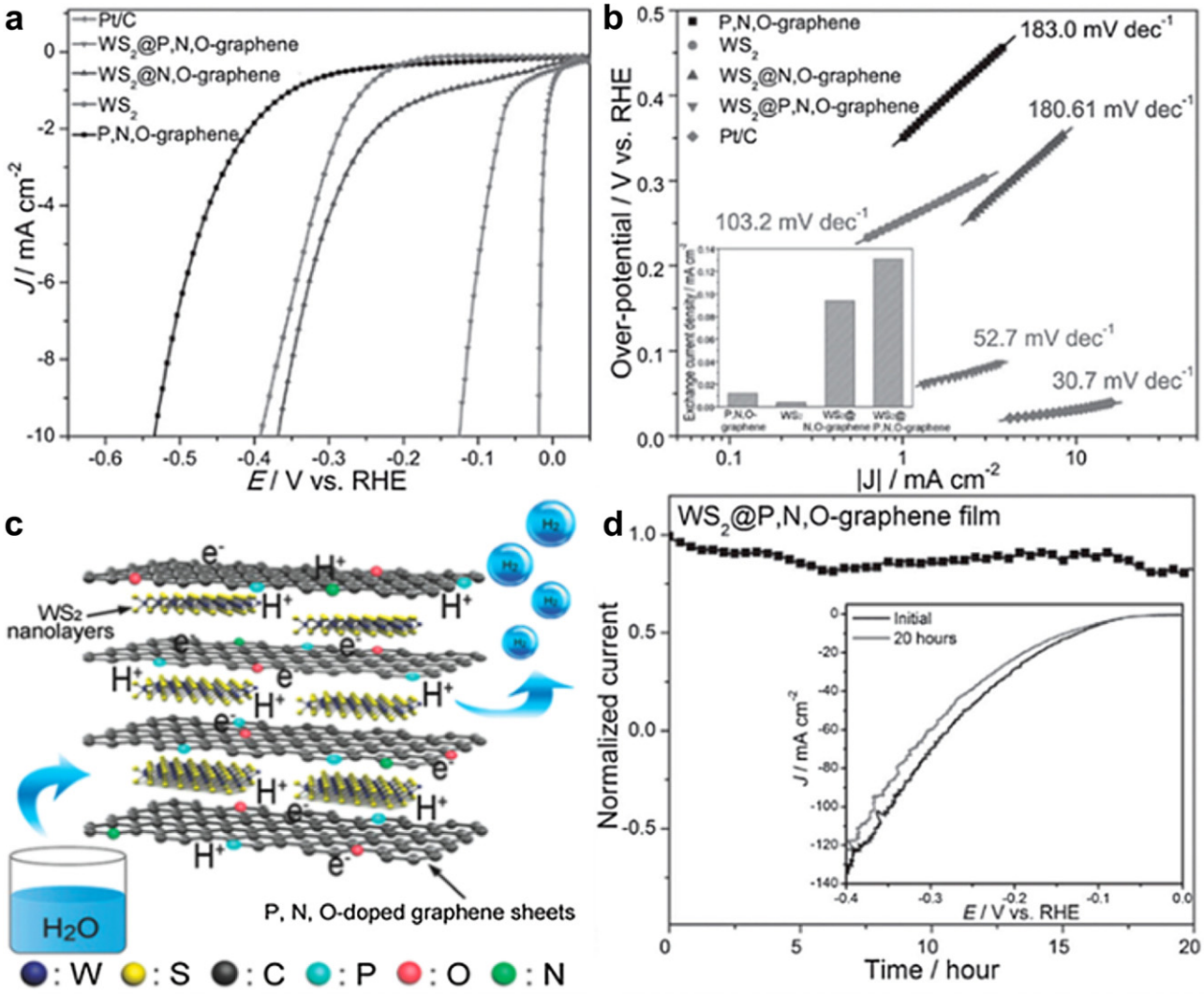

Fig. 17. (a) Polarization curves below 10 mA cm^{-2}, (b) Tafel plots, inset shows the exchange current density. (c) A schematic representation of the HER process. (d) Chronoamperometric response of WS_2@P,N,O-graphene film, inset shows the polarization curves before and after 20 h' operating.
Reproduced with permission from Ref. [204]. Copyright 2015, John Wiley & Sons, Inc.

of Co and Mn oxides and their hydroxides, and 9 times better compared to the TOF of a precious IrO_2 catalyst. The activity of the catalyst was increased by anodic conditioning, which was recommended to form amorphous regions and reactive Co(IV) species on surface.

As shown above, carbon nanomaterials (graphene, CNTs et al.) doped with N could be an efficient, low-cost, metal-free alternative to Pt for ORR. And Co/N-doped carbon nanomaterials with the second heteroatom, such as S, B, or P, can modulate the electronic performances and surface polarities to further promote the ORR activity. Conversely, the most electrocatalysts reported for OER until now are based on the transitionmetal supported on carbon materials to promote electron transfer. Although the development of noble metal-based bifunctional catalysts had attracted considerable attention [343,344], their high cost and poor durability severely hindered their applicability to broad commercialization. So it is extremely challenging but desirable to develop efficient bifunctional electrocatalysts possessing excellent durability and low cost for ORR and OER to replace conventional precious metals utilized in regenerative fuel cells. Our group prepared a hybrid composite of Co NPs embedded in N-doped carbon (Co/N-C-800), which showed highly efficient bifunctional catalytic activity and excellent stability toward both ORR and OER in alkaline solution [345]. In addition, metal-free bifunctional ORR and OER catalyst has been reported. For instance, 3D P and N double-doped mesoporous nanocarbon foams, barely by pyrolysis of polyaniline aerogels prepared in the presence of phytic acid has a large surface area of ~1663 m^2 g^{-1} and good electrocatalytic properties for both ORR and OER [346]. Wei et al. prepared N-doped graphene/CNTs nanohybrids as the efficient metal-free bifunctional electrocatalyst for both ORR and OER [347]. While on the other hand, electrocatalytic water splitting to hydrogen and oxygen is a promising and appealing solution that has attracted significant attention [348]. And this kind of bifunctional electrocatalyst have been demonstrated as state-of-the-art catalysts for HER and OER [349]. Co_9S_8@MoS_2 core-shell structures formed on CNFs with cubic Co_9S_8 as the core and layered MoS_2 as the shell can be directly used as an electrode for HER and OER and displays excellent stability [241]. The high hydrogen and oxygen evolution activities of the Co_9S_8@MoS_2 are due to the electrocatalytic synergetic effects of the nanointerfaces generated by the directly contacting regions between the Co_9S_8 core and the MoS_2 shell.

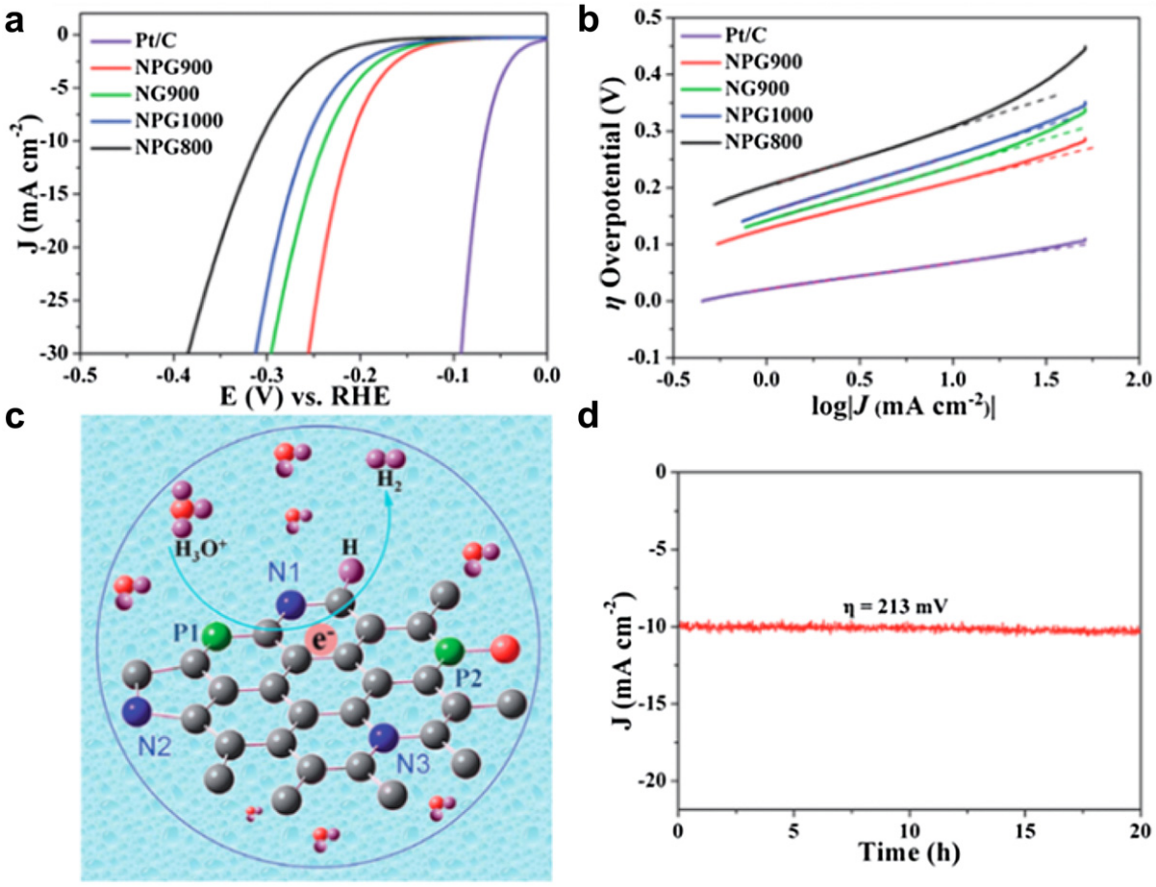

Fig. 18. (a) Polarization curves of various samples and (b) the corresponding Tafel plots. (c) A schematic representation of the HER process on the surface of NPG. The gray balls represent C atoms, green for P, blue for N, red for O and purple for H. (d) Time dependence of cathodic current density of NPG900 over 20 h at a fixed over potential of 213 mV.

Reproduced with permission from Ref. [155]. Copyright 2015, Royal Society of Chemistry.

Other applications

In addition to the aforementioned applications, other kinds of potential applications, such as transparent conductive electrodes, photocatalysis, sensors, absorbents, and biological applications, of these 3D architectures have also been demonstrated.

Flexible devices

Flexible devices related to energy storage and conversion have potential applications in portable and wearable electronics such as electronic papers, roll-up displays, active radio-frequency identification tags, touch screens, wearable sensors and implantable medical devices [350]. Thereby, they have attracted a good deal of attention in last several years from both industrial and academic aspects. Shi et al. prepared self-standing graphene flexible conductivity materials with 3D porous microstructures for large scale production [92]. The conductivity and density of these rGO aerogels can be modulated by the concentrations of feeding GO dispersions. They possessed light (6.73–12.32 mg cm^{-3}), conductive (0.48–1.76 S m^{-1}), and superior elasticity properties. The aerogel synthesized from 5 mg mL^{-1} GO could recover to its initial shape upon repeated compression up to 30% strain for the three hundred cycles. On the other hand, the gel-film transformation technique had synthesized rGO films containing trace amounts (<8%, by weight; wt%) of poly(acrylic acid-co-(4-acrylamidophenyl)boronic acid) ($PAPB_{0.2}$, the subscript refers to the molar ratio of carboxylate groups amidated with 3-aminophenylboronic acid) [108]. The film with 4 wt% $PAPB_{0.2}$ displayed the electrical conductivity of 337 ± 12 S cm^{-1}, their tensile strength of 381.78 ± 11.83 MPa, and the toughness of 7.50 ± 0.40 MJ m^{-3}. Especially, it achieved an excellent gravimetric particular strength (208 N m g^{-1}) than those of widely used metals or alloys such as stainless steel, Mg, Al and Ti alloys.

Graphene/polymer composites can also be synthesized by in situ growth of polymers in graphene matrices. Our group have manufactured an integrated 3D porous CNT/graphene and p-PDMS composite with excellent electrical performance [129]. The electrical conductivity of the pPCG reaches 27 S m^{-1} with only 2 wt% CNTs/graphene, and the value maintained constant after bending 5000 times and after 100 cycles of a 5% stretching-releasing process (Fig. 19). In addition, during the stretching process, the σ of the pPCG maintained unchanged (0–5% strains), after a slight decrease, the σ of the pPCG maintained invariant again to up to 50% strain. These phenomena could be quantitatively identified by simulating the mechanical performances through theoretical modeling of p-PDMS. The FEA displayed the large ε_{appl} could be accommodated by rotations and bending of cell walls, and the largest deformations presented primarily on the joints of struts. The stretchable composite displays superior cyclic electrical performances. When the composites were stretched to 10% and 50%, the σ of the pPCG only reduced by 20% and 25%, respectively, during the first stretching process and then maintained unchanged during the retention of the stretching releasing cycles. In the above, the strategy supplies a facile, inexpensive and simple industrial approach for manufac-

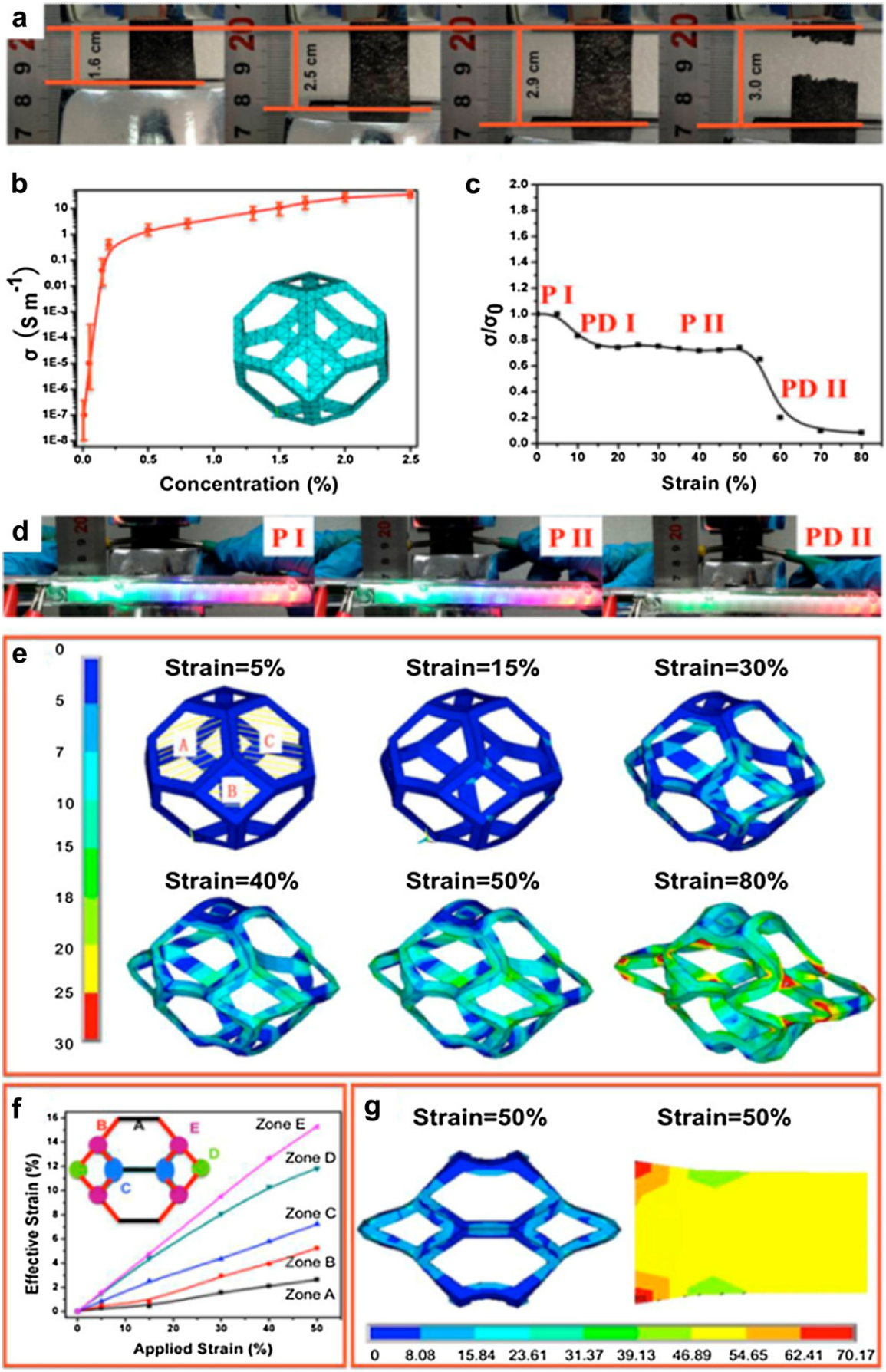

Fig. 19. (a) Photographs of pPCG films during the stretching process. (b) Conductivity of the pPCG composites with MWCNTs/graphene loading. (c) Normalized conductivity

turing a novel SCM that shows many fascinating performances for applications in stretchable next-generation electronics.

Solar photocatalytic applications

It has been demonstrated that some of these prepared 3D architectures could be promising photocatalysts for water splitting and photodegradation [95,230,268]. Such as, the TiO_2/MoS_2/graphene composites achieved the H_2 production rate of 165.3 μmol h^{-1}, and the apparent quantum efficiency reached 9.7% at 365 nm [226]. Zhu et al. developed Au-Pd alloy NPs supported on phosphate anion modified hydrotalcite to be active and selective for the direct oxidative esterification of aliphatic alcohols under visible-light irradiation using molecular oxygen as a benign oxidant [307]. Recently, Kang et al. reported the design and preparation of carbon nanodot-C_3N_4 nanocomposite and showed its impressive property for photocatalytic solar water splitting [280]. And the quantum efficiencies were 16% under wavelength 420 ± 20 nm, 6.29% for 580 ± 15 nm, and 4.42% for 600 ± 10 nm, determined the overall solar energy conversion efficiency of 2.0%. Yang et al. synthesized the macroscopic 3D porous *g*-C_3N_4 monolith for the photocatalytic hydrogen evolution [268]. Because of its plentiful porosity, excellent particular surface area, great visible light capture, as well as excellent charge separation efficiency, the product displays superior photocatalytic activity, which is 2.84 times higher compared to that of *g*-C_3N_4 powder for hydrogen evolution under visible light. In view of its freestanding structure, great mechanical strength, acceptable elasticity, and excellent photocatalytic activity, the macroscopic 3D porous *g*-C_3N_4 monolith shows great potential for the applications in the fields of water splitting, pollutant degradation, CO_2 reduction, and energy storage devices. In addition, *g*-C_3N_4 nanosheets/N-doped graphene/layered MoS_2 ternary nanojunction provided the widely optical window for effective light harvesting, short diffusion distance for superior charge transport, as well as the large contact area for fast interfacial charge separation and photoelectrochemical reactions [230]. Due to the special structure of AgX/graphene aerogels, the bulk composite materials could only just be recycled by directly clipping out using tweezers and washed with deionized water several times [95]. After the cycling photocatalysis, only very little quality loss was inspected and the morphology also maintained invariant. Superior cycling property had also been well retained even after multiple cycles on photocatalytic reactions. The corresponding photocatalytic degradation mechanism had been explained both theoretically and experimentally (Fig. 20). On the whole, in the photocatalytic system, the introduction of graphene aerogels had obviously increased the photocatalytic property. As a capable substrate for a photocatalyst, graphene aerogels had a general applicability and were anticipated to increase the evolution of photocatalysis toward commercial applications.

Biosensors and gas-sensing devices

3D architectures are efficient biosensors and gas-sensing devices owing to their low-mass densities, large surface areas, good mechanical stabilities and high electrical conductivities [21,22,141,351,352]. Yavari et al. [351] reported highly sensitive gas detectors using macroscopic 3D graphene networks. The performances of graphene-based foams as the active material in sensing devices were evaluated by monitoring their change in resistance ($\triangle R/R$) as a function of time in a chemiresistor with a four-probe configuration for different analyst concentrations. The $\triangle R/R$ of the graphene foams active layers decreased from ~30% for 1000 ppm to ~5% for 20 ppm of NH_3, exhibiting an improved sensitivity relative to individual single-wall nanotube device and commercially available conducting polymer sensors. In addition to NH_3, graphene-based foams sensors exhibit high efficiencies for detecting NO_2 with a $\triangle R/R$ of ~4% for 20 ppm NO_2. And Chen et al. developed the sensitive and selective field-effect transistor (FET) biosensor using vertically-oriented graphene (VG) sheets labeled with gold nanoparticle (NP)-antibody conjugates [141]. The protein detection is accomplished through measuring changes in the electrical signal from the FET sensor upon the antibody-antigen binding. The novel biosensor with unique graphene morphology shows high sensitivity (down to ~2 ng mL^{-1} or 13 pM) and selectivity towards specific proteins.

Adsorptive remediation of environmental pollutants

One of the important features of 3D architectures is their large accessible specific surface areas, and thus they can effectively absorb organic and inorganic contaminants. Furthermore, these 3D foams can be easily separated from solution, making them convenient to collect and recyclable. 3D graphene-based foams can be used as super absorbers in environmental remediation to remove a range of organic contaminants and heavy metal ions with high efficiencies [22,97,98,137,353]. In addition, 3D white graphene foam exhibited much higher adsorption capacities to these organics and oils compared with many competitors, as shown in Fig. 21 [282]. The rapid and effective adsorption behaviors were directly visualized. After dipping the 3D white graphene foams into an aqueous solution of chloroform, which was intentionally stained with Sudan III to mark the foams red in color, these red pollutants absorbed rapidly and completely within 2 min. The adsorption capacity of the 3D white graphene foams was up to 70–190 times its own weight for organic pollutants and oils. For pump oil, a common pollutant, the typical adsorption capacity of 3D white graphene foams was as high as 115 g g^{-1}, and this means that only 1 kg of 3D white graphene foams is needed to purify 1 ton of water containing 10% oil pollutant. To more quantitatively evaluate the adsorption capacity of 3D white graphene foams, several recently reported excellent sorbents and commercial activated carbon powders were adopted for comparison. Taking the adsorption of pump oil as the instance, the adsorption capacity (115 g g^{-1}) of the 3D white graphene foams was higher compared to all of these competitors. Compared with the commercial BN and active carbon powders, the adsorption capacity of these 3D white graphene foams was 420 times larger compared to these typical sorbents. After 7 test cycles and heat treatments under 100 °C, the adsorption capacities of the 3D white graphene foams still maintained 490% toward both ethanol and chloroform. As for pump oil, the removal efficiency was still retained at about 85% even after 5 cycles via the direct combustion in air. Expressly, these results showed the prepared 3D white graphene foams could be deliberated extremely effective and recyclable sorbents for the removal of pollutants in environment purification. The superstrong competitive power of 3D white graphene foams over other sorbents arose from their two crucial features, large-yield configuration and hierarchical pores, that both profited from the vesicant-assisted foaming. Due of the unique structure with hierarchical pores, the 3D white graphene possessed excellent pollutant removal performances.

of the composites as the function of tensile strain. (d) Brightness of LED lamps depending on these strains. (e) Tetrakaidecahedron model of porous *p*-PDMS under stretching along the X-axis, in which different strain models display clear deformation on each spot. (f) Average strains of the tetrakaidecahedron calculated by FEA in the five zones as the function of applied strains. (g) Comparison of strain distributions between the porous p-PDMS and solid PDMS models.

Reproduced with permission from Ref. [129]. Copyright 2014, John Wiley & Sons, Inc.

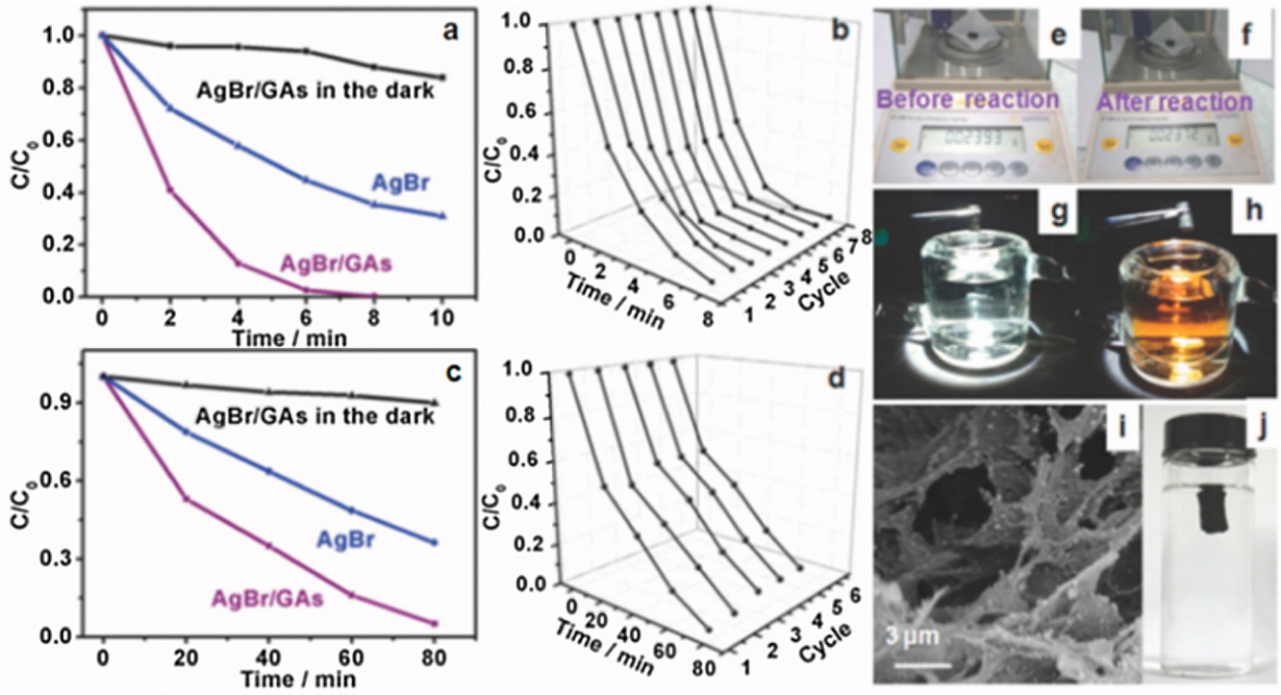

Fig. 20. (a) Photocatalytic oxidative curves of MO by AgBr and AgBr/GAs under visible light (λ > 420 nm), the absorptive curve of AgBr/GAs in the dark environment. (b) Eight successive photodegradation dynamic curves of MO over AgBr/GAs. (c) Photocatalytic reductive curves of Cr^{VI} by AgBr and AgBr/GAs under visible light and the adsorptive curve of AgBr/GAs in the dark environment. (d) Five successive photoreductive dynamic curves of Cr^{VI} over AgBr/GAs. (e) The quality of AgBr/GAs before photocatalytic reaction. (f) The quality of AgBr/GAs after photocatalytic reaction. (g) Tweezers are just used to take the AgBr/GAs from completed reaction system. (h) Tweezers are just used to take the AgBr/GAs to a fresh system without centrifugation, ultrasound, and drying process. (i) SEM image of AgBr/GAs after photocatalysis reaction. (j) The AgBr/GAs composite suspends in the aqueous solution.

Reproduced with permission from Ref. [95]. Copyright 2015, John Wiley & Sons, Inc.

Biomedical applications

3D architectures also display well potential in biomedical applications [115,354,355]. The first research used 3D graphene foams as cell culture substrates for human bone marrow-derived mesenchymal stem cells (hMSCs) [354]. 3D graphene networks retained the hMSC viability and stimulate changes in the morphology and protein expression patterns, indicating that spontaneous osteogenic differentiation arised without extrinsic biochemical inputs. Tang et al. studied the pro- and anti-inflammatory responses of microglia in the graphene foams culturing systems [355]. They established that graphene foams supported the growth of microglia and displayed comparable biocompatibility with commercially available tissue culture PS. Shah et al. showed the 3D printable graphene (3DG) composites consisting of majority graphene and minority polylactide-co-glycolide, a biocompatible elastomer, 3D-printed from a liquid ink [115]. In vitro experiments in simple growth medium, in the absence of neurogenic stimuli, reveal that 3DG supports hMSCs adhesion, viability, proliferation, and neurogenic differentiation with important upregulation of glial and neuronal genes. This coincides with hMSCs adopting extremely elongated morphologies with features as well as axons and presynaptic terminals. In vivo experiments demonstrated that 3DG had promising biocompatibility over the course of at least 30 days. Surgical tests using a human cadaver nerve model also evidenced that 3DG had exceptional handling characteristics and could be intraoperatively manipulated and applied to fine surgical procedures. With this special set of performances, combined with ease of preparation, 3DG could be applied toward the design and preparation of a wide range of functional biological, electronic, and bioelectronic medical and nonmedical devices.

Conclusion and outlook

Currently, the development of advanced materials and processes is widely regarded as a key response to the challenges of the 21 st century including climate change, disease control and securing the supply of clean water, food and energy. Due to the large surface area and macro/mesoporous structure, 3D architectures materials exhibit their unique excellent performances in the above fields. In this review, we have outlined recently developed methods for the preparation of 3D architectures hydric materials, including co-assembly, template methods and *in-situ* synthesis. The composites of unique hierarchical architecture often provided multidimensional electronic network, and numerous open channels for the access of the reactant, thus providing a new material platform for applications in nanoelectronics, energy materials, and catalysts.

No matter their potential application, the first target is to prepare it in a controlled fashion. Firstly, it is the precise control of the 3D nanostructures, including the growth of the layers, pore size and porosity. Most of these reported 3D architectures have a wide pore size distribution, ranging from one hundred to several hundreds of micrometers. Large pore sizes decrease the mechanical performances of the resulting materials. Thereby, single-layered 3D architectures are hardly ever prepared, due to their fragile mechanical performances and large pore sizes. The preparation of 3D architectures with uniform meso- or micropores and controlled layers are much necessary. In the template-assisted synthesis, the preparation of a template with uniform meso- or micropores is significant. In the assembly method, gaining more control over the layer growth and size of the 2D nanosheets would be helpful. The second challenge is to further enhance the mechanical

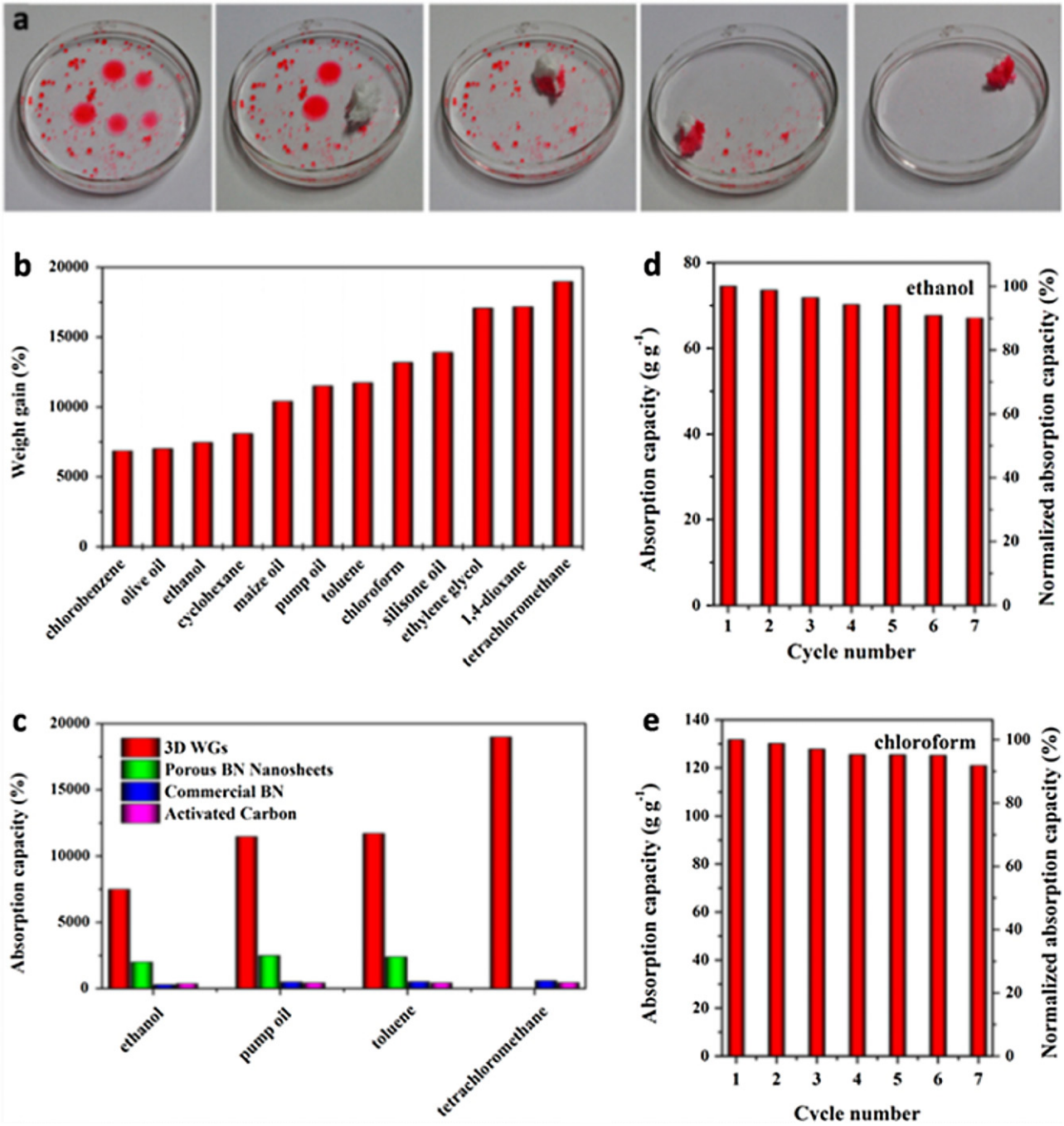

Fig. 21. Excellent adsorption performances of 3D white graphene (WG) foams toward various organic contaminations. (a) Visual variation of the 3D WG-immersed chloroform solution within 1 min, showing the effective and speedy adsorption ability. (b) Adsorption capacities of the 3D WG foams toward various organic contaminations. (c) Comparison of the contamination adsorption capacities of the 3D WG foams with other typical sorbents, including commercial activated carbon. Chloroform (d) and ethanol (e) adsorption recyclability of 3D WG foams.

Reproduced with permission from Ref. [282]. Copyright 2015, Nature Publishing Group.

and electrical performances of the 3D architectures. Increasing and strengthening the cross-linking between the nanosheets by enhancing the surface functional moieties or adding cross-linkers will enhance the inter-sheet binding of the nanosheets and the mechanical and electrical performances. Thereby, continued innovative research and development is required to further enhance the performances and applications of 3D architectures.

In the other hand, for applications in catalysis, energy storage and conversion, an advanced hybrid nanostructure should generally meet the requirements of large particular surface area for reaction, ion exchange or light adsorption, the conductive networks for charge transport, and the interface/heterojunction formed by two components for the effective channeling or separation of charge carriers. Among these requirements, much effort has been devoted to heightening the effective surface area of these hybrids. But the particular surface area could never go beyond the theoretical value of the monolayer nanosheet. One possible strategy is to establish high-density nanosized holes in the 2D nanomaterials via etch-based approachs or the defect configuration during doping hetero atom. As such, the resulting nanoporous sheet structure can

possess a surface area much larger compared to the theoretical value of a seamless 2D material, and simultaneously supply plenty of active edge sites for various reactions.

In addition, the material engineering of 3D architectures is combined composite or hybrid materials. The original techniques could help us access a large number of graphene analogues-based 3D nanocomposites/nanohybrids, which not only integrate the performances of the individual 2D nanomaterials, but also bring new collective and synchronic functions. Furthermore, improved properties of 2D nanomaterials at the nanoscale can be inspected owing to the synergetic chemical coupling effects. On these based, we should attach importance to the fundamental understanding of the principles of these synergistic coupling effects. For instance, an in-depth understanding of the ORR mechanisms and the relationship between the composition and structure of the catalyst active sites is beneficial to tailor novel catalyst structures and ORR activity levels. Furthermore, more theoretical investigations into the electronic properties, crystal and surface structure in the different 3D architectures as well as synergetic effects of modified- graphene analogues-based nanomaterials should be made based on first-principle calculations, which in combination with smart experimental strategies will greatly shorten the development process of extremely efficient graphene analogues-based 3D nanocomposites for energy conversion and storage or other applications.

Ultimately, we need to address the problem of large-scale production, manufacturing of nanomaterials is an interdisciplinary field covering chemistry, biology, physics, materials science and engineering. The interaction between scientists with different disciplines will undoubtedly lead to the production of 2D and 3D nanomaterials with tailored performances. The success of nanomanufacturing depends on the intense cooperation between industry and academia so as to be informed about current needs and future challenges, to design products directly transferred into the industrial sector. It is of paramount importance the selection of the appropriate approach combining synthesis of nanomaterials with required performances and limited impurities as well as scalability of the technique. However, the above summary prepared methods are not suitable for larger-scale production. And these newly developed 3D architectures hydric nanomaterials manufacturing approaches, although still in research labs, are expected to supply with nanostructures and nanoparticles of high process throughput and low product costs. Affirmatively, the existing gap between basic research relating them and their application in real life will be overcome in the next decade.

Acknowledgements

This work was supported by the National Natural Science Foundation of China (21136006, 21206043, 21322607, 21406072, 21471056 and 91534202), Shanghai Educational Development Foundation (14CG29), Basic Research Program of Shanghai (15JC1401300), International Science and Technology Cooperation Program of China (2015DFA51220), Program for Professor of Special Appointment(Eastern Scholar) at Shanghai Institutions of Higher Learning, Project funded by China Postdoctoral Science Foundation (2014M560307, 2014M561497, 2015T80408), and the Fundamental Research Funds for the Central Universities.

References

[1] K.S. Novoselov, A.K. Geim, S.V. Morozov, D. Jiang, Y. Zhang, S.V. Dubonos, I.V. Grigorieva, A.A. Firsov, Science 306 (2004) 666–669.
[2] K.S. Novoselov, V.I. Fal'ko, L. Colombo, P.R. Gellert, M.G. Schwab, K. Kim, Nature 490 (2012) 192–200.
[3] D.S.L. Abergel, V. Apalkov, J. Berashevich, K. Ziegler, T. Chakraborty, Adv. Phys. 59 (2010) 261–482.
[4] K.S. Novoselov, A.K. Geim, S.V. Morozov, D. Jiang, M.I. Katsnelson, I.V. Grigorieva, S.V. Dubonos, A.A. Firsov, Nature 438 (2005) 197–200.
[5] K.I. Bolotin, F. Ghahari, M.D. Shulman, H.L. Stormer, P. Kim, Nature 462 (2009) 196–199.
[6] L.A. Ponomarenko, R.V. Gorbachev, G.L. Yu, D.C. Elias, R. Jalil, A.A. Patel, A. Mishchenko, A.S. Mayorov, C.R. Woods, J.R. Wallbank, M. Mucha-Kruczynski, B.A. Piot, M. Potemski, I.V. Grigorieva, K.S. Novoselov, F. Guinea, V.I. Fal'ko, A.K. Geim, Nature 497 (2013) 594–597.
[7] K.I. Bolotin, K.J. Sikes, Z. Jiang, M. Klima, G. Fudenberg, J. Hone, P. Kim, H.L. Stormer, Solid State Commun. 146 (2008) 351–355.
[8] A.H. Castro-Neto, F. Guinea, N.M.R. Peres, K.S. Novoselov, A.K. Geim, Rev. Mod. Phys. 81 (2009) 109–162.
[9] N.O. Weiss, H. Zhou, L. Liao, Y. Liu, S. Jiang, Y. Huang, X. Duan, Adv. Mater. 24 (2012) 5782–5825.
[10] S.Z. Butler, S.M. Hollen, L. Cao, Y. Cui, J.A. Gupta, H.R. Gutiérrez, T.F. Heinz, S.S. Hong, A.F. Ismach, E. Johnston-Halperin, M. Kuno, V.V. Plashnitsa, R.D. Robinson, R.S. Ruoff, S. Salahuddin, J. Shan, L. Shi, M.G. Spencer, M. Terrones, W. Windl, J.E. Goldberger, ACS Nano 7 (2013) 2898–2926.
[11] M.S. Xu, T. Liang, M.M. Shi, H. Chen, Chem. Rev. 113 (2013) 3766–3798.
[12] C. Tan, H. Zhang, Chem. Soc. Rev. 44 (2015) 2713–2731.
[13] X. Huang, Z.Y. Zeng, H. Zhang, Chem. Soc. Rev. 42 (2013) 1934–1946.
[14] Y.F. Sun, S. Gao, Y. Xie, Chem. Soc. Rev. 43 (2014) 530–546.
[15] Y. Ma, Y. Chen, Natl. Sci. Rev. 2 (2015) 40–53.
[16] X. Cao, Z. Yin, H. Zhang, Energy Environ. Sci. 7 (2014) 1850–1865.
[17] N. Leventis, Acc. Chem. Res. 40 (2007) 874-.
[18] B. Dunn, J.I. Zink, Acc. Chem. Res. 40 (2007) 874–884.
[19] J. Biener, M. Stadermann, M. Suss, M.A. Worsley, M.M. Biener, K.A. Rose, T.F. Baumann, Energy Environ. Sci. 4 (2011) 656–667.
[20] S. Nardecchia, D. Carriazo, M.L. Ferrer, M.C. Gutiérrez, F. del Monte, Chem. Soc. Rev. 42 (2013) 794–830.
[21] V. Chabot, D. Higgins, A.P. Yu, X. Xiao, Z. Chen, J. Zhang, Energy Environ. Sci. 7 (2014) 1564–1596.
[22] C. Li, G. Shi, Nanoscale 4 (2012) 5549–5563.
[23] B. Luo, L. Zhi, Energy Environ. Sci. 8 (2015) 456–477.
[24] C. Li, G. Shi, Adv. Mater. 26 (2014) 3992–4012.
[25] S. Han, D. Wu, S. Li, F. Zhang, X. Feng, Adv. Mater. 26 (2014) 849–864.
[26] Z. Chen, W. Ren, L. Gao, B. Liu, S. Pei, H.M. Cheng, Nat. Mater. 10 (2011) 424–428.
[27] H. Bi, X. Xie, K. Yin, Y. Zhou, S. Wan, L. He, F. Xu, F. Banhart, L. Sun, R.S. Ruoff, Adv. Funct. Mater. 22 (2012) 4421–4425.
[28] X. Zhang, Z. Sui, B. Xu, S. Yue, Y. Luo, W. Zhan, B. Liu, J. Mater. Chem. 21 (2011) 6494–6497.
[29] M.A. Worsley, P.J. Pauzauskie, T.Y. Olson, J. Biener, J.H. Satcher, T.F. Baumann, J. Am. Chem. Soc. 132 (2010) 14067–14069.
[30] Y.F. Ma, Y.S. Chen, Natl. Sci. Rev. 2 (2015) 40–53.
[31] K.S. Novoselov, D. Jiang, F. Schedin, T.J. Booth, V.V. Khotkevich, S.V. Morozov, A.K. Geim, Proc. Natl. Acad. Sci. U. S. A. 102 (2005) 10451–10453.
[32] H. Matte, A. Gomathi, A.K. Manna, D.J. Late, R. Datta, S.K. Pati, C.N.R. Rao, Angew. Chem. 122 (2010) 4153–4156.
[33] Z.Y. Zeng, Z.Y. Yin, X. Huang, H. Li, Q.Y. He, G. Lu, F. Boey, H. Zhang, Angew. Chem. Int. Ed. 50 (2011) 11093–11097.
[34] X.H. Li, M. Antonietti, Chem. Soc. Rev. 42 (2013) 6593–6604.
[35] J.N. Coleman, M. Lotya, A. O'Neill, S.D. Bergin, P.J. King, U. Khan, K. Young, A. Gaucher, S. De, R.J. Smith, I.V. Shvets, S.K. Arora, G. Stanton, H.Y. Kim, K. Lee, G.T. Kim, G.S. Duesberg, T. Hallam, J.J. Boland, J.J. Wang, J.F. Donegan, J.C. Grunlan, G. Moriarty, A. Shmeliov, R.J. Nicholls, J.M. Perkins, E.M. Grieveson, K. Theuwissen, D.W. McComb, P.D. Nellist, V. Nicolosi, Science 33 (2011) 568–571.
[36] Z. Zeng, T. Sun, J. Zhu, X. Huang, Z. Yin, G. Lu, Z. Fan, Q. Yan, H.H. Hng, H. Zhang, Angew. Chem. Int. Ed. 51 (2012) 9052–9056.
[37] Z.Y. Yin, H. Li, L. Jiang, Y.M. Shi, Y.H. Sun, G. Lu, Q. Zhang, X.D. Chen, H. Zhang, ACS Nano 6 (2012) 74–80.
[38] A. Splendiani, L. Sun, Y.B. Zhang, T.S. Li, J. Kim, C.Y. Chim, G. Galli, F. Wang, Nano Lett. 10 (2010) 1271–1275.
[39] Y.J. Zhang, J.T. Ye, Y. Matsuhashi, Y. Iwasa, Nano Lett. 12 (2012) 1136–1140.
[40] Q. He, Z. Zeng, Z. Yin, H. Li, S. Wu, X. Huang, H. Zhang, Small 8 (2012) 2994–2999.
[41] H. Li, G. Lu, Z.Y. Yin, Q.Y. He, Q. Zhang, H. Zhang, Small 8 (2012) 682–686.
[42] H. Li, Z.Y. Yin, Q.Y. He, X. Huang, G. Lu, D.W.H. Fam, A.I.Y. Tok, Q. Zhang, H. Zhan, Small 8 (2012) 63–67.
[43] S. Wu, Z. Zeng, Q. He, Z. Wang, S.J. Wang, Y. Du, Z. Yin, X. Sun, W. Chen, H. Zhang, Small 8 (2012) 2264–2270.
[44] J. Liu, Z. Zeng, X. Cao, G. Lu, L.H. Wang, Q.L. Fan, W. Huang, H. Zhang, Small 8 (2012) 3517–3522.
[45] Y. Jing, Z. Zhou, C.R. Cabrera, Z.F. Chen, J. Mater. Chem. A 2 (2014) 12104–12122.
[46] M.R. Gao, Y.F. Xu, J. Jiang, S.H. Yu, Chem. Soc. Rev. 42 (2013) 2986–3017.
[47] C.L. Tan, Z.D. Liu, W. Huang, H. Zhang, Chem. Soc. Rev. 44 (2015) 2615–2628.
[48] M. Chhowalla, H.S. Shin, G. Eda, L.J. Li, K. Loh, H. Zhang, Nat. Chem. 5 (2013) 263–275.
[49] Y. Chen, C.L. Tan, H. Zhang, L.Z. Wang, Chem. Soc. Rev. 44 (2015) 2681–2701.
[50] X. Huang, X.Y. Qi, F. Boey, H. Zhang, Chem. Soc. Rev. 41 (2012) 666–686.
[51] X. Huang, C.L. Tan, Z.Y. Yin, H. Zhang, Adv. Mater. 26 (2014) 2185–2204.
[52] X. Huang, Z.Y. Zeng, S.Y. Bao, M.F. Wang, X.Y. Qi, Z.X. Fan, H. Zhang, Nat. Commun. 4 (2013) 1444.

[53] J. Kim, S. Byun, A.J. Smith, J. Yu, J.X. Huang, J. Phys. Chem. Lett. 4 (2013) 1227–1232.
[54] Y.M. Shi, J.K. Huang, L.M. Jin, Y.T. Hsu, S.F. Yu, L.J. Li, H.Y. Yang, Sci. Rep. 3 (2013) 1839.
[55] T.S. Sreeprasad, P. Nguyen, N. Kim, V. Berry, Nano Lett. 13 (2013) 4434–4441.
[56] Z.Y. Zeng, C.L. Tan, X. Huang, S.Y. Bao, H. Zhang, Energy Environ. Sci. 7 (2014) 797–803.
[57] Y.M. Kang, S. Najmaei, Z. Liu, Y.J. Bao, Y.M. Wang, X. Zhu, N.J. Halas, P. Nordlander, P.M. Ajayan, J. Lou, Z.Y. Fang, Adv. Mater. 26 (2014) 6467–6741.
[58] Z.Y. Yin, X. Zhang, Y.Q. Cai, J.Z. Chen, J.I. Wong, Y.Y. Tay, J.W. Chai, J. Wu, Z.Y. Zeng, B. Zheng, H.Y. Yang, H. Zhang, Angew. Chem. Int. Ed. 53 (2014) 12560–12565.
[59] J.M. Yun, Y.J. Noh, C.H. Lee, S.I. Na, S. Lee, S.M. Jo, H.I. Joh, D.Y. Kim, Small 10 (2014) 2319–2324.
[60] X. Xu, Z.Y. Fan, S.J. Ding, D.M. Yu, Y.P. Du, Nanoscale 6 (2014) 5245–5250.
[61] Y.P. Huang, Y.E. Miao, L.S. Zhang, W.W. Tjiu, J.S. Pan, T.X. Liu, Nanoscale 6 (2014) 10673–10679.
[62] Y. Zhang, Q.Q. Ji, G.F. Han, J. Ju, J.P. Shi, D.L. Ma, J.Y. Sun, Y.S. Zhang, M.J. Li, X.Y. Lang, Y.F. Zhang, Z.F. Liu, ACS Nano 8 (2014) 8617–8624.
[63] L. Cheng, J.J. Liu, X. Gu, H. Gong, X.Z. Shi, T. Liu, C. Wang, X.Y. Wang, G. Liu, H.Y. Xing, W.B. Bu, B.Q. Sun, Z. Liu, Adv. Mater. 26 (2014) 1886–1893.
[64] T. Liu, C. Wang, X. Gu, H. Gong, L. Cheng, X.Z. Shi, L.Z. Feng, B.Q. Sun, Z. Liu, Adv. Mater. 26 (2014) 3433–3440.
[65] W.Y. Yin, L. Yan, J. Yu, G. Tian, L.J. Zhou, X.P. Zheng, X. Zhang, Y. Yong, J. Li, Z.J. Gu, Y.L. Zhao, ACS Nano 8 (2014) 6922–6933.
[66] Y. Yong, L.J. Zhou, Z.J. Gu, L. Yan, G. Tian, X.P. Zheng, X.D. Liu, X. Zhang, J.X. Shi, W.S. Cong, W.Y. Yin, Y.L. Zhao, Nanoscale 6 (2014) 10394–10403.
[67] S.K. Kim, J.J. Wie, Q. Mahmooda, H.S. Park, Nanoscale 6 (2014) 7430–7435.
[68] D.O. Dumcenco, H. Kobayashi, Z. Liu, Y.S. Huang, K. Suenaga, Nat. Commun. 4 (2013) 1351.
[69] Y.F. Chen, J.Y. Xi, D.O. Dumcenco, Z. Liu, K. Suenaga, D. Wang, Z.G. Shuai, Y.S. Huang, L.M. Xie, ACS Nano 7 (2013) 4610–4616.
[70] H.L. Li, X.D. Duan, X.P. Wu, X.J. Zhuang, H. Zhou, Q.L. Zhang, X.L. Zhu, W. Hu, P.Y. Ren, P.F. Guo, L. Ma, X.P. Fan, X.X. Wang, J.Y. Xu, A.L. Pan, X.F. Duan, J. Am. Chem. Soc. 136 (2014) 3756–3759.
[71] J. Mann, Q. Ma, P.M. Odenthal, M. Isarraraz, D. Le, E. Preciado, D. Barroso, K. Yamaguchi, G. von Son Palacio, A. Nguyen, T. Tran, M. Wurch, A. Nguyen, V. Klee, S. Bobek, D.Z. Sun, T.F. Heinz, T.S. Rahman, R. Kawakami, L. Bartels, Adv. Mater. 26 (2014) 1399–1404.
[72] Q.L. Feng, Y.M. Zhu, J.H. Hong, M. Zhang, W.J. Duan, N.N. Mao, J.X. Wu, H. Xu, F.L. Dong, F. Lin, C.H. Jin, C.M. Wang, J. Zhang, L.M. Xie, Adv. Mater. 26 (2014) 2648–2653.
[73] J.F. Xie, J.J. Zhang, S. Li, F. Grote, X.D. Zhang, H. Zhang, R.X. Wang, Y. Lei, B.C. Pan, Y. Xie, J. Am. Chem. Soc. 135 (2013) 17881–17888.
[74] C.W. Lin, X.J. Zhu, J. Feng, C.Z. Wu, S.L. Hu, J. Peng, Y.Q. Guo, L.L. Peng, J.Y. Zhao, J.L. Huang, J.L. Yang, Y. Xie, J. Am. Chem. Soc. 135 (2013) 5144–5151.
[75] K. Chang, W.X. Chen, ACS Nano 5 (2011) 4720–4728.
[76] D.Y. Chen, G. Ji, B. Ding, Y. Ma, B.H. Qu, W.X. Chen, J.Y. Lee, Nanoscale 5 (2013) 7890–7896.
[77] J. Yang, D. Voiry, S.J. Ahn, D. Kang, A.Y. Kim, M. Chhowalla, H.S. Shin, Angew. Chem. Int. Ed. 52 (2013) 13751–13754.
[78] X.H. Cao, Y.M. Shi, W.H. Shi, X.H. Rui, Q.Y. Yan, J. Kong, H. Zhang, Small 9 (2013) 3433–3438.
[79] X.L. Zheng, J.B. Xu, K.Y. Yan, H. Wang, Z.L. Wang, S.H. Yang, Chem. Mater. 26 (2014) 2344–2353.
[80] L. David, R. Bhandavat, G. Singh, ACS Nano 8 (2014) 1759–1770.
[81] X. Huang, B. Zheng, Z.D. Liu, C.L. Tan, J.Q. Liu, B. Chen, H. Li, J.Z. Chen, X. Zhang, Z.X. Fan, W.N. Zhang, Z. Guo, F.W. Huo, Y.H. Yang, L.H. Xie, W. Huang, H. Zhang, ACS Nano 8 (2014) 8695–8701.
[82] C.L. Tan, X.Y. Qi, X. Huang, J. Yang, B. Zheng, Z.F. An, R.F. Chen, J. Wei, B.Z. Tang, W. Huang, H. Zhang, Adv. Mater. 26 (2014) 1735–1739.
[83] Y.C. Lin, D.O. Dumcenco, H.P. Komsa, Y. Niimi, A.V. Krasheninnikov, Y.S. Huang, K. Suenaga, Adv. Mater. 26 (2014) 2857–2861.
[84] C.L. Tan, H. Zhang, Chem. Soc. Rev. 44 (2015) 2713–2731.
[85] H. Li, J. Wu, Z.Y. Yin, H. Zhang, Acc. Chem. Res. 47 (2014) 1067–1075.
[86] S.M. Jung, H.Y. Jung, M.S. Dresselhaus, Y.J. Jung, J. Kong, Sci. Rep. 2 (2012) 849.
[87] F. Bonaccorso, L. Colombo, G.H. Yu, M. Stoller, V. Tozzini, A.C. Ferrari, R.S. Ruoff, V. Pellegrini, Science 347 (2015) 1246501–1246502.
[88] X. Sun, Y.Q. Guo, C.Z. Wu, Y. Xie, Adv. Mater. 27 (2015) 3850–3867.
[89] Z.H. Tang, S.L. Shen, J. Zhuang, X. Wang, Angew. Chem. Int. Ed. 49 (2010) 4603–4607.
[90] H. Jiang, P.S. Lee, C.Z. Li, Energy Environ. Sci. 6 (2013) 41–53.
[91] H. Jiang, J. Ma, C.Z. Li, Adv. Mater. 24 (2012) 4197–4202.
[92] Y.R. Li, J. Chen, L. Huang, C. Li, J.D. Hong, G.Q. Shi, Adv. Mater. 26 (2014) 4789–4793.
[93] X. Jiang, X.L. Yang, Y.H. Zhu, H.L. Jiang, Y.F. Yao, P. Zhao, C.Z. Li, J. Mater. Chem. A 2 (2014) 11124–11133.
[94] X. Jiang, X.L. Yang, Y.H. Zhu, K.C. Fan, P. Zhao, C.Z. Li, New J. Chem. 37 (2013) 3671–3678.
[95] Y.Y. Fan, W.G. Ma, D.X. Han, S.Y. Gan, X.D. Dong, L. Niu, Adv. Mater. 27 (2015) 3767–3773.
[96] C.X. Li, C.G. Hu, Y. Zhao, L. Song, J. Zhang, R.D. Huang, L.T. Qu, Carbon 78 (2014) 231–242.
[97] X. Wang, L.L. Lu, Z.L. Yu, X.W. Xu, Y.R. Zheng, S.H. Yu, Angew. Chem. 127 (2015) 2427–2431.
[98] X. Xu, H. Li, Q.Q. Zhang, H. Hu, Z.B. Zhao, J.H. Li, J.Y. Li, Y. Qiao, Y. Gogotsi, ACS Nano 9 (2015) 3969–3977.
[99] Y.R. Zhong, M. Yang, X.L. Zhou, Y.T. Luo, J.P. Wei, Z. Zhou, Adv. Mater. 27 (2014) 806–812.
[100] Y.X. Xu, Z.Y. Lin, X. Zhong, B. Papandrea, Y. Huang, X.F. Duan, Angew. Chem. Int. Ed. 54 (2015) 5345–5350.
[101] Y.J. Gong, H.L. Fei, X.L. Zou, W. Zhou, S.B. Yang, G. Ye, Z. Liu, Z.W. Peng, J. Lou, R. Vajtai, B.I. Yakobson, J.M. Tour, P.M. Ajayan, Chem. Mater. 27 (2015) 1181–1186.
[102] L. Chen, R. Du, J.H. Zhu, Y.Y. Mao, C. Xue, N. Zhang, Y.L. Hou, J. Zhang, T. Yi, Small 11 (2015) 1423–1429.
[103] W. Guo, C. Cheng, Y.Z. Wu, Y.N. Jiang, J. Gao, D. Li, L. Jiang, Adv. Mater. 25 (2013) 6064–6068.
[104] K. Hatakeyama, M.R. Karim, C. Ogata, H. Tateishi, A. Funatsu, T. Taniguchi, M. Koinuma, S. Hayami, Y. Matsumoto, Angew. Chem. Int. Ed. 53 (2014) 6997–7000.
[105] X.L. Yang, K.C. Fan, Y.H. Zhu, J.H. Shen, X. Jiang, P. Zhao, S.R. Luan, C.Z. LI, ACS Appl. Mater. Interfaces 5 (2013) 997–1002.
[106] Z.S. Wu, K. Parvez, S. Li, S. Yang, Z.Y. Liu, S.H. Liu, X.L. Feng, K. Müllen, Adv. Mater. 27 (2015) 4054–4061.
[107] Y.N. Meng, K. Wang, Y.J. Zhang, Z.X. Wei, Adv. Mater. 25 (2013) 6985–6990.
[108] M. Zhang, L. Huang, J. Chen, C. Li, G.Q. Shi, Adv. Mater. 26 (2014) 7588–7592.
[109] B. Rangasamy, J.Y. Hwang, W. Choi, Carbon 77 (2014) 1065–1072.
[110] M. Park, Y. Kim, Y. Ko, S. Cheong, S.W. Ryu, J. Cho, J. Am. Chem. Soc. 136 (2014) 17213–17223.
[111] Z.B. Xiao, Z. Yang, L. Wang, H.G. Nie, M.E. Zhong, Q.Q. Lai, X.J. Xu, L.J. Zhang, S.M. Huang, Adv. Mater. 27 (2015) 2891–2898.
[112] J.H. Shen, Y.H. Zhu, K.F. Zhou, X.L. Yang, C.Z. Li, J. Mater. Chem. 22 (2012) 545–550.
[113] X.L. Yang, K.C. Fan, Y.H. Zhu, J.H. Shen, X. Jiang, P. Zhao, C.Z. Li, J. Mater. Chem. 22 (2012) 17278–17283.
[114] J.H. Kim, W.S. Chang, D. Kim, J.R. Yang, J.T. Han, G.W. Lee, J.T. Kim, S.K. Seol, Adv. Mater. 27 (2015) 157–161.
[115] A.E. Jakus, E.B. Secor, A.L. Rutz, S.W. Jordan, M.C. Hersam, R.N. Shah, ACS Nano 9 (2015) 4636–4648.
[116] E. García-Tunon, S. Barg, J. Franco, R. Bell, S. Eslava, E. D'Elia, R.C. Maher, F. Guitian, E. Saiz, Adv. Mater. 27 (2015) 1688–1693.
[117] C. Zhu, T.Y.J. Han, E.B. Duoss, A.M. Golobic, J.D. Kuntz, C.M. Spadaccini, M.A. Worsley, Nat. Commun. 6 (2015) 6962.
[118] S.H. Choi, J.K. Lee, Y.C. Kang, Nano Res. 8 (2015) 1584–1594.
[119] G.W. Zhou, L.L. Wang, P.F. Gao, X.W. Yang, Y.S. He, X.Z. Liao, J. Yang, Z.F. Ma, Ind. Eng. Chem. Res. 52 (2013) 1197–1204.
[120] Y. Yoon, K. Lee, C. Baik, H. Yoo, M. Min, Y. Park, S.M. Lee, H. Lee, Adv. Mater. 25 (2013) 4437–4444.
[121] S.L. Jing, H. Jiang, Y.J. Hu, C.Z. Li, J. Mater. Chem. A 2 (2014) 16360–16364.
[122] H.M. Ding, H. Jiang, Z.J. Zhu, Y.J. Hu, F. Gu, C.Z. Li, Electrochim. Acta 157 (2015) 205–210.
[123] L.B. Qu, Y.L. Zhao, A.M. Khan, C.H. Han, K.M. Hercule, M.Y. Yan, X.Y. Liu, W. Chen, D.D. Wang, Z.Y. Cai, W.W. Xu, K.N. Zhao, X.L. Zheng, L.Q. Mai, Nano Lett. 15 (2015) 2037–2044.
[124] M.Q. Sun, G.C. Wang, X.W. Li, C.Z. Li, J. Power Sources 245 (2014) 436–444.
[125] H. Jiang, Y.H. Dai, Y.J. Hu, W.N. Chen, C.Z. Li, ACS Sustain. Chem. Eng. 2 (2014) 70–74.
[126] W. Dai, J.H. Yu, Y. Wang, Y.Z. Song, F.E. Alam, K. Nishimura, C.T. Lin, N. Jiang, J. Mater. Chem. A 3 (2015) 4884–4891.
[127] M.Q. Sun, G.C. Wang, C.Y. Yang, H. Jiang, C.Z. Li, J. Mater. Chem. A 3 (2015) 3880–3890.
[128] M.T. Chen, T. Tao, L. Zhang, W. Gao, C.Z. Li, Chem. Commun. 49 (2013) 1612–1614.
[129] M.T. Chen, L. Zhang, S.S. Duan, S.L. Jing, H. Jiang, C.Z. Li, Adv. Funct. Mater. 24 (2014) 7548–7556.
[130] S.L. Jing, H. Jiang, Y.J. Hu, J.H. Shen, C.Z. Li, Adv. Funct. Mater. 25 (2015) 5395–5401.
[131] Z.P. Chen, W.C. Ren, L.B. Gao, B.L. Liu, S.F. Pei, H.M. Cheng, Nat. Mater. 10 (2011) 424–428.
[132] Y.H. Xue, D.S. Yu, L.M. Dai, R.G. Wang, D.Q. Li, A. Roy, F. Lu, H. Chen, Y. Liu, J. Qu, Phys. Chem. Chem. Phys. 15 (2013) 12220–12226.
[133] M. Zhou, T.Q. Lin, F.Q. Huang, Y.J. Zhong, Z. Wang, Y.F. Tang, H. Bi, D.Y. Wan, J.H. Lin, Adv. Funct. Mater. 23 (2013) 2263–2269.
[134] M. Mecklenburg, A. Schuchardt, Y.K. Mishra, S. Kaps, R. Adelung, A. Lotnyk, L. Kienle, K. Schulte, Adv. Mater. 24 (2012) 3486–3490.
[135] Y. Ito, Y. Tanabe, H.J. Qiu, K. Sugawara, S. Heguri, N.H. Tu, K.K. Huynh, T. Fujita, T. Takahashi, K. Tanigaki, M. Chen, Angew. Chem. Int. Ed. 53 (2014) 4822–4826.
[136] J.S. Lee, H.J. Ahn, J.C. Yoon, J.H. Jang, Phys. Chem. Chem. Phys. 14 (2012) 7938–7943.
[137] J.S. Lee, H.J. Ahn, J.C. Yoon, J.H. Jang, Sci. Rep. 3 (2013) 2125.
[138] M.T. Chen, S.S. Duan, L. Zhang, Z.H. Wang, C.Z. Li, Chem. Commun. 51 (2015) 3169–3172.
[139] W.L. Zhang, H.H. Xie, R.F. Zhang, M.Q. Jian, C.Y. Wang, Q.S. Zheng, F. Wei, Y.Y. Zhang, Carbon 86 (2015) 358–362.
[140] C. Tang, Q. Zhang, M.Q. Zhao, J.Q. Huang, X.B. Cheng, G.L. Tian, H.J. Peng, F. Wei, Adv. Mater. 26 (2014) 6100–6105.

[141] S. Mao, K.H. Yu, J.B. Chang, D.A. Steeber, L.E. Ocola, J.H. Chen, Sci. Rep. 3 (2013) 1696.
[142] Z. Bo, K.H. Yu, G.H. Lu, P.X. Wang, S. Mao, J.H. Chen, Carbon 49 (2011) 1849–1858.
[143] X.B. Wang, Y.J. Zhang, C.Y. Zhi, X. Wang, D.M. Tang, Y.B. Xu, Q.H. Weng, X.F. Jiang, M. Mitome, D. Golberg, Y. Bando, Nat. Commun. 4 (2013) 2905.
[144] W.H. He, C.H. Jiang, J.B. Wang, L.H. Lu, Angew. Chem. Int. Ed. 53 (2014) 9503–9507.
[145] H. Jiang, Y.J. Hu, S.J. Guo, C.Y. Yan, P.S. Lee, C.Z. Li, ACS Nano 8 (2014) 6038–6046.
[146] H. Jiang, T. Sun, C.Z. Li, J. Ma, RSC Adv. 1 (2011) 954–957.
[147] H. Jiang, L.P. Yang, C.Z. Li, C.Y. Yan, P.S. Lee, J. Ma, Energy Environ. Sci. 4 (2011) 1813–1819.
[148] H. Jiang, T. Zhao, C.Z. Li, J. Ma, Chem. Commun. 47 (2011) 8590–8592.
[149] Y.H. Dai, H. Jiang, Y.J. Hu, Y. Fu, C.Z. Li, Ind. Eng. Chem. Res. 53 (2014) 3125–3130.
[150] H. Jiang, C.Z. Li, T. Sun, J. Ma, Nanoscale 4 (2012) 807–812.
[151] H.L. Jiang, Y.H. Zhu, Q. Feng, Y.H. Su, X.L. Yang, C.Z. Li, Chem. Eur. J. 20 (2014) 3106–3112.
[152] H. Jiang, X.L. Yang, C. Chen, Y.H. Zhu, C.Z. Li, New J. Chem. 37 (2013) 1578–1583.
[153] H.L. Jiang, Y.H. Su, Y.H. Zhu, J.H. Shen, X.L. Yang, Q. Feng, C.Z. Li, J. Mater. Chem. A 1 (2013) 12074–12081.
[154] Y.H. Su, H.L. Jiang, Y.H. Zhu, W.J. Zou, X.L. Yang, J.D. Chen, C.Z. Li, J. Power Sources 265 (2014) 246–253.
[155] H.L. Jiang, Y.H. Zhu, Y.H. Su, Y.F. Yao, Y.Y. Liu, X.L. Yang, C.Z. Li, J. Mater. Chem. A 3 (2015) 12642–12645.
[156] H.L. Jin, H.H. Huang, Y.H. He, X. Feng, S. Wang, L.M. Dai, J.C. Wang, J. Am. Chem. Soc. 137 (2015) 7588–7591.
[157] Y.Z. Su, Y.X. Liu, P. Liu, D.Q. Wu, X.D. Zhuang, F. Zhang, X.L. Feng, Angew. Chem. Int. Ed. 54 (2015) 1812–1816.
[158] Z.P. Song, H.S. Zhou, Energy Environ. Sci. 6 (2013) 2280–2301.
[159] S.B. Kulkarni, U.M. Patil, I. Shackery, J.S. Sohn, S. Lee, B. Park, S.C. Jun, J. Mater. Chem. A 2 (2014) 4989–4998.
[160] S.B. Kulkarni, U.M. Patil, I. Shachery, J.S. Sohn, S.C. Lee, B. Park, S.C. Jun, ACS Appl. Mater. Interfaces 6 (2014) 2448–2456.
[161] Y. Liu, Y. Ma, S. Guang, H. Xu, X. Su, J. Mater. Chem. A 2 (2014) 813–823.
[162] M. Yu, Y.X. Ma, J.H. Liu, S.M. Li, Carbon 87 (2015) 98–105.
[163] K.F. Zhou, Y.H. Zhu, X.L. Yang, J.H. Zhou, C.Z. Li, ChemPhysChem 13 (2012) 699–702.
[164] Q.H. Wang, K. Kalantar-Zadeh, A. Kis, J.N. Coleman, M.S. Strano, Nat. Nanotechnol. 7 (2012) 699–702.
[165] C. Tan, X. Qi, X. Huang, J. Yang, B. Zheng, Z. An, R. Chen, J. Wei, B.Z. Tang, W. Huang, H. Zhang, Adv. Mater. 26 (2014) 1735–1739.
[166] O. Lopez-Sanchez, D. Lembke, M. Kayci, A. Radenovic, A. Kis, Nat. Nanotechnol. 8 (2013) 497–501.
[167] G. Sun, J. Liu, X. Zhang, X. Wang, H. Li, Y. Yu, W. Huang, H. Zhang, P. Chen, Angew. Chem. Int. Ed. 53 (2014) 12576–12580.
[168] Z. Yin, X. Zhang, Y. Cai, J. Chen, J.I. Wong, Y.-Y. Tay, J. Chai, J. Wu, Z. Zeng, B. Zheng, H.Y. Yang, H. Zhang, Angew. Chem. Int. Ed. 53 (2014) 12560–12565.
[169] Z. Yin, B. Chen, M. Bosman, X. Cao, J. Chen, B. Zheng, H. Zhang, Small 10 (2014) 3537–3543.
[170] C. Xu, S. Peng, C. Tan, H. Ang, H. Tan, H. Zhang, Q. Yan, J. Mater. Chem. A 2 (2014) 5597–5601.
[171] L.H. Li, Y. Chen, G. Behan, H.Z. Zhang, M. Petravic, A.M. Glushenkov, J. Mater. Chem. 21 (2011) 11862–11866.
[172] H. Li, G. Lu, Y.L. Wang, Z.Y. Yin, C.X. Cong, Q.Y. He, L. Wang, F. Ding, T. Yu, H. Zhang, Small 9 (2013) 1974–1981.
[173] R.J. Smith, P.J. King, M. Lotya, C. Wirtz, U. Khan, S. De, A. O'Neill, G.S. Duesberg, J.C. Grunlan, G. Moriarty, J. Chen, J. Wang, A.I. Minett, V. Nicolosi, J.N. Coleman, Adv. Mater. 23 (2011) 3944–3948.
[174] K.K. Kim, A. Hsu, X. Jia, S.M. Kim, Y. Shi, M. Hofmann, D. Nezich, J.F. Rodriguez-Nieva, M. Dresselhaus, T. Palacios, J. Kong, Nano Lett. 12 (2012) 161–166.
[175] S. Chatterjee, Z. Luo, M. Acerce, D.M. Yates, A.T.C. Johnson, L.G. Sneddon, Chem. Mater. 23 (2011) 4414–4416.
[176] X.S. Wang, H.B. Feng, Y.M. Wu, L.Y. Jiao, J. Am. Chem. Soc. 135 (2013) 5304–5307.
[177] K.K. Liu, W.J. Zhang, Y.H. Lee, Y.C. Lin, M.T. Chang, C. Su, C.S. Chang, H. Li, Y.M. Shi, H. Zhang, C.S. Lai, L.J. Li, Nano Lett. 12 (2012) 1538–1544.
[178] Y.H. Lee, X.Q. Zhang, W.J. Zhang, M.T. Chang, C.T. Lin, K.D. Chang, Y.C. Yu, J.T.W. Wang, C.S. Chang, L.J. Li, T.W. Lin, Adv. Mater. 24 (2012) 2320–2325.
[179] D. Yoo, M. Kim, S. Jeong, J. Han, J. Cheon, J. Am. Chem. Soc. 136 (2014) 14670–14673.
[180] X. Zhang, Z.C. Lai, Z.D. Liu, C.L. Tan, Y. Huang, B. Li, M.T. Zhao, L.H. Xie, W. Huang, H. Zhang, Angew. Chem. 127 (2015) 5515–5518.
[181] I.-Y. Jeon, Y.-R. Shin, G.-J. Sohn, H.-J. Choi, S.-Y. Bae, J. Mahmood, S.-M. Jung, J.-M. Seo, M.-J. Kim, D. Wook Chang, L. Dai, J.-B. Baek, Proc. Natl. Acad. Sci. U. S. A. 109 (2012) 5588–5593.
[182] V. Nicolosi, M. Chhowalla, M.G. Kanatzidis, M.S. Strano, J.N. Coleman, Science 340 (2013) 1226419.
[183] Y.G. Yao, L. Tolentino, Z.Z. Yang, X.J. Song, W. Zhang, Y.S. Chen, C.P. Wong, Adv. Funct. Mater. 23 (2013) 3577–3583.
[184] X. Zhang, H. Xie, Z. Liu, C. Tan, Z. Luo, H. Li, J. Lin, L. Sun, Z. Xu, W. Chen, L. Xie, W. Huang, H. Zhang, Angew. Chem. Int. Ed. 54 (2015) 3653–3657.
[185] Y.J. Zhan, Z. Liu, S. Najmaei, P.M. Ajayan, J. Lou, Small 8 (2012) 966–971.
[186] K. Keyshar, Y. Gong, G. Ye, G. Brunetto, W. Zhou, D.P. Cole, K. Hackenberg, Y. He, L. Machado, M. Kabbani, A.H.C. Hart, B. Li, D.S. Galvao, A. George, R. Vajtai, C.S. Tiwary, P.M. Ajayan, Adv. Mater. 27 (2015) 4640–4648.
[187] M. Zhang, Y. Zhu, X. Wang, Q. Feng, S. Qiao, W. Wen, Y. Chen, M. Cui, J. Zhang, C. Cai, L. Xie, J. Am. Chem. Soc. 137 (2015) 7051–7054.
[188] Q. Feng, Y. Zhu, J. Hong, M. Zhang, W. Duan, N. Mao, J. Wu, H. Xu, F. Dong, F. Lin, C. Jin, C. Wang, J. Zhang, L. Xie, Adv. Mater. 26 (2014) 2648–2653.
[189] C. Huang, S. Wu, A.M. Sanchez, J.J.P. Peters, R. Beanland, J.S. Ross, P. Rivera, W. Yao, D.H. Cobden, X. Xu, Nat. Mater. 13 (2014) 1096–1101.
[190] H. Heo, J.H. Sung, G. Jin, J.H. Ahn, K. Kim, M.J. Lee, S. Cha, H. Choi, M.H. Jo, Adv. Mater. 27 (2015) 3803–3810.
[191] Q. Liu, X. Li, Z. Xiao, Y. Zhou, H. Chen, A. Khalil, T. Xiang, J. Xu, W. Chu, X. Wu, J. Yang, C. Wang, Y. Xiong, C. Jin, P.M. Ajayan, L. Song, Adv. Mater. 27 (2015) 4837–4844.
[192] L. Cheng, W. Huang, Q. Gong, C. Liu, Z. Liu, Y. Li, H. Dai, Angew. Chem. Int. Ed. 53 (2014)
7860–7863.
[193] B. Mahler, V. Hoepfner, K. Liao, G.A. Ozin, J. Am. Chem. Soc. 136 (2014) 14121–14127.
[194] V.V. Plashnitsa, F. Vietmeyer, N. Petchsang, P. Tongying, T.H. Kosel, M. Kuno, J. Phys. Chem. Lett. 3 (2012) 1554–1558.
[195] S. Jeong, D. Yoo, J. Jang, M. Kim, J. Cheon, J. Am. Chem. Soc. 134 (2012) 18233–18236.
[196] J.W. Thomson, K. Nagashima, P.M. Macdonald, G.A. Ozin, J. Am. Chem. Soc. 133 (2011) 5036–5041.
[197] J. Joo, H.B. Na, T. Yu, J.H. Yu, Y.W. Kim, F. Wu, J.Z. Zhang, T. Hyeon, J. Am. Chem. Soc. 125 (2003) 11100–11105.
[198] Y.P. Du, Z.Y. Yin, J.X. Zhu, X. Huang, X.J. Wu, Z.Y. Zeng, Q.Y. Yan, H. Zhang, Nat. Commun. 3 (2012) 1177.
[199] J. Seo, Y. Jun, S. Park, H. Nah, T. Moon, B. Park, J. Kim, Y.J. Kim, J. Cheon, Angew. Chem. Int. Ed. 46 (2007) 8828–8831.
[200] Y.K. Jung, J.I. Kim, J. Lee, J. Am. Chem. Soc. 132 (2010) 178–184.
[201] W. Jung, S. Lee, D. Yoo, S. Jeong, P. Miró, A. Kuc, T. Heine, J. Cheon, J. Am. Chem. Soc. 137 (2015) 7266–7269.
[202] Y. Gong, S. Yang, L. Zhan, L. Ma, R. Vajtai, P.M. Ajayan, Adv. Funct. Mater. 24 (2014) 125–130.
[203] L. Zhang, W. Fan, W.W. Tjiu, T. Liu, RSC Adv. 5 (2015) 34777–34787.
[204] J. Duan, S. Chen, B.A. Chambers, G.G. Andersson, S.Z. Qiao, Adv. Mater. 27 (2015) 4234–4241.
[205] C. Du, H. Huang, X. Feng, S. Wu, W. Song, J. Mater. Chem. A 3 (2015) 7616–7622.
[206] H. Jiang, D. Ren, H. Wang, Y. Hu, S. Guo, H. Yuan, P. Hu, L. Zhang, C. Li, Adv. Mater. 27 (2015) 3687–3695.
[207] D. Chakravarty, C.S. Tiwary, L.D. Machado, G. Brunetto, S. Vinod, R.M. Yadav, D.S. Galvao, S.V. Joshi, G. Sundararajan, P.M. Ajayan, Adv. Mater. 27 (2015) 4534–4543.
[208] C. Tan, X. Qi, Z. Liu, F. Zhao, H. Li, X. Huang, L. Shi, B. Zheng, X. Zhang, L. Xie, Z. Tang, W. Huang, H. Zhang, J. Am. Chem. Soc. 137 (2015) 1565–1571.
[209] X. Hong, J. Liu, B. Zheng, X. Huang, X. Zhang, C. Tan, J. Chen, Z. Fan, H. Zhang, Adv. Mater. 26 (2014) 6250–6254.
[210] P.H. Qiu, C.B. Mao, ACS Nano 4 (2010) 1573–1579.
[211] G. Sun, X. Zhang, R. Lin, J. Yang, H. Zhang, P. Chen, Angew. Chem. Int. Ed. 54 (2015) 4651–4656.
[212] C. Hao, F. Wen, J. Xiang, L. Wang, H. Hou, Z. Su, W. Hu, Z. Liu, Adv. Funct. Mater. 24 (2014) 6700–6707.
[213] H. Tang, J. Wang, H. Yin, H. Zhao, D. Wang, Z. Tang, Adv. Mater. 27 (2015) 1117–1123.
[214] Y. Shi, J. Wang, C. Wang, T.T. Zhai, W.J. Bao, J.J. Xu, X.H. Xia, H.Y. Chen, J. Am. Chem. Soc. 137 (2015) 7365–7370.
[215] X.L. Li, J.P. Ge, Y.D. Li, Chem. Eur. J. 10 (2004) 6163–6171.
[216] S. Prabakar, C.W. Bumby, R.D. Tilley, Chem. Mater. 21 (2009) 1725–1730.
[217] Y.J. Zhang, Q.F. Gong, L. Li, H.C. Yang, Y.G. Li, Q.B. Wang, Nano Res. 8 (2015) 1108–1115.
[218] G. Zhou, X.Y. Xu, J.Y. Yu, B. Feng, Y. Zhang, J.G. Hu, Y.X. Zhou, CrystEngComm 16 (2014) 9025–9032.
[219] P.P. Wang, H.Y. Sun, Y.J. Ji, W.H. Li, X. Wang, Adv. Mater. 26 (2014) 964–969.
[220] Z.N. Deng, Y.J. Hu, D.Y. Ren, S.L. Lin, H. Jiang, C.Z. Li, Chem. Commun. 51 (2015) 13838–13841.
[221] X.B. Ge, L.Y. Chen, L. Zhang, Y.R. Wen, A. Hirata, M. Chen, Adv. Mater. 26 (2014) 3100–3104.
[222] Y.H. Chang, F.Y. Wu, T.Y. Chen, C.L. Hsu, C.H. Chen, F. Wiryo, K.H. Wei, C.Y. Chiang, L.J. Li, Small 10 (2014) 895–900.
[223] X.M. Geng, W. Wu, N. Li, W.W. Sun, J. Armstrong, A. Al-hilo, M. Brozak, J.B. Cui, T.P. Chen, Adv. Funct. Mater. 24 (2014) 6123–6129.
[224] L. Fei, Y. Xu, X.F. Wu, G. Chen, Y.L. Li, B.S. Li, S.G. Deng, S. Smirnov, H.Y. Fan, H.M. Luo, Nanoscale 6 (2014) 3664–3669.
[225] H.L. Yu, C. Ma, B.H. Ge, Y.J. Chen, Z. Xu, C.L. Zhu, C.Y. Li, Q.Y. Ouyang, P. Gao, J.Q. Li, C.W. Sun, L.H. Qi, Y.M. Wang, F.H. Li, Chem. Eur. J. 19 (2013) 5818–5823.
[226] Q.J. Xiang, J.G. Yu, M. Jaroniec, J. Am. Chem. Soc. 134 (2012) 6575–6578.
[227] W.J. Zhou, K. Zhou, D.M. Hou, X.J. Liu, G.Q. Li, Y.H. Sang, H. Liu, L.G. Li, S.W. Chen, ACS Appl. Mater. Interfaces 6 (2014) 21534–21540.
[228] Z.K. Tang, Y.N. Zhang, D.Y. Zhang, W.M. Lau, L.M. Liu, Sci. Rep. 4 (2014) 7007.
[229] X. Jiang, X.L. Yang, Y.H. Zhu, J.H. Shen, K.C. Fan, C.Z. Li, J. Power Sources 237 (2013) 178–186.

[230] Y. Hou, Z.H. Wen, S.M. Cui, X.R. Guo, J.H. Chen, Adv. Mater. 25 (2013) 6291–6297.
[231] S.J. Peng, L.L. Li, X.P. Han, W.P. Sun, M. Srinivasan, S.G. Mhaisalkar, F. Cheng, Q.Y. Yan, J. Chen, S. Ramakrishna, Angew. Chem. Int. Ed. 53 (2014) 12594–12599.
[232] N. Lingappan, N.H. Van, S. Lee, D.J. Kang, J. Power Sources 280 (2015) 39–46.
[233] S. Wang, K. Li, Y. Chen, H. Chen, M. Ma, J. Feng, Q. Zhao, J. Shi, Biomaterials 39 (2015) 206–217.
[234] S. Wang, X. Li, Y. Chen, X.J. Cai, H.L. Yao, W. Gao, Y.Y. Zheng, X. An, J.L. Shi, H.R. Chen, Adv. Mater. 27 (2015) 2775–2782.
[235] T. Liu, C. Wang, W. Cui, H. Gong, C. Liang, X. Shi, Z. Li, B. Sun, Z. Liu, Nanoscale 6 (2014) 11219–11225.
[236] L.R. Hu, Y.M. Ren, H.X. Yang, Q. Xu, ACS Appl. Mater. Interfaces 6 (2014) 14644–14652.
[237] D.Y. Ren, H. Jiang, Y.J. Hu, L. Zhang, C.Z. Li, RSC Adv. 4 (2014) 40368–40372.
[238] H.S. Li, X.Y. Wang, B. Ding, G. Pang, P. Nie, L.F. Shen, X.G. Zhang, ChemElectroChem 1 (2014) 1118–1125.
[239] F. Zhou, S. Xin, H.W. Liang, L.T. Song, S.H. Yu, Angew. Chem. Int. Ed. 53 (2014) 11552–11556.
[240] H.W. Liang, Q.F. Guan, L.F. Chen, Z. Zhu, W.J. Zhang, S.H. Yu, Angew. Chem. Int. Ed. 51 (2012) 5101–5105.
[241] H. Zhu, J.F. Zhang, R.P. Yanzhang, M.L. Du, Q.F. Wan, G.H. Gao, J.D. Wu, G.M. Wu, M. Zhang, B. Liu, J.M. Yao, X.W. Zhang, Adv. Mater. 27 (2015) 4752–4759.
[242] X. Guo, G.L. Cao, F. Ding, X.Y. Li, S.Y. Zhen, Y.F. Xue, Y.M. Yan, T. Liu, K.N. Sun, J. Mater. Chem. A 3 (2015) 5041–5046.
[243] H.L. Yu, C.L. Zhu, K. Zhang, Y.J. Chen, C.Y. Li, P. Gao, P.P. Yang, Q.Y. Ouyang, J. Mater. Chem. A 2 (2014) 4551–4557.
[244] H.T. Wang, Z.Y. Lu, D.S. Kong, J. Sun, T.M. Hymel, Y. Cui, ACS Nano 8 (2014) 4940–4947.
[245] X.Y. Yu, H. Hu, Y.W. Wang, H.Y. Chen, X.W. Lou, Angew. Chem. Int. Ed. 54 (2015) 7395–7398.
[246] X.Y. Yu, L. Yu, L.F. Shen, X.H. Song, H.Y. Chen, X.W. Lou, Adv. Funct. Mater. 24 (2014) 7440–7446.
[247] C. Lei, F. Han, D. Li, W.C. Li, Q. Sun, X.Q. Zhang, A.H. Lu, Nanoscale 5 (2013) 1168–1175.
[248] X.Y. Zhao, C.W. Hu, M.H. Cao, Chem. Asian J. 8 (2013) 2701–2707.
[249] Z. Wang, J.G. Hou, C. Yang, S.Q. Jiao, H.M. Zhu, Chem. Commun. 50 (2014) 1731–1734.
[250] X.D. Zhang, Y. Xie, Chem. Soc. Rev. 42 (2013) 8187–8199.
[251] X.F. Song, J.L. Hu, H.B. Zeng, J. Mater. Chem. C 1 (2013) 2952–2969.
[252] J.Y. Wang, S.B. Deng, Z.F. Liu, Z.R. Liu, Natl. Sci. Rev. 2 (2015) 22–39.
[253] L.K. Li, Y.J. Yu, G.J. Ye, Q.Q. Ge, X.D. Ou, H. Wu, D.L. Feng, X.H. Chen, Y.B. Zhang, Nat. Nanotechnol. 9 (2014) 372–377.
[254] S.L. Zhang, Z. Yan, Y.F. Li, Z.F. Chen, H.B. Zeng, Angew. Chem. Int. Ed. 54 (2015) 3112–3115.
[255] X.D. Zhuang, Y.Y. Mai, D.Q. Wu, F. Zhang, X.L. Feng, Adv. Mater. 27 (2015) 403–427.
[256] X. Wang, X. Li, L. Zhang, Y. Yoon, P.K. Weber, H. Wang, J. Guo, H. Dai, Science 324 (2009) 768–771.
[257] T.B. Martins, R.H. Miwa, A.J.R. da Silva, A. Fazzio, Phys. Rev. Lett. 98 (2007) 196803.
[258] S.W. Cao, J.X. Low, J.G. Yu, M. Jaroniec, Adv. Mater. 27 (2015) 2150–2176.
[259] K. Maeda, X. Wang, Y. Nishihara, D. Lu, M. Antonietti, K. Domen, J. Phys. Chem. C 113 (2009) 4940–4947.
[260] H. Ji, F. Chang, X. Hu, W. Qin, J. Shen, Chem. Eng. J. 218 (2013) 183–190.
[261] S.C. Yan, Z.S. Li, Z.G. Zou, Langmuir 25 (2009) 10397–10401.
[262] G. Zhang, J. Zhang, M. Zhang, X. Wang, J. Mater. Chem. 22 (2012) 8083–8091.
[263] F. Dong, Z. Wang, Y. Sun, W.K. Ho, H. Zhang, J. Colloid Interface Sci. 401 (2013) 70–79.
[264] A.B. Jorge, D.J. Martin, M.T.S. Dhanoa, A.S. Rahman, N. Makwana, J. Tang, A. Sella, F. Corà, S. Firth, J.A. Darr, P.F. McMillan, J. Phys. Chem. C 117 (2013) 7178–7185.
[265] X. Wang, K. Maeda, X. Chen, K. Takanabe, K. Domen, Y. Hou, X. Fu, M. Antonietti, J. Am. Chem. Soc. 131 (2009) 1680–1681.
[266] J. Zhang, F. Guo, X. Wang, Adv. Funct. Mater. 23 (2013) 3008–3014.
[267] Q. Han, B. Wang, Y. Zhao, C.G. Hu, L.T. Qu, Angew. Chem. Int. Ed. 54 (2015) 11433–11437.
[268] Q.H. Liang, Z. Li, X.L. Yu, Z.H. Huang, F.Y. Kang, Q.H. Yang, Adv. Mater. 27 (2015) 4634–4639.
[269] J. Xu, F. Wu, H.T. Wu, B. Xue, Y.X. Li, Y. Cao, Microporous Mesoporous Mater. 198 (2014) 223–229.
[270] Y.S. Jun, J. Park, S.U. Lee, A. Thomas, W.H. Hong, G.D. Stucky, Angew. Chem. Int. Ed. 52 (2013) 11083–11087.
[271] Y. Zhao, C.G. Hu, L. Song, L.X. Wang, G.Q. Shi, L.M. Dai, L.T. Qu, Energy Environ. Sci. 7 (2014) 1913–1918.
[272] Y. Zhao, C.G. Hu, Y. Hu, H.H. Cheng, G.Q. Shi, L.T. Qu, Angew. Chem. Int. Ed. 124 (2012) 11533–11537.
[273] J. Liang, Y. Zheng, J. Chen, J. Liu, H.J. Denisa, M. Jaroniec, S.Z. Qiao, Angew. Chem. Int. Ed. 124 (2012) 3958–3962.
[274] J.J. Duan, S. Chen, M. Jaroniec, S.Z. Qiao, ACS Nano 9 (2015) 931–940.
[275] Q. Chen, Y. Zhao, X.K. Huang, N. Chen, L.T. Qu, J. Mater. Chem. A 3 (2015) 6761–6766.
[276] H.J. Huang, S.B. Yang, R. Vajtai, X. Wang, P.M. Ajayan, Adv. Mater. 26 (2014) 5160–5165.
[277] Y. Zhao, F. Zhao, X.P. Wang, C.Y. Xu, Z.P. Zhang, G.Q. Shi, L.T. Qu, Angew. Chem. Int. Ed. 53 (2014) 13934–13939.
[278] J.Q. Tian, R. Ning, Q. Liu, A.M. Asiri, A.O. Al-Youbi, X.P. Sun, ACS Appl. Mater. Interfaces 6 (2014) 1011–1017.
[279] T.Y. Ma, S. Dai, M. Jaroniec, S.Z. Qiao, Angew. Chem. Int. Ed. 53 (2014) 7281–7285.
[280] J. Liu, Y. Liu, N.Y. Liu, Y.Z. Han, X. Zhang, H. Huang, Y. Lifshitz, S.T. Lee, J. Zhong, Z.H. Kang, Science 347 (2015) 970–974.
[281] J.H. Shen, Y.F. Li, Y.H. Su, Y.H. Zhu, H.L. Jiang, X.L. Yang, C.Z. Li, Nanoscale 7 (2015) 2003–2008.
[282] H.J. Zhao, X.F. Song, H.B. Zeng, NPG Asia Mater. 7 (2015) 168.
[283] S. Frueh, R. Kellett, C. Mallery, T. Molter, W.S. Willis, C. King'ondu, S.L. Suib, Inorg. Chem. 50 (2010) 783–792.
[284] S. Vinod, C.S. Tiwary, P.A. Autreto, J. Taha-Tijerina, S. Ozden, A.C. Chipara, R. Vajtai, D.S. Galvao, T.N. Narayanan, P.M. Ajayan, Nat. Commun. 5 (2014) 4541.
[285] M. Loeblein, R.Y. Tay, S.H. Tsang, W.B. Ng, E.H.T. Teo, Small 10 (2014) 2992–2999.
[286] R.Y. Tay, X. Wang, S.H. Tsang, G.C. Loh, R.S. Sing, H. Li, G. Mallick, E. Teo, J. Mater. Chem. C 2 (2014) 1650–1657.
[287] S.M. Kim, A. Hsu, P.T. Araujo, Y.-H. Lee, T. Palacios, M. Dresselhaus, J.-C. Idrobo, K.K. Kim, J. Kong, Nano Lett. 13 (2013) 933–941.
[288] K. Uosaki, G. Elumalai, H. Noguchi, T. Masuda, A. Lyalin, A. Nakayama, T. Taketsugu, J. Am. Chem. Soc. 136 (2014) 6542–6545.
[289] M. Busch, E. Ahlberg, I. Panas, Catal. Today 202 (2013) 114–119.
[290] S. Chakrabarty, K. De, S. Das, V.S. Amaral, K. Chatterjee, J. Nanosci. Nanotechnol. 14 (2014) 4236–4244.
[291] J.B. Zhu, L.F. Bai, Y.F. Sun, X.D. Zhang, Q.Y. Li, B.X. Cao, W.S. Yan, Y. Xie, Nanoscale 5 (2013) 5241–5246.
[292] T. Yao, L. Liu, C. Xiao, X.D. Zhang, Q.H. Liu, S.Q. Wei, Y. Xie, Angew. Chem. Int. Ed. 52 (2013) 7554–7558.
[293] C. Schliehe, B.H. Juarez, M. Pelletier, S. Jander, D. Greshnykh, M. Nagel, A. Meyer, S. Foerster, A. Kornowski, C. Klinke, H. Weller, Science 329 (2010) 550–553.
[294] X.D. Zhang, J.J. Zhang, J.Y. Zhao, B.C. Pan, M.G. Kong, J. Chen, Y. Xie, J. Am. Chem. Soc. 134 (2012) 11908–11911.
[295] X.H. Liu, R.Z. Ma, Y. Bando, T. Sasaki, Adv. Mater. 24 (2012) 2148–2153.
[296] O.C. Compton, A. Abouimrane, Z. An, M.J. Palmeri, L.C. Brinson, K. Amine, S.T. Nguyen, Small 8 (2012) 1110–1116.
[297] W.R. Cheng, J.F. He, T. Yao, Z.H. Sun, Y. Jiang, Q.H. Liu, S. Jiang, F.C. Hu, Z. Xie, B. He, W.S. Yan, S.Q. Wei, J. Am. Chem. Soc. 136 (2014) 10393–10398.
[298] S. Ida, N. Kim, E. Ertekin, S. Takenaka, T. Ishihara, J. Am. Chem. Soc. 137 (2015) 239–244.
[299] Y.F. Sun, F.C. Lei, S. Gao, B.C. Pan, J.F. Zhou, Y. Xie, Angew. Chem. Int. Ed. 52 (2013) 10569–10572.
[300] P. Zhao, Y.H. Zhu, X.L. Yang, J.H. Shen, X. Jiang, J. Zong, C.Z. Li, Dalton Trans. 43 (2014) 451–457.
[301] H. Jiang, C.Z. Li, T. Sun, J. Ma, Chem. Commun. 48 (2012) 2606–2608.
[302] L.L. Peng, X. Peng, B.R. Liu, C.Z. Wu, Y. Xie, G.H. Yu, Nano Lett. 13 (2013) 2151–2157.
[303] H. Jiang, T. Sun, C.Z. Li, J. Ma, J. Mater. Chem. 22 (2012) 2751–2756.
[304] C.Y. Yan, H. Jiang, T. Zhao, C.Z. Li, J. Ma, P.S. Lee, J. Mater. Chem. 21 (2011) 10482–10488.
[305] H. Jiang, T. Zhao, C.Z. Li, J. Ma, J. Mater. Chem. 21 (2011) 3818–3823.
[306] H. Jiang, J.Q. Hu, C.Z. Li, F. Gu, J. Ma, CrystEngComm 12 (2010) 1726–1729.
[307] Q. Xiao, Z. Liu, A. Bo, S. Zavahir, S. Sarina, S. Bottle, J.D. Riches, H.Y. Zhu, J. Am. Chem. Soc. 137 (2015) 1956–1966.
[308] R.Z. Ma, X.H. Liu, J.B. Liang, Y. Bando, T. Sasaki, Adv. Mater. 26 (2014) 4173–4178.
[309] F. Song, X.L. Hu, J. Am. Chem. Soc. 136 (2014) 16481–16484.
[310] F.X. Geng, R.Z. Ma, Y. Ebina, Y. Yamauchi, N. Miyamoto, T. Sasaki, J. Am. Chem. Soc. 136 (2014) 5491–5500.
[311] D. Yang, Z.Y. Lu, X.H. Rui, X. Huang, H. Li, J.X. Zhu, W.Y. Zhang, Y.M. Lam, H.H. Hng, H. Zhang, Q.Y. Yan, Angew. Chem. Int. Ed. 53 (2014) 9352–9355.
[312] J. Bao, X. Zhang, B. Fan, J. Zhang, M. Zhou, W.L. Yang, X. Hu, H. Wang, B.C. Pan, Y. Xie, Angew. Chem. 127 (2015) 7507–7512.
[313] L.Y. Dang, C.Z. Wei, H.F. Ma, Q.Y. Lu, F. Gao, Nanoscale 7 (2015) 8101–8109.
[314] M. Naguib, J. Halim, J. Lu, K.M. Cook, L. Hultman, Y. Gogotsi, M.W. Barsoum, J. Am. Chem. Soc. 135 (2013) 15966–15969.
[315] M. Naguib, V.N. Mochalin, M.W. Barsoum, Y. Gogotsi, Adv. Mater. 26 (2014) 992–1005.
[316] O. Mashtalir, M. Naguib, V.N. Mochalin, Y. Dall'Agnese, M. Heon, M.W. Barsoum, Y. Gogotsi, Nat. Commun. 4 (2013) 1716.
[317] M.R. Lukatskaya, O. Mashtalir, C.E. Ren, Y. Dall'Agnese, P. Rozier, P.L. Taberna, M. Naguib, P. Simon, M.W. Barsoum, Y. Gogotsi, Science 341 (2013) 1502–1505.
[318] M.Q. Zhao, C.E. Ren, Z. Ling, M.R. Lukatskaya, C.F. Zhang, K.L.V. Aken, M.W. Barsoum, Y. Gogotsi, Adv. Mater. 27 (2015) 339–345.
[319] C.X. Peng, B.D. Chen, Y. Qin, S.H. Yang, C.Z. Li, Y.H. Zuo, S.Y. Liu, J.H. Yang, ACS Nano. 6 (2015) 1074–1081.
[320] M. Zhou, X.L. Li, B. Wang, Y.B. Zhang, J. Ning, Z.C. Xiao, X.H. Zhang, Y.H. Chang, L.J. Zhi, Nano. Lett. 15 (2015) 6222–6228.
[321] C. Zhang, W. Lv, Y. Tao, Q.H. Yang, Energy Environ. Sci. 8 (2015) 1390–1403.
[322] B. Wang, X.L. Li, B. Luo, L. Hao, M. Zhou, X.H. Zhang, Z.J. Fan, L.J. Zhi, Adv. Mater. 27 (2015) 1526–1532.
[323] Y. Xu, Y. Tao, X.Y. Zheng, H.Y. Ma, J.Y. Luo, F.Y. Kang, Q.-H. Yang, Adv. Mater. 27 (2015) 8082–8087.

[324] X.Y. Zheng, J.Y. Luo, W. Lv, D.W. Wang, Q.H. Yang, Adv. Mater. 27 (2015) 5388–5395.
[325] L. Hao, J. Ning, B. Luo, B. Wang, Y.B. Zhang, Z.H. Tang, J.H. Yang, A. Thomas, L.J. Zhi, J. Am. Chem. Soc. 137 (2015) 219–225.
[326] B. Luo, B. Wang, M. Liang, J. Ning, X. Li, L.J. Zhi, Adv. Mater. 24 (2012) 1405–1409.
[327] B. Wang, B. Luo, X. Li, L.J. Zhi, Mater. Today 15 (2012) 544–552.
[328] B. Wang, X. Li, T. Qiu, B. Luo, J. Ning, J. Li, X. Zhang, M. Liang, L.J. Zhi, Nano Lett. 13 (2013) 5578–5584.
[329] D. Kong, H. He, Q. Song, B. Wang, W. Lv, Q.-H. Yang, L.J. Zhi, Energy Environ. Sci. 7 (2014) 3320–3325.
[330] A.V. Murugan, M. Quintin, M. Delville, G. Campet, C.S. Gopinath, K. Vijayamohanan, J. Power Sources 156 (2006) 615–619.
[331] Y.X. Xu, G.Q. Shi, X.F. Duan, Acc. Chem. Res. 48 (2015) 1666–1675.
[332] X.H. Xia, D.L. Chao, Y.Q. Zhang, Z.X. Shen, H.J. Fan, Nano Today 9 (2014) 785–807.
[333] J. Yan, Q. Wang, T. Wei, Z. Fan, Adv. Energy Mater. 4 (2014) 1300816.
[334] C. Hu, H. Cheng, Y. Zhao, Y. Hu, Y. Liu, L. Dai, L. Qu, Adv. Mater. 24 (2012) 5493–5498.
[335] Y.H. Su, Y.H. Zhu, X.L. Yang, J.H. Shen, J.D. Lu, X.Y. Zhang, J.D. Chen, C.Z. Li, Ind. Eng. Chem. Res. 52 (2013) 6076–6082.
[336] X.L. Yang, W.J. Zou, Y.H. Su, Y.H. Zhu, H.L. Jiang, J.H. Shen, C.Z. Li, J. Power Sources 266 (2014) 36–42.
[337] Y. Su, Y. Zhang, X. Zhuang, S. Li, D. Wu, F. Zhang, X. Feng, Carbon 62 (2013) 296–301.
[338] M.R. Gao, Q. Gao, J. Jiang, C.H. Cui, W.T. Yao, S.H. Yu, Angew. Chem. Int. Ed. 50 (2011) 4905–4908.
[339] X. Zhao, H. Zhu, X.R. Yang, Nanoscale 6 (2014) 10680–10685.
[340] Y. Zheng, Y. Jiao, Y. Zhu, L.H. Li, Y. Han, Y. Chen, A. Du, M. Jaroniec, S.Z. Qiao, Nat. Commun. 5 (2014) 3783.
[341] V. Artero, M. Chavarot-Kerlidou, M. Fontecave, Angew. Chem. Int. Ed. 50 (2011) 7238–7266.
[342] L. Liang, H. Cheng, F.C. Lei, J. Han, S. Gao, C.M. Wang, Y.F. Sun, S. Qamar, S.Q. Wei, Y. Xie, Angew. Chem. Int. Ed. 54 (2015) 12004–12008.
[343] C.H. Cui, S.H. Yu, Acc. Chem. Res. 46 (2013) 1427–1437.
[344] E. Antolini, ACS Catal. 4 (2014) 1426–1440.
[345] Y.H. Su, Y.H. Zhu, H.L. Jiang, J.H. Shen, X.L. Yang, W.J. Zou, J.D. Chen, C.Z. Li, Nanoscale 6 (2014) 15080–15089.
[346] J.T. Zhang, Z.H. Zhao, Z.H. Xia, L.M. Dai, Nat. Nanotech. 10 (2015) 444–452.
[347] G.L. Tian, M.Q. Zhao, D.S. Yu, X.Y. Kong, J.Q. Huang, Q. Zhang, F. Wei, Small 10 (2014) 2251–2259.
[348] A. Yamaguchi, R. Inuzuka, T. Takashima, T. Hayashi, K. Hashimoto, R. Nakamura, Nat. Commun. 5 (2014) 4256.
[349] S. Zhang, Y.Z. Hao, D. Su, V.V.T. Doan-Nguyen, Y.T. Wu, J. Li, S. Sun, C.B. Murray, J. Am. Chem. Soc. 136 (2014) 15921–15924.
[350] X.L. Wang, G.Q. Shi, Energy Environ. Sci. 8 (2015) 790–823.
[351] F. Yavari, Z. Chen, A.V. Thomas, W.C. Ren, H.M. Cheng, N. Koeatkar, Sci. Rep. 1 (2011) 166.
[352] Y. Ma, M.G. Zhao, B. Cai, W. Wang, Z.Z. Ye, J.Y. Huang, Biosens. Bioelectron. 59 (2014) 384–388.
[353] Y.L. Lei, F. Chen, Y.J. Luo, L. Zhang, Chem. Phys. Lett. 593 (2014) 122–127.
[354] S.W. Crowder, D. Prasai, R. Rath, D.A. Balikov, H. Bae, K.I. Bolotin, H.J. Sung, Nanoscale 5 (2013) 4171–4176.
[355] Q. Song, Z.Y. Jiang, N. Li, P. Liu, L.W. Liu, M.L. Tang, G.S. Cheng, Biomaterials 35 (2014) 6930–6940.

Jianhua Shen received his BS degrees (2009) from East China University of Science and Technology. He then obtained his PhD degree under Prof. Yihua Zhu in 2014. He is currently working as a postdoctoral researcher at Key Laboratory for Ultrafine Materials of Ministry of Education with Prof. Chunzhong Li. His research is focused on the preparations and applications on two-dimensional nanosheets and their nanocomposites.

Yihua Zhu received his BS degree from Nanjing University and MS and PhD degrees from East China University of Science and Technology (ECUST). Currently he is a full professor in Key Laboratory for Ultrafine Materials of Ministry of Education at ECUST, and elected as a Fellow of the Royal Society of Chemistry in 2015. His research interests include porous materials and nanostructured materials and related functional applications, especially for biosensors, drug delivery, catalysis and clean energy.

Hao Jiang received his PhD degree in Materials Science and Engineering under Prof. Chunzhong Li from East China University of Science & Technology (ECUST), China, in 2009. He joined Temasek Laboratories, Nanyang Technological University (NTU) in Singapore, as a research scientist in 2009–2011. Currently he is a full professor in Key Laboratory for Ultrafine Materials of Ministry of Education at ECUST, and become the winner of the National Science Fund for Excellent Young Scholars in 2015. His current research interests focus on the design and preparation of novel hierarchical nanomaterials and their applications in energy storage devices.

Chunzhong Li received BS (1989), MS (1992) and PhD (1997) from East China University of Science and Technology (ECUST). He became a full professor of school of materials science and engineering in 1998, and now he is the dean of School of Materials Science and Engineering at ECUST. He was elected as a Fellow of the Royal Society of Chemistry in 2015, became the Cheung Kong Distinguished Professor in 2014, the winner of the National Science Fund for Distinguished Young Scholars in 2009. His research interests include functionalization and fabrication of nanomaterials for new energy, environment and relevant applications.